Stream Carbon Flux in the Northern Pacific Coastal Temperate Rainforest: Seasonal DOC Transport and CO_2 and CH_4 Emissions

by

Anna Bishop

A thesis submitted in partial fulfillment of the requirements for the degree of

Master of Science

IN ECOLOGY

Department of BIOLOGICAL SCIENCES

University of Alberta

© Anna Bishop, 2020

Abstract

Streams in British Columbia's humid, organic-rich Pacific Coastal Temperate Rainforest (PCTR) deliver globally significant yields of soil-derived dissolved organic carbon (DOC) to the ocean, which can affect ocean acidification, provide energy to coastal food webs, and off-gas to the atmosphere as CO_2. Although there is an established relationship between discharge and DOC, the key subsurface processes controlling stream DOC in this region have not been determined, and the balance between organic carbon export and stream CO_2 and CH_4 efflux in this region is currently unknown. To determine seasonal and landscape controls on stream DOC, CO_2, and CH_4 in the PCTR, we used automated, *in situ* fDOM sensors in combination with field-based sampling in up to four PCTR watersheds over a two-year period. We analyzed the hysteresis between stream DOC and discharge to develop a seasonal model of subsurface hydrologic connectivity and DOC transport, and used field data to develop reach and sub-basin scale multivariate predictive models of stream CO_2 and CH_4 flux in the PCTR. Determining seasonal and spatial controls on stream DOC, CO_2, and CH_4 in this high-carbon region has critical implications for coastal marine ecology and the global carbon cycle, and will improve our ability to predict how these systems may be affected by environmental and climatic changes in the future.

Dedication

This thesis is dedicated to the interconnected biogeochemical webs that sustain all life on earth, which bring me repeatedly to a place of humility, awe, deep compassion, and respect. It is dedicated to all the earthly beings who are suffering because of the effects of anthropogenic climate change. It is finally dedicated to two of my greatest teachers, Micheal Elrick and Emmett Peters. May your spirits live on in the actions of those you inspired, and in the quiet songs of streams.

Acknowledgements

There were many people involved in this project who have contributed in some way to bring it its final state. I would like to acknowledge with deep gratitude my supervisor and mentor, Dr. Suzanne Tank. Suzanne demonstrates what it takes to excel in a scientific field every day, and she does it with kindness, grace and patience. Her guidance and mentorship on this project have been invaluable, and I will always be grateful for having had the opportunity to work with her. My scientific mentors were not few in this project, and I would like to also acknowledge and thank Kevin Devito, Mika Little-Devito, and Carl Mendoza for sharing their extensive hydrogeologic and wetland expertise with me; Vincent St. Louis for use of equipment and mentorship; Rachel Brown for her mentorship in teaching; and Andreas Hamann, Dante, and Melodie Kunegel-Brown for the time they spent helping me develop and troubleshoot R scripts. I would also like to extend my acknowledgement to the team at the Hakai Institute, without which there would be no data for this project. Thank you Shawn Hately, Rob White, Isabelle Desmarais, Maartje Korver, and Ian Giesbrecht, for exceptional dedication to producing top-tier research and data packages, and for leading by example in the professional environmental sciences. I would also like to thank my lab mates for their comradery, critiques, and time spent assisting me in so many ways. Thank you especially Sarah Shakil, Ryan Hutchins, Erin MacDonald, Nikki vanKlavern, and Scott Zolkos.

I would like to extend my deepest appreciation to my parents, Kate and Scot Bishop, who have always believed in my ability to achieve my dreams. Their financial, mental, and emotional assistance throughout this graduate degree have been unparalleled. I am so thankful for their unquestioning support of my endeavours and trust in my abilities (even when they entail traipsing through the coastal wilderness far from civilization!), as well as their willingness to

share their hard-earned wisdom. I am grateful for my grandmother, Lenore Mills, who has been a constant inspiration and reminder of what can be achieved when hard work, compassion, and a vision of a better world combine. I would also like to extend thanks to everyone in my wider Edmonton community who have supported me as I made this journey. Thank you especially to Alexander Fraser, Dylan George, Jess Cooper, Edrihan Levesque, the Zen Den, and Wych Haus. I could not have done this without your support.

Table of Contents

List of Tables

List of Figures

List of Abbreviations

30d – 30 day
3d – 3 day
7d – 7 day
A254 – Absorbance
API – Antecedent Precipitation Index
BC – British Columbia
BFI – Baseflow Index
C – Carbon
CART – Classification And Regression Tree
chA – Chemostatic, Anticlockwise
chC – Chemostatic, Clockwise
chN – Chemostatic, No hysteresis
C-Q – Concentration-Discharge
CWH – Coastal Wet Hemlock ecozone
CWHvh2 – Coastal Wet Hemlock Very Wet Hypermaritime subzone 2
D – Dry
DA – Dilution, Anticlockwise
DC – Dilution, Clockwise
DD – Drainage Density
DN – Dilution, No hysteresis
DOC – Dissolved Organic Carbon
DOM – Dissolved Organic Matter
DY – Drying
FA – Flushing, Anticlockwise
FC – Flushing, Clockwise
fDOM – fluorescent Dissolved Organic Matter
FI – Flushing Index
FN – Flushing, No hysteresis
G – groundwater
GIS – Geographic Information System
H-BGC - Hydro-Biogeochemical Cycle
HI – Hysteresis Index
k – gas transfer velocity

k_2 – reaeration coefficient
LiDAR – Light Detection and Ranging
Lm – Mainstem length
Lt – total stream network length
MAP – Mean Annual Precipitation
MxFlwpth – maximum flowpath length
NDVI – Normalized Difference Vegetation Index
NPCTR – Northern Pacific Coastal Temperate Rainforest
NPP – Net Primary Production
OC – Organic Carbon
P – Pool
POC – Particulate Organic Carbon
Q – Discharge
R – Riffle
RDA – Redundancy Analysis
RW – Re-Wetting
S – Steady
SE – soil event runoff water
SO – soil groundwater
SOC – Soil Organic Carbon
SO_H – soil groundwater with high connectivity
SO_L – soil groundwater with low connectivity
SOM – Soil Organic Matter
US(A) – United States (of America)
USGS – United States Geological Survey
VRM – Vector Ruggedness Matrix
W – Wet
WS – Watershed
YSI – Yellow Springs Instrument

1.0 General Introduction

Rivers and streams play a key role in the global carbon cycle as biogeochemical conduits in the landscape (Martin and Meybeck, 1979; Newbold, 1982), as well as sources of atmospheric CO_2 (Mayorga et al., 2005; Butman and Raymond, 2011, Raymond et al., 2013). With an annual global flux estimated at $0.4x10^5$ gC (Bernhardt and Schlesinger, 2013), rivers connect spatially distinct carbon stores by transporting and transforming particulate organic matter (POM), and dissolved organic carbon (DOC) in the form of dissolved organic matter (DOM), through terrestrial to freshwater and marine environments (Lauerwald et al., 2012; Smith et al., 2013; Raymond and Spencer, 2015). Stream DOC influences light attenuation, photo-reactivity (Bertilsson and Tranvik, 2000), primary production, ecosystem metabolism (Fisher and Likens, 1973), energy budgets, bacterial respiration and decomposition (Tank et al. 2010), inorganic nutrient mineralization, and food web structure (Ylostalo et al. 2016, Traving et al. 2017).

The composition of DOC strongly influences bacterial metabolism, and different sources of DOC are metabolized at different rates depending on their molecular composition (Berggren and del Giorgio, 2015). Autochthonous DOC in the form of DOM is generated internally within river ecosystems by algal and macrophytic photosynthesis (Findlay and Sinsabaugh, 2003), whereas allochthonous C is input from external sources including microbial degradation of soil organic material, root respiration, and litterfall (Meyer et al., 1998). Within aquatic systems, autochthonous DOC is usually characterized by labile, bioavailable, low molecular weight compounds such as carbohydrates, lipids and proteins (Mayorga et al., 2005; Yang et al., 2016). Allochthonous DOM is typically composed of complex, aromatic, high-molecular-weight molecular compounds with low bioavailability, such as lignin found in plant material, and hydrophobic organic acids found in soils (Weishaar et al., 2003, Seifert et al., 2016). However, the age of allochthonous DOC is a factor of biolability, as fresh, humic DOC (eg. forest litter) can be preferentially metabolized compared to older DOC from peatlands (Berggren and del Giorgio, 2015). Allochthonous DOM usually dominates small headwater streams due to the influx of leaf litter and other organic materials, coinciding with the river-continuum concept (Vannote et al. 1980). During transport, DOM can be transformed or removed from riverine ecosystems through microbial decomposition and respiration, photo-oxidation, sorption to metal-oxide compounds, and flocculation to sediment particles (Raymond and Spencer, 2015, Couturier et al. 2016).

The study of hysteresis dynamics between stream discharge and DOC provides a unique opportunity to further our knowledge of the hydro-biogeochemical processes that form the basis of watershed-scale carbon cycling and lateral C transport processes. Assessing these hysteresis trends can advance our understanding of DOC source distribution and subsurface hydrology, allowing for the development of predictive, mechanistic terrestrial-aquatic C cycling models that are increasingly critical in the context of global anthropogenic climate change. Previous research has demonstrated that stream discharge exhibits a significant positive, non-linear correlation with stream DOC concentration (Lundquist et al., 1999; Mladenov et al., 2005; Raymond and Saiers, 2010; Emili and Price, 2013; Strohmeier et al., 2013). The majority of terrestrial DOC export occurs during rapid hydrologic events where a large quantity of water is input to the landscape over a short period of time, i.e. storms or spring snowmelt (Raymond and Saiers, 2010). The non-linearity of the relationship between DOC and discharge creates a cyclical pattern known as hysteresis (Figure 1.1) (Hendrickson and Krieger, 1964; Toler and Ocala, 1965; Lloyd et al. 2015), where DOC concentrations loop in a clockwise (peak DOC on the rising hydrograph limb) or counterclockwise (peak DOC on the falling hydrograph limb) direction, or in both directions in a “figure-of-eight” formation (Zuecco et al., 2016). The slope of the hysteresis loop has been used to identify the DOC concentration gradient through the duration of the storm event (Figure 1.1) (Vaughan et al. 2017; from Butturini et al. 2008).

Various mechanisms have been hypothesized as potential controls on temporal hysteresis relationships between DOC and discharge, with an emphasis on shallow-subsurface moisture and flowpath connectivity (Lloyd et al., 2015; Outram et al., 2016; Tunaley et al., 2016). Clockwise hysteresis has been attributed to the build-up of DOC in shallow, sub-surface soil pore waters during dry conditions, and rapid flushing when a storm event initiates local hydrologic connectivity through precipitation infill and pore-water displacement (Mladenov et al., 2005; Saraceno et al., 2009). Anticlockwise hysteresis has been modeled as the result of delayed DOC contributions to local flowpaths, due to full hydrologic connectivity only occurring at maximum catchment flow (Inamdar et al. 2004). The slope of the hysteresis loop demonstrates either a flushing, dilution, or chemostatic DOC response, which can be indicative of soil DOC transport availability and/or DOC source proximity (Vaughan et al. 2017; from Butturini et al. 2008). Flowpath mixing models have been used to determine groundwater, antecedent moisture, and lateral subsurface riparian flowpaths as significant controls on temporal trends in DOC concentration (Elder et al., 2000; Strohmeier et al., 2013; Seifert et al., 2016; Tunaley et al., 2016), whereas stream size and surface flow have been identified as less influential controls (Fellman et al., 2013). Coupled hydrologic-biogeochemical models have been developed and tested successfully to utilize the predictive capacity of the DOC-discharge relationship (Birkel et al., 2013; Dick et al., 2015; Birkel et al., 2017). In addition to hydrologic variables, the temporal trends and quantity of allochthonous stream DOC can be influenced by landscape factors such as ecosystem type (Vaughan et al., 2017; Emili and Price, 2013) and climatic factors such as seasonal temperature variability (Saraceno et al., 2009; Strohmeier et al., 2010, Futter et al., 2011).

Precise quantification of the non-linearity between DOC concentration and discharge has until recently been limited by coarse data resolution from periodic grab sampling programs (Fellman et al., 2013). The advent of digital technology in the late 1990's to early 2000's caused a major transition in the field of biogeochemistry towards automated, *in situ* sampling (Meinson et al. 2016). The introduction of *in situ* fluorescent DOM (fDOM) sensors to freshwater DOM research has provided continuous, high-frequency data which capture event discharge and DOC dynamics at previously unavailable temporal resolutions (i.e., minute, hourly, and daily timestep intervals) (Pellerin et al., 2011, Ruhala and Zarnetske, 2016; Rode et al., 2016). However, *in situ* fDOM sensor output readings are highly sensitive to certain environmental variables, including temperature due to the process of thermal quenching (Baker, 2005; Watras et al., 2011; Downing et al., 2012), turbidity due to the attenuation of light by suspended particles (Saraceno et al., 2009; Lee et al., 2015), and absorbance ("inner-filter effects") by chromophores in DOM compounds (Downing et al., 2012; Wilson et al., 2013). To effectively use *in situ* fluorescence sensor output, corrections for the inaccuracies caused by these variables are necessary (McKnight et al, 2001).

Another important component of the global carbon cycle is the emission of greenhouse gases, such as CO_2 and CH_4, from inland freshwaters. Global inland freshwater CO_2 emissions are estimated at an annual rate of 3.9 PgC (Drake et al., 2018), and global inland freshwater CH_4 emissions are estimated at ~0.075 PgC yr^{-1} (Bastviken et al. 2011). Sinks of dissolved stream CO_2 gas include uptake by photosynthetic organisms (Jones and Mulholland, 1998). Sources include root respiration and DOC mineralization via bacterial respiration in the stream and in adjacent riparian soil pore water, which in turn contribute to freshwater CO_2 emissions or atmospheric evasion (Mayorga et al., 2005; Waterloo et al., 2006; Berggren and del Giorgio, 2015). As seasonal climatic and hydrologic patterns transform due to global climate change, it is critical to identify controls of the atmospheric evasion of dissolved CO_2 and CH_4 to determine the influence of this potentially significant component of the carbon cycle on global climate feedback dynamics (Raymond et al., 2013).

The aim of this thesis was twofold, broadly investigating lateral stream DOC transport and stream greenhouse gas emissions (CO_2 and CH_4). Specifically, our objectives were to:

1) Assess the utility of automated, *in situ* fDOM sensors for modelling stream DOC; use the resulting high-resolution DOC dataset to determine the seasonal variation in and controls on event-based lateral DOC transport via hysteresis analysis; and create a mechanistic conceptual model of seasonal lateral DOC transport in our study region.
2) Determine the spatial variation in and controls on dissolved stream CO_2 and CH_4 partial pressures and efflux at both the reach and sub-basin scale; and to compare the relative predictive strengths of our models at each scale.

This study was situated on Calvert and Hecate Islands in the Northern Pacific Coastal Temperate Rainforest (NPCTR), off the central Pacific coast of British Columbia, Canada (Lat 51.650, Long -128.035). Recently, stream DOC export in this region has been assessed through a grab sampling program as being very high, primarily allochthonous, and highly aromatic (Oliver et al., 2017). That study proposed that organic-rich upland forest soils and organic material contributions from abundant peatlands are key factors in the production of high annual stream C exports. However, a quantitative evaluation of the seasonal and spatial controls on lateral and atmospheric stream C exports in this high-carbon region has not yet been conducted.

1.1 Figures

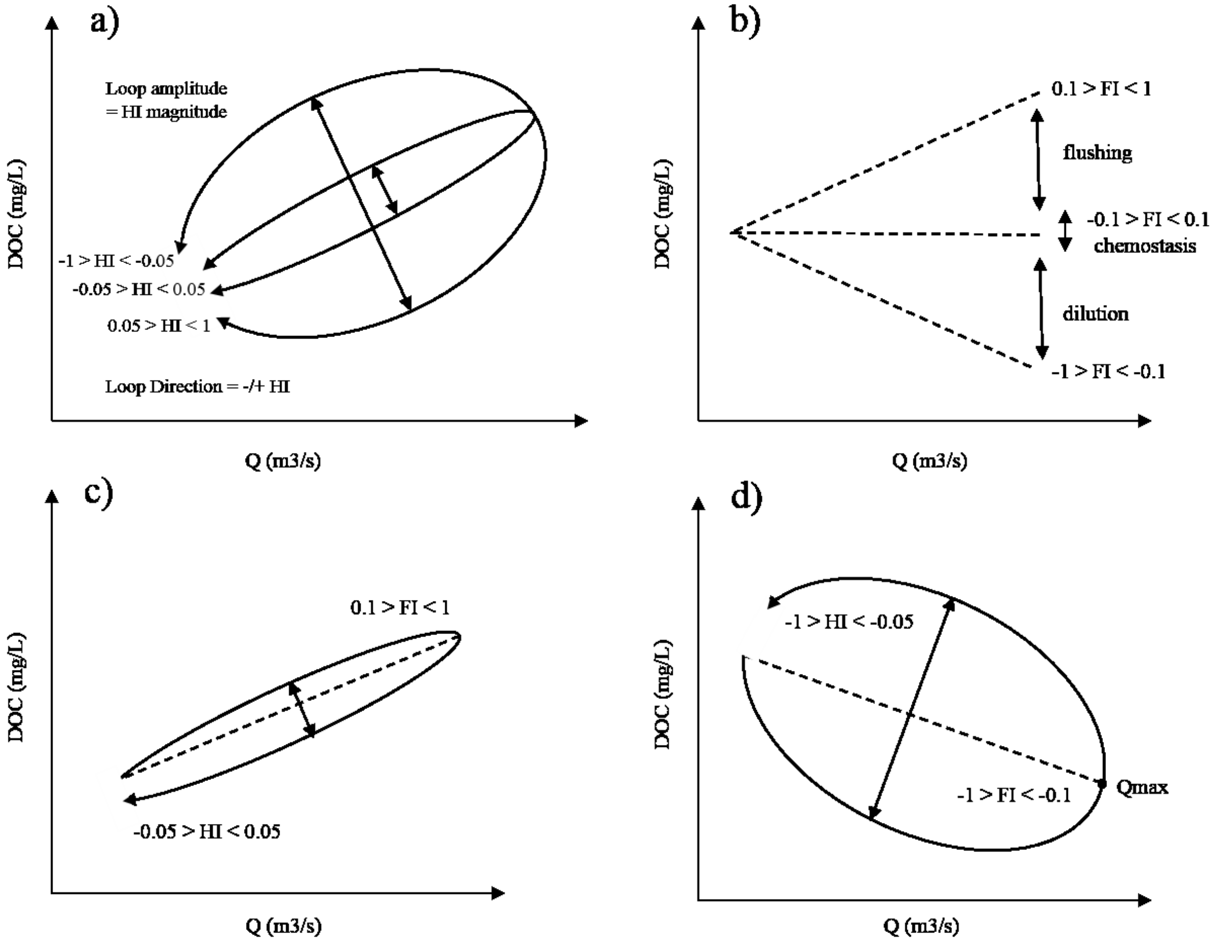

Figure 1.1: Conceptual models of flushing index (FI) and hysteresis index (HI) range and thresholds (Aguilera and Melack, 2018), and schematic examples of different event types. a) HI threshold ranges based on loop direction and amplitude, which correspond to HI sign (-/+) and magnitude: clockwise (0.05 < HI < 1), anticlockwise (-1 > HI > -0.05), and no hysteresis (-0.05 > HI < 0.05); b) FI threshold ranges based on FI slope, which corresponds to FI sign (+/-) and magnitude: flushing (0.1 < FI < 1), dilution (-1 > FI > -0.1), and chemostasis (-0.1 > FI < 0.1); c) a schematic example of a flushing, no hysteresis event (FN); d) a schematic example of a dilution, anticlockwise event (DA).

2.0 Seasonal dynamics and controls on DOC transport in the high-carbon region of the northern Pacific Coastal Temperate Rainforest

2.1 Introduction

Fluvial systems (hereafter "streams") are biogeochemical catalysts in the global carbon cycle. They connect spatially distinct carbon stores in terrestrial ecosystems, the ocean, and the atmosphere, and transform carbon between organic and inorganic forms (Aufdenkampe et al., 2011; Newbold, 1982; Martin and Meybeck, 1979). A portion of soil- and stream-derived dissolved organic carbon (DOC) is delivered to the oceans, where it supports coastal ecosystems as an energy source (Bernal et al., 2018; Cole and Caraco, 2001). Another portion of stream DOC is emitted to the atmosphere as CO_2 via in-stream microbial mineralization (Rasilo et al., 2017). Thus, understanding the processes that govern streamwater DOC has both ecological and climatic implications, over a variety of scales (Johnston et al., 2018; Moody et al., 2013).

Stream DOC can be produced autochthonously via primary production, or it can be derived from terrestrial primary production that is transported to the stream via subsurface runoff pathways. In small watersheds and headwaters, the of terrestrially-derived DOC typically outweighs that of autochthonous origin (Tank et al., 2010; Findlay and Sinsabaugh, 1999; Creed et al. 2015). As such, small headwater streams are the predominant pathway by which a portion of terrestrial NPP is diverted from soil sequestration and returned to marine or atmospheric stocks for continued cycling (Lauerwald et al., 2015). Indeed, recent work points to an overarching influence of NPP on stream DOC export at a regional landscape scale (Hutchins et al., 2019). The extent to which aquatic flowpaths divert terrestrial NPP and affect marine and atmospheric carbon cycling is primarily influenced by underlying hydrologic and climatic factors, however. Understanding controls on soil-derived stream DOC transport and export therefore lays the foundation for predictive models of coastal ecology and stream CO_2 emissions under various climate change scenarios.

Previous research has demonstrated that stream DOC concentrations are related to discharge and that DOC export is episodic, following pulses of discharge from hydrological events such as storms and snow melt (Mladenov et al., 2005; Raymond and Saiers, 2010; Strohmeier et al., 2013). During storm events, the orientation of peak DOC to peak discharge can provide insight into the subsurface hydrology and flowpaths controlling soil-derived stream DOC concentrations. This orientation, when plotted on a biplot of discharge and DOC or a “C-Q plot”, is represented by a characteristic hysteresis “loop” in a clockwise or anticlockwise direction where the change in concentration over the duration of the event is represented by the loop’s slope (Hendrickson et al., 1964; Toler, 1965, Williams, 1989; Long et al., 2017). Several indices have been developed to quantify event hysteresis characteristics from C-Q plots, including ΔC (Butturini et al. 2006; Butturini et al., 2008) or the similarly-derived flushing index (FI; Vaughan et al. 2017), which assesses the change in concentration over the course of the event, and the hysteresis index “HI”, which assesses the direction and magnitude of the hysteretic loop (Lloyd et al., 2016b) (Figure 1.1). The direction and slope of hysteresis loops have been correlated with various subsurface hydrologic flowpaths, and models of subsurface DOC transport (Evans and Davies, 1998; Butturini et al., 2006; Butturini et al., 2008; Zuecco et al., 2016), making them a useful tool for developing mechanistic models of soil-derived stream DOC transport and the factors controlling stream DOC concentrations over time (for example, Long et al., 2017). Aside from soil-derived stream DOC research, hysteresis analyses of heavy metals dynamics (Rodriguez-Blanco et al., 2018), trends in suspended sediment (Ziegler et al., 2016), various nutrients such as NO_3^- (Cerro et al., 2014), NH_4^+, and PO_4^{3+} (Aguilera and

Melack, 2018), and total N and P (Outram et al., 2016), and ions such as Ca^{2+} (Rose et al., 2017) are becoming increasingly prominent.

When considering HI, anticlockwise hysteresis is typically considered the result of a time delay, caused by an initial first flush of diluted runoff at the beginning of an event followed by DOC-rich inputs, often from wetlands (Fovet et al., 2013; Knorr et al., 2013), or by the expansion of the riparian saturated zone to connect previously isolated DOC sources, such as hillslopes, to subsurface flowpaths (Inamdar et al., 2004; Tunaley et al., 2016). Typically, widespread, unlimited DOC sources throughout the catchment are thought to result in anticlockwise hysteresis (Coch et al., 2018, Rose et al., 2017). Conversely, clockwise hysteresis is indicative of subsurface hydrologic isolation, where immediate flushing of proximal, limited DOC-rich water is transported to the stream via shallow, subsurface flowpaths once a critical saturation threshold is reached (Birkel et al., 2017). Soil "wetting up time" has been proposed as a control on the amplitude of hysteresis loops, which indicates the strength of the hysteresis trend, or how coincident solute and discharge peaks are (Eckard et al., 2017). When considering ΔC or FI, dilution is typically thought of as a response to high hydrologic connectivity within the lateral, subsurface flowpath network and is thus associated with DOC stores that are distant from the stream. Flushing is considered as the result of DOC build-up in the soil during an antecedent dry period, and is also associated with DOC stores that are in close proximity to the stream (Vaughan et al. 2017). These concepts were initially proposed in conceptual models, which have been followed by studies using stable isotope observations (Tunaley et al., 2016), rainfall-runoff models (Birkel et al., 2014), and changes in DOC concentration relative to reference samples (Birkel et al., 2017; Eckard et al., 2017). Within regions, these studies have validated the ties between hysteresis characteristics, subsurface hydrologic dynamics, and seasonal controls on soil-derived DOC transport.

Common predictors of hysteresis characteristics and thus stream DOC export include antecedent precipitation and soil moisture conditions (Knorr et al., 2003; 2013; Tunaley et al., 2016; Fovet et al., 2018), as well as groundwater table depth (Emili and Price, 2013; Dick et al., 2015; Osburn et al., 2018). These predictors have been found consistently across a variety of ecosystems, including wetlands (Knorr et al., 2013), upland forest streams (Pellerin et al., 2012), seasonally frozen rivers (Kamari et al., 2018) and agricultural, urban, and forested watersheds (Vaughan et al., 2017; Fovet et al., 2018). In addition, seasonality has been shown to exert a strong influence on loop direction and event DOC concentration (Pellerin et al., 2012; Birkel et al., 2014). Generally, in temperate watersheds in eastern North America, storm events in summer encapsulate the largest stream DOC responses, winters exhibit subdued responses, and freshet in late winter-spring demonstrate increasing DOC responses leading into peak summer DOC (Connecticut; Schultz et al., 2018). However, some regions experience peak DOC in late summer-Fall, likely due to the accumulation of soil DOC during a drier summer period and subsequent transport at the onset of Fall precipitation (New Hampshire; Wilson et al., 2013; Koenig et al., 2017). Although some studies have been unable to attribute any significant predictors to hysteresis loop direction and change in event concentration (Butturini et al., 2006; Butturini et al., 2008), determining the influence of explanatory variables on hysteresis descriptors across multiple events is an avenue to understand what controls soil-derived DOC transport to streams, DOC sources, preferential flowpaths, and their seasonal dynamics.

Here, we work to understand seasonal variation in stream DOC export dynamics in the Pacific Coastal Temperate Rainforest (PCTR) ecoregion of North America. The PCTR has previously been identified as a potential global DOC export hotspot due to its moderate temperatures and extremely high precipitation, which combine to slow soil decomposition rates and produce thick, organic-rich topsoils (McNicol et al., 2019). Previous work has identified the PCTR ecoregion as a DOC export hotspot in global carbon models (Mayorga et al., 2010), and that streams draining small, hypermaritime watersheds at our PCTR study site exhibit globally-significant yields of terrestrial DOC (~50 MgC km^{-2}) (Oliver et al., 2017). Determining the controls on stream DOC export will further our knowledge of how climate change might affect stream DOC export in this carbon-rich region. By assessing seasonal variation in storm event hysteresis dynamics, and correlating hysteresis characteristics with environmental variables, we can develop a conceptual model of subsurface, soil-derived stream DOC transport in the PCTR and its variation. This lays a foundation to understand how climate change may affect stream DOC flux, and in turn coastal ecosystems, in the high-carbon region of the PCTR.

We undertook this work using high-frequency, *in situ* fDOM sensors (Rode et al., 2016) to assess trends in hysteresis characteristics at event to inter-annual timescales. Our objective was to develop a hydro-biogeochemical conceptual model where the seasonal dynamics and environmental controls on soil-derived stream DOC transport and flux are identified within the PCTR. Our main research questions were: 1) What are the main trends in hysteresis characteristics at event-specific and seasonal timescales?; 2) What are the primary environmental and catchment-scale controls on hysteresis characteristics?; and 3) Can a hysteresis-based, hydro-biogeochemical conceptual model be developed to understand subsurface DOC transport in wet, coastal temperate rainforests?

2.2 Methods

2.2.1 Study Site

This study took place across four small watersheds on Calvert and Hecate Islands, situated on the central coast of British Columbia, Canada (51.650˚N, 128.035˚W; Figure 2.1). Calvert and Hecate Islands are part of the North Pacific Coastal Temperate Rainforest (NPCTR) ecosystem (50°N - 58°N), the largest contiguous stretch of coastal temperate rainforest in the world stretching from California through British Columbia to Alaska (Kellogg et al., 1995). Coastal temperate rainforest ecosystems are distinguished by certain key features: ocean proximity, coastal mountains, cool summer temperatures, and high precipitation across all seasons (Weigand, 1990). The bulk of the North American coastal temperate rainforest has either a perhumid or seasonal humid climate, with moisture indices above zero (annual precipitation > potential evapotranspiration; Thornthwaite, 1948). A perhumid climate exhibits summer rainfall above 10 percent of the annual total with a mean annual temperate of 7˚C, whereas a seasonal humid climate exhibits summer rainfall below 10 percent of the annual total and a mean annual temperature of 10˚C, with periodic droughts and summer fires (DellaSalla, 2011). The North American PCTR specifically has the highest biomass accumulations and some of the highest rates of productivity of forest ecosystems in the world (Barbour and Billings, 2000), as well as extremely large stocks of soil organic carbon (SOC) (McNicol et al. 2019).

Within the perhumid NPCTR, Calvert and Hecate Islands are largely classified biogeoclimatically as a "Very Wet Hypermaritime" subzone (CWHvh2), the wettest in the Coastal Western Hemlock zone (CWH) of British Columbia (Pojar et al., 1987; Green, 2014). This subzone has an annual average of 220 days of precipitation, and the dominant soils are poorly drained podzols, organic-rich upland folisols, mineral gleysols due to extended saturation, as well as thick organic wetland soils such as fibrisols, mesisols, and humisols (Banner et al., 2005). Even within the NPCTR, Calvert and Hecate Islands represent an extreme end of the climate spectrum with an annual precipitation of 3414 mm yr^{-1} at sea level and 4529 mm yr^{-1} at the maximum elevation of 1045 m on Mount Buxton from 1981-2010 (Wang et al. 2016; from ClimateBC). Seasons on Calvert and Hecate Islands have been defined by two hydrologically distinct periods: wet (September – April) and dry (May – August) (Oliver et al., 2017). Temperatures are moderate and cool, with a mean annual temperature of 8.3°C at sea level and 5.9°C at maximum elevation from 1981-2010 (Wang et al. 2016; from ClimateBC). Precipitation is primarily comprised of rainfall with only 141 mm yr^{-1} of snow at sea level, but as much as 632 mm yr^{-1} at maximum elevation (Wang et al. 2016; from ClimateBC). Terrestrial ecosystems on Calvert and Hecate Islands reflect the local climate, topography, soils and parent material. Watersheds are dominated by varying proportions of wet-moist zonal forests, bog forests, bog woodlands, and blanket bog complexes (Green, 2014; Thompson et al., 2016). Geology is predominantly granodiorite and quartz diorite bedrock intrusions with some alluvial and glacial deposits (Roddick, 1996). Topographic relief is generally low, characterized by rolling inland hills, with steeper terrain leading to higher elevations of the headwaters. The predominantly gentle terrain, high precipitation, and moderate temperatures together produce thick accumulations of organic matter on the forest floor and support the widespread development of peatlands (Banner et al., 2005).

Four watersheds (WS) were chosen as study sites for this project, nested within a long-term watershed and critical zone observatory operated by the Hakai Institute: WS 703, WS 708, WS 819, and WS 1015 (Figure 2.1). Our study period extended from August 2015 – December 2016. Each watershed is similar in its organic topsoil depth, small area, and dominant ecosystem cover at a regional scale, however there are variations in total water yield, mean slope, lake coverage, soil depth, watershed area, and ecosystem mosaic at the watershed and sub-basin scale, which can affect biogeochemical processing in the study streams (Table 2.1; Oliver et al. 2017, Levy Booth et al. 2019).

2.2.2 Stream Sensor Network

Automated, continuous, *in situ* biogeochemical sensors were installed in the stream outlets of each study watershed. fDOM sensors (Turner Designs Cyclops 7, excitation/emission wavelengths = 370/425nm) were paired with a turbidity sensor (Cyclops Submersible Sensor) and water temperature sensor (OTT Hydromet Pressure Level Sensor) to ensure accurate correction of fDOM sensor outputs. fDOM and turbidity sensors were installed in WS 708 in July 2014, and installed in WS 1015, 819, and 703 in July 2015. Each fDOM and turbidity sensor was equipped with a wiper to prevent biofilm accumulation. The fDOM and turbidity sensors were calibrated annually, and fDOM outputs were corrected for turbidity, temperature and inner filter effects (see below and Appendix). Additional in-stream measurements included stage (OTT Hydromet Pressure Level Sensor) and discharge via the auto-salt dilution method (Korver et al. 2019). 5-minute discharge rating curves use the Lowess distribution (Korver et al., 2019).

2.2.3 Additional ancillary data

Precipitation and air temperature were monitored at various meteorological stations on Calvert and Hecate Islands. Data were collected at a station located on the eastern ridge separating WS 708 and WS 703 for WS 708; and near the watershed outlets for WS 703, WS 819, and WS 1015 (Figure 2.1). Precipitation and air temperature were measured every 5 seconds, with a mean of this 5 second data being recorded every 5-minutes. Antecedent precipitation was calculated from this precipitation data (see below for further details). DOC concentration and dissolved organic matter (DOM) absorbance were measured by periodic grab sampling. DOC samples were preserved with 7.5 M H_3PO_4 and analyzed using a total organic carbon analyzer (Aurora 1030; OI Analytical; Oliver et al., 2017). Absorbance was determined on site using a spectrofluorometer (Aqualog, Horiba Instruments Inc.). Absorbance scans were conducted between 200 and 800 nm using a 1 cm quartz cell, with readings baseline corrected as outlined in Oliver et al. (2017). Watershed-scale spatial predictors were extracted in ArcGIS from the Hakai Watershed LiDAR layer (Gonzalez-Arriola, 2015) and included watershed area, mean elevation, mean slope, main channel length, total stream network length, drainage density, maximum flowpath length, mean NDVI, mean gap fraction (canopy cover), waterbody cover, and wetland cover (Table 2.1).

2.2.4 fDOM Sensor Corrections

fDOM sensors were corrected for temperature, turbidity, and inner filter effects in a stepwise correction process based on the methods of Watras et al. (2011) and Downing et al. (2012). The corrected fDOM sensor measurements were converted to an inferred DOC concentration via linear regression with lab DOC measurements (Figure 2.2). Throughout this paper, we refer to true (lab analyzed) DOC concentrations as “DOC”, and inferred sensor-derived DOC concentrations as “DOC_{sensor}”. For further details on these methods see Appendix 1.

2.2.5 Event and Event Peak Selection

We developed a semi-quantitative method of storm event selection to compare DOC_{sensor} dynamics across storm events, which involved a combination of automated selection and visual assessment. Baseflow was delineated using the online modelling tool SepHydro (Danielescu et al., 2018), which applies various digital recursive filters to the discharge timeseries. Discharge measurements were input to SepHydro at hourly intervals, as baseflow was overestimated at the 5-minute data interval. Storm event periods for discharge and DOC_{sensor} at the hourly interval were selected automatically by a written loop in R (R Core Team, 2013) using the criteria in Lloyd et al. (2015): Storm event starts were defined as the (hourly) point on the rising hydrograph limb where the discharge was greater than 20% of the total baseflow component; and storm event ends were defined on the decreasing hydrograph limb where the net decrease in discharge was greater than 20% of the total baseflow component.

In SepHydro we applied a digital recursive filter to our hourly interval data developed by Eckhardt et al. (2005), which calculates the baseflow index (BFI) as a second parameter to complement the primary baseflow separation parameter (alpha) used in previous models (Lyne and Hollick, 1979; Arnold and Allen, 1999). The dual-parameter Eckhardt et al. (2004) filter was chosen because a second parameter increases robustness, and because this filter provided BFI and alpha levels that were calculated and field-verified for watersheds of various sizes and substrates (Eckhardt et al., 2005). To delineate baseflow, we selected a BFI (0.71) and alpha level (0.98) from the Atlantic coastal northeastern Beaverdam Creek study site calculated during April 1950-March 1952, as it was the smallest (50 km^2) perennial watershed with the largest mean annual precipitation (1075 mm) that had been assessed for these criteria (Eckhardt et al., 2005).

Upon visual assessment of the automatically-selected hourly storm event periods, we determined that the criteria from Lloyd et al. (2016b) performed well for large, distinct, isolated storm events, but resulted in a high degree of inaccuracy for clusters of consecutive storm events ("event series"), and for storm events at low discharge levels. Therefore, a second set of selection criteria were developed to inform the manual adjustment of automated selection periods for event series and low discharge storms. Event starts were manually selected where discharge began to increase after a constant baseline of greater than 2 hr duration on the rising limb, and end points were manually selected where discharge returned to pre-event Q, or at the first hourly interval of a constant baseline greater than 2 hr on the falling limb (Appendix 1).

2.2.6 Hysteresis Analysis

For each hourly-selected storm event period, the 5-minute interval discharge and DOC_{sensor} data were selected and normalized from zero to 1 according to Lloyd et al. (2016b). The hysteresis index (HI) and flushing index (FI) were calculated following Lloyd et al. (2016b) and Vaughan et al. (2017; see also Butturini et al. 2008), respectively (Figure 1.1). The HI ranges from -1 to 1, where negative values indicate anticlockwise hysteresis, positive values indicate clockwise hysteresis, and a value of zero or close to zero (-0.05 to 0.05) indicates no hysteresis. The absolute magnitude of the HI describes the amplitude of the hysteresis loop, or how coincident peak DOC and peak discharge are. FI also ranges from -1 to +1, with the magnitude of this index indicating the direction of the relationship between DOC_{sensor} concentration and discharge, and thus the concentration gradient between DOC_{sensor} source areas and the stream (see above). Negative FI values indicate DOC_{sensor} dilution, positive FI values indicate DOC_{sensor} flushing or accretion, and FI values at or close to zero (-0.1 to 0.1) indicate chemostasis. Further details on HI and FI calculations are provided in Appendix 1.

2.2.6 Antecedent Precipitation Index

Antecedent precipitation is often used as a proxy for antecedent soil moisture conditions when soil moisture data is unavailable. Precipitation data were collected from the meteorological stations as described previously. We calculated an antecedent precipitation index following the methods of Saxton and Lenz (1987) from Lloyd et al. (2016a):

$$\mathrm{API}_j = \mathrm{K}(\mathrm{API}_{j-1} + \mathrm{P}_{j-1}) \tag{3}$$

Where j is the time step in days, P is the daily precipitation (mm), and K is a decay coefficient controlled by evapotranspiration. We used a K decay coefficient value of 0.929, derived from a model developed in a small watershed (Deer Creek, 300 ha) in the high streamflow Cascade mountain region of western Oregon, US. Deer Creek is within the PCTR and has a similar climate, and its small size is comparable to our study watersheds (Fedora and Beschta, 1989).

2.2.7 Statistical Analyses

We delineated our timeframes using the classic Julian day calendar for each year, and using Spring, Summer, Fall, and Winter for each season. We delineated seasons based on the typical 3-month periods (Spring = March, April, May; Summer = June, July, August; Fall = September, October, November; and Winter = December, January, February), adjusted to reflect that season's dominant hydrograph trend; shifting the summer season to coincide with the beginning of the dry season during our study period (April 1) and end at the start of Fall rains (August 26) (Spring = March; Summer = April - August 26; Fall = August 27 - November; Winter = December - February). For example, Summer begins in April, as this month is relatively dry and has rainfall similar to the rest of the summer months, and ends on August 26, as that is the last dry day before the characteristic fall rains begin (Figure 2.3).

Seasonal trends in FI and HI were assessed qualitatively and quantitatively for the four study watersheds. Trends were assessed qualitatively through visual inspection of biplots of FI and HI, and variation in these indices across months and seasons. We tested the various combinations of FI and HI, as well as FI and HI individually, for significance between months, seasons, and watersheds using the Kruskal-Wallis test, using the *kruskal.test* and *kruskalmc* functions from the *pgirmess* package in R (R Core Team, 2013). We assessed chemodynamism, which is conceptually similar to the FI as it expresses the hydrologic sensitivity of solute transport, using concentration-discharge (C-Q) plots following Godsey et al. (2009). We compared annual and seasonal C-Q plot slopes to the chemostatic/chemodynamic threshold levels outlined in Bieroza and Heathwaite (2015). The C-Q plot slopes were calculated on a logarithmic scale, and chemostatic responses were assigned to slopes that fell between -0.1 and 0.1.

To understand controls on HI and FI, predictor and response variables were input to an RDA ordination. Predictor variables included climatic, environmental and watershed-scale spatial data. The climatic and environmental predictors included mean temperature per event, precipitation per event, the antecedent precipitation index (API) for 3, 7, and 30 days prior to the event (as a proxy for soil moisture) (Table 2.2). The spatial, watershed scale predictors input to the RDA are identical to those described in Section 2.2.3 (Table 2.1).

We input categorical response variables of combined FI and HI classes to a Classification and Regression Tree analysis. Our response variables included chN (chemostasis, no hysteresis), DN (dilution, no hysteresis), FN (flushing, no hysteresis), DA (dilution, anticlockwise hysteresis), DC (dilution, clockwise hysteresis), FA (flushing, anticlockwise hysteresis), and FC (flushing, clockwise hysteresis) (E.g. Figure 1.1), with predictor variables identical to those described for the RDA above. CART models evaluate various thresholds in the predictor dataset to determine the first split that explains the most variation in the response variable. After the first threshold is determined, the CART model repeats for each sub-group in the tree until no additional significant variation can be explained. To conduct our CART analysis, we used the *ctree* function from the *partykit* package in R (R Core Team, 2013).

2.3 Results

2.3.1 Sensor Calibrations

fDOM sensors were corrected for temperature, turbidity, and inner filter effects through watershed-specific standard rating curves that were developed annually. The quenching effect of temperature on fDOM sensor output was corrected for using the methods in Watras et al. (2012) ($R^2 > 0.99$ in all cases for calibration in 2015; Figure A1.1). Turbidity sensors were calibrated with standardized turbidity solutions to create linear rating curves ($R^2 = 1$ in all calibration cases for 2015; Figure A1.2), and fDOM was corrected for turbidity using standard rating curves fit to linear models of the reciprocal of signal loss (%) (i.e., compensating signal gain) and turbidity concentration ($R^2 = 1$ in all cases for calibration in 2015; Figure A1.3). Inner filter effects were corrected for using standard rating curves developed using a Suwanee River organic matter standard and the fDOM sensor output ($R^2 > 0.99$ in all cases; Figure A1.6). After these corrections were applied to the fDOM sensor output in a stepwise manner, the final relationships between watershed-specific fDOM sensor outputs and DOC_{sensor} were linear, with slope coefficients approximately at 1 and a combined $R^2 = 0.74$ across all watersheds (Figure 2.2) ($R^2 = 0.89$, 0.65, 079, and 0.42, for WS 703, 708, 819, and 1015, respectively; Figure A1.8).

2.3.2 Monthly Hysteresis Trends

Stream DOC outlet concentrations generally followed catchment outlet hydrographs, reinforcing the relationship between DOC and discharge. There are several instances of elevated DOC concentrations during storm events across all watersheds during mid-summer, but levels remain relatively low until fall precipitation begins in earnest (Figure 2.3) (see also Oliver et al. 2017). Stream DOC began to decrease across all watersheds beginning in early Winter and continued to decrease through late Winter and Spring. Our use of continuous sensor data was able to substantially improve the overall representation of storm event dynamics for these study streams, which were previously documented using grab sample data (Figure 2.3, Oliver et al., 2017).

Regardless of season, all watersheds had more dilution relative to flushing events, as shown by the FI (Vaughan et al., 2017 from Butturini et al., 2006), and more anticlockwise relative to clockwise events, as demonstrated by the HI (Lloyd et al. 2016) (Figure 2.4; Table 2.3). Most storm events with a dilution, anticlockwise response (DA; low FI, low HI) occurred in the Fall, whereas storm events with a flushing, clockwise response (FC; high FI, high HI) predominantly occurred in the Summer with the exception of watershed 819 (Figure 2.4). The proportion of different combinations of FI and HI varied across watersheds, however across all watersheds the most common response was DA (Figure 2.5; Table 2.3). Events with a DA response were most prevalent in watersheds 703, 819, and 1015, whereas storm event responses were distributed more evenly in WS 708 (Figure 2.4).

On a monthly basis, the proportion of events exhibiting a dilution response (DA and DC) generally followed annual trends in storm event count for our study watersheds, with a higher proportion of dilution events in winter and fall months and – in general – a greater proportion of flushing events in Spring and Summer (Figure 2.5). The flushing responses were dominated by anticlockwise (i.e., FA) events, with a cluster of FC event responses occurring in late summer – early fall (August, September, and October) (Figure 2.5). The monthly proportion of events exhibiting no hysteresis was low (FN, DN, chN), but consistent throughout the year (Figure 2.5).

2.3.3 Kruskal-Wallis tests

Temporal and spatial variation in storm event responses were further explored with nonparametric Kruskal-Wallis tests and post-hoc pairwise comparisons. The combined, categorical FI/HI values were defined previously (e.g. FA, DA, FC, DC, etc.) and were tested for significant differences in the number of types in each category across seasons, months, and watersheds. Individual FI and HI numerical values were assessed for significant differences in the same way (Table A2.1).

The categorical FI/HI combination types were only significantly different between the seasons of Winter and Summer ($p=0.01$), highlighting the influence of seasonal climatic variation between wet and dry periods in the region. In addition, the combination of FI and HI was significantly different between watersheds 703 and 708 ($p=0.003$) (Table A2.1).

When assessing spatiotemporal variation in FI, we found that the flushing-dilution response was significantly different between Summer and Winter, and Summer and Fall ($p<0.001$). Specific pairs of months that exhibited significant differences in the FI reflect these seasonal trends, and include February-August, April-October, April-November, April-

December, June-November, June-December, August-October, August-November, August-December, and September-November ($p<0.001$). The only watersheds that were significantly different in their FI response were WS 819 and WS 1015 ($p=0.011$) (Table A1).

In contrast, the hysteresis response to storm events (HI) was not significantly different on a seasonal or monthly basis. This suggests that FI, rather than HI, is driving the observed temporal variation. However, significant spatial differences were found in HI between watershed 703 and 708, and between watershed 703 and 819 ($p<0.001$) (Table A1).

2.3.4 C-Q Plots

Slope coefficients of seasonally-demarcated C-Q plots show seasonal patterns that are similar across watersheds and that reinforce the event-based FI trends discussed above. Most of these responses are weak at the annual scale, or within the -0.1 to +0.1 threshold as demarcated in Bieroza and Heathwaite (2015) (Figures 2.7, 2.8) although the variation between hysteresis types clearly follows seasonal trends when assessed at the monthly scale (E.g. Figure 2.5). Across all watersheds, slope coefficients are primarily negative in winter, indicating a dominance of dilution event responses during the region's wet period, and are primarily positive in summer, indicating a predominance of flushing events during the region's dry period (Figure 2.7). The highest cross-watershed divergence in C-Q response occurs in Spring, with watershed 703 exhibiting an overall flushing response, and watershed 819 exhibiting an overall dilution response. The least divergence in seasonal C-Q response occurs in the Fall, with most watersheds exhibiting predominantly dilution event responses (Figure 2.7). Across watersheds, WS 1015 showed the least annual variation in C-Q response, with a slope that was near zero across all seasons. Annually, WS 703 and WS 708 exhibit slight to moderate net flushing, while WS 819 and WS 1015 exhibit slight to moderate net dilution. Although none of the annual C-Q plot slope coefficients are zero, the fact that many fall within the -0.1 to 0.1 threshold indicates an overriding chemostatic response on an annual to seasonal basis (Figure 2.7), as the seasonal flushing and dilution behaviours effectively cancel each other out.

2.3.5 Landscape Drivers of Hysteresis: Redundancy Analysis and CART

The per-event characteristics of our environmental parameters are demonstrated in visible boxplot ranges and outliers (Figure 2.8), as well as by descriptive statistics (Table 2.2). RDA 1 explained 26.3% and RDA 2 explained 8.0% of total variance in HI and FI, resulting in a total of 34.8% of variance explained by the response variables (Figure 2.9). RDA 1 was most strongly associated with the FI response, which was best explained by the climatic variables of API (soil moisture) and temperature. A positive (i.e., flushing) FI response was positively correlated with temperature, but negatively correlated with antecedent soil moisture. RDA 2 was most strongly associated with the HI response, which was best explained by the watershed-scale predictors of elevation and waterbody percent (ponds and wetlands). Here, a positive (i.e., clockwise) HI response is negatively correlated with watershed area and elevation, and positively correlated with % Waterbody and precipitation (Figure 2.9). However, these results may indicate differences between watersheds rather than true drivers due to our low watershed sample size (n=4).

Our CART analysis identified a series of environmental and catchment-scale drivers that served as determinants of the variation in event responses. Predictors that were identified as being significant in explaining the variation in combined, categorical FI and HI event responses included: 30-day antecedent soil moisture (30d API), waterbody cover (% ponds and wetlands)

(Wtb_prct), mean gap fraction (i.e. canopy cover; Mean_GapFrac), and mean temperature (Mean_Temp_QC_DegC) (Figure 2.10). The percentage of misclassified events in the terminal leaf nodes of our CART was moderate (40.5% - 56.8%).

At the highest level, the API enabled a split between a predominantly flushing (API 30d < 57mm) and dilution response (API 30d > 57mm) (Figure 2.10). Then, within the predominantly flushing responses (i.e. dry antecedent soil conditions), waterbody cover determined whether the response was predominantly anticlockwise (waterbody cover <= 7.5%) or clockwise (waterbody coverage > 7.5%). Within the predominantly dilution responses (i.e. antecedent wet soil conditions) a low gap fraction separated out DA events. This is likely a separation of WS 703 in the CART pathway analysis due to the high amount of DA events occurring in WS 703, and the abundant coverage of dense, wet and wetland forests within that watershed. Warm temperatures enabled a flushing response even under wet API 30d conditions in the remaining terminal nodes, yet when temperatures were lower, dilution dominated.

2.4 Discussion

2.4.1 Sensor Performance

The correlation between DOC_{sensor} concentrations and lab-derived DOC concentrations was marginally lower than values reported in other studies using similar fDOM sensors and correction methods ($R^2 = 0.74$) (Figure 2.2). High correlations between sensor and lab DOC have been found in various studies, including Saraceno et al. (2009) ($R^2 = 0.97$), Downing et al. (2012) ($R^2=0.93$), Wilson et al. (2013) ($R^2=0.85$), and Koenig et al. (2017) ($R^2=0.82$). A more moderate correlation was found between sensor and stream DOC concentrations in Schultz et al. (2018) ($R^2=0.78$). The highest correlation ($R^2=0.97$) was conducted in a study catchment in

Sacramento Valley, California, USA, with a mean annual precipitation between 450-860mm (Saraceno et al. 2009). In contrast, a study catchment in Massachusetts, USA had a MAP of 1100mm and a relatively lower correlation between sensor and stream DOC (R^2=0.85) (Wilson et al. 2013). The study catchments in Koenig et al. (2017) had a MAP of 1031-1260mm and a similar correlation between sensor and stream DOC (R^2=0.82), with a wide range in sensor accuracy depending on the catchment (0.38-0.95). Another fDOM sensor study was conducted in the humid, eastern climate of Connecticut, where catchments experienced relatively uniform precipitation throughout the year and more moderate correlation between sensor and stream DOC concentrations (R^2=0.78) (Schultz et al. 2018). Sites with lower mean annual precipitation (MAP) generally had a higher correlation between sensor-derived and actual DOC measurements.

Based on the known conditions that influence optical fDOM sensor accuracy (Downing et al., 2012), this reduction in sensor accuracy with increasing MAP could indicate a couple of mechanisms. High stream turbidity often accompanies high precipitation and could reduce sensor accuracy in these regions. High DOC concentrations often accompany high precipitation as well, which could increase fDOM sensor inaccuracy due to increased inner filter effects. Our study site has high precipitation but low turbidity, suggesting that inner filter effects are the dominant source of error in our fDOM sensor calculations. This indicates that we are reaching the upper DOC concentration limit for commercial fDOM sensors in this high-carbon region.

2.4.2 Trends in DOC concentration

The occurrence of precipitation primarily as rainfall throughout the winter months on Calvert and Hecate Islands (with the exception of some snowfall at elevation) increases the overall flux of DOC from soils to streams relative to other temperate ecoregions. The nearcontinual rainfall in the PCTR acts as a transport mechanism for soil DOC from organic-rich upland folisol soils throughout the year. More specifically, the largest increase in stream DOC concentrations occurs at the onset of Fall rains, which is followed by declining DOC concentrations throughout the rest of the wet season (Figure 2.3). This is likely due to the accumulation of DOC in riparian soils during the drier Summer months when a water transport vector is lacking. Once subsurface flowpaths initiate with increased precipitation, this reservoir of soil DOC is flushed to streams, as illustrated by $\text{DOC}_{\text{sensor}}$ concentrations across our study watersheds. DOC concentrations have also been found to be higher during storm events following dry conditions in a temperate bog (Tunaley et al. 2016). The cool summers exhibited by the coastal climate of the perhumid PCTR could dampen seasonal variation in NPP in comparison to humid, seasonal temperate rainforest regions with higher summer temperatures (DellaSalla et al. 2011), limiting relative soil DOC production in the drier summer months. However, this is most likely secondary to the influence of the dryness during the summer (Oliver et al. 2017), as soil DOC cannot be input to streams without a transport mechanism.

2.4.3 Seasonal variation in flushing via the FI and C-Q response

Two out of four seasons exhibited chemodynamism (flushing/dilution) in their stream DOC dynamics during storm events (Spring and Summer), while two seasons tended towards chemostasis (Fall and Winter) (Figure 2.7). Stream chemodynamism occurs when a solute concentration is sensitive and responds to changes in discharge, indicating a coupled hydro-biogeochemical cycle. The mechanism of chemodynamism lies in the lack of pre-existing “legacy” solute stores, so that stream solute concentrations during a storm event can increase or decrease (flush/dilute) in relation to soil wetness conditions (Bieroza and Heathwaite, 2018).

Theoretically, soils could become completely leached if the rate of hydrologic transport exceeded the rate of net primary production, and this is seen on a smaller scale in our study watersheds as the concentration of DOC dilutes slowly over multi-day and multi-week event series (Figure 2.3).

At the event scale, DOC responses demonstrated dilution (-FI) during storm events in the wetter period (Winter, Spring) and exhibited flushing (+FI) during storm events in the drier period (Summer) (Figure 2.7). Although these trends are muted when evaluated from a seasonal perspective relative to those at the monthly event scale (Figure 2.5); this is primarily due to the C-Q plots illustrating the broader aspect of these processes whereas assessment at the event scale demonstrates more detail due to a finer temporal resolution. Nevertheless, our C-Q plot findings maintain overall support for a model of subsurface hydrology and DOC transport being driven by antecedent moisture conditions. Greater wetness extends the contributing network and increases subsurface flowpath connectivity and mixing, which dilutes soil DOC during transport into the stream; less wetness decreases the contributing area and subsurface flowpath connectivity, limiting stream DOC inputs to adjacent stores that are flushed rapidly at the onset of a storm event. Similar seasonal effects were observed in the Connecticut River in southern New England, USA, where summer dry periods exhibited more flushing and winter wet periods exhibited more dilution (Schultz et al. 2018), as well as in a study conducted in agricultural streams, where dry conditions and small, frequent storms resulted in greater flushing behaviour than storms during wet conditions (Baker et al. 2019). The results of our RDA ordination support this model. Temperature is positively correlated with FI, indicating that stream DOC flushing is more likely to occur during warmer seasons. Conversely, the FI is negatively correlated with antecedent soil moisture, which indicates that stream DOC dilution is more likely to occur during seasons with higher pre-existing moisture levels, such as during the wetter Winter and Spring seasons. These correlations explain much of the seasonal variation in the FI throughout our study period and provide further support for a hydro-biogeochemical model of aquatic carbon cycling, specifically soil DOC mobilization and transport. These results are in alignment with the findings of our CART analysis as well.

Although the FI experiences seasonal chemodynamic flushing/dilution across all watersheds due to the accumulation of soil DOC during the summer and consequent flushing, averaging this variation creates a weaker, chemostatic signal at seasonal to annual scales when compared to the event scale (Figure 2.7). Regardless of streamflow, and thus the amount of water flowing through surrounding subsurface flowpaths, a chemostatic stream demonstrates relatively stable solute concentrations. This indicates an uncoupled hydro-biogeochemical (H-BGC) cycle at annual to seasonal scales, where the influence of subsurface hydrologic connectivity in solute transport is overridden by solute concentration.

This weaker signal at annual and seasonal relative to event timescales could also be indicative of a multi-annual "legacy" effect of high SOC stocks across our ecoregion, which contribute to the dampening of event-scale chemodynamic flushing/dilution responses (Bieroza and Heathwaite 2018). Indeed, recent research has demonstrated very high SOC stocks throughout our study region (McNicol et al. 2019). This legacy effect has also been exhibited in agricultural soils that have had multi-annual anthropogenic inputs of nitrogen- or phosphorous-based fertilizers, such that essentially unlimited solute availability nullifies the hydrochemical influence of broader catchment characteristics like soil, vegetation and topography (Basu et al. 2011). There is still uncertainty surrounding the effect of watershed size on stream solute behaviour and transport, as studies have found that large watersheds can exhibit both a dampening of hydrochemical effects due to mixing from diverse landscapes resulting in chemostasis (Creed et al. 2015), as well as a preservation of hydrochemical effects from disparate spatiotemporal hydrologic contributions and heterogeneous precipitation inputs (Zimmer et al. 2019). However, there is a decreased likelihood of this mechanism in our watersheds due to their small size. Thus, at annual to seasonal timescales, study watersheds in the PCTR experience chemostasis, or a predominantly uncoupled H-BGC cycle driven more strongly by local biogeochemistry than hydrologic variation. However, chemodynamism is evident in the monthly variation between flushing and dilution responses, which demonstrates a coupled H-BGC cycle driven by hydrologic conditions at the event timescale.

2.4.4 Seasonal variation in hysteresis via the HI response

In contrast to the event-scale variability in FI that we observed, the hysteresis direction of each storm event (HI) did not exhibit clear seasonal trends. The majority of storm events exhibited anticlockwise hysteresis regardless of season or month (Figure 2.4; Figure 2.5), further indicating that sources of terrestrially derived stream DOC in our study catchments are widely available, transport-limited, and mobilized from a larger subsurface contributing area (Lloyd et al. 2016; Rose et al. 2018; Coch et al. 2018). The high prevalence of multi-day precipitation events in our catchments increases the overall “ambient wetness” of the soil, which increases subsurface flowpath connectivity at the event onset and allows DOC to mobilize from a greater contributing area (Tunaley et al., 2016), leading to the prevalent characteristic anticlockwise delay of peak DOC following peak discharge. This delay has also been attributed to highly concentrated DOC-rich contributions from saturated wetlands or ponds pulsing into the stream after their storage is exceeded (Knorr et al. 2013; Fovet et al. 2018). Thus, the predominance of anticlockwise hysteresis on Calvert and Hecate Islands is likely due to delayed contributions as ambient soil wetness is flushed out and more concentrated DOC stores are input to streams from greater contributing areas, facilitated by wet soil conditions and thus greater hydrologic connectivity.

Although anticlockwise hysteresis dominated event responses across all seasons, there were a modest number of events exhibiting clockwise hysteresis throughout the study period (Figure 2.4; Table 2.3). Clockwise hysteresis has generally been attributed to the presence of limited solute sources that are adjacent or proximal to the stream, and thus require shorter transport time (Lloyd et al. 2016; Coch et al. 2018). DOC flushing is often associated with clockwise hysteresis due to the proximity of inferred DOC sources: when soils are dry, or when solute transport is limited by hydrologic connectivity, inputs are restricted to adjacent sources that are rapidly flushed into the stream. Following the FI trends, there were less FC (flushing, clockwise hysteresis) than DC (dilution, clockwise hysteresis) events, which was counter to our expectations. FC events were clustered in late Summer-early Fall, which was according to our expectations, whereas DC events showing a more uniform seasonal distribution. The clustering of FC events in the late Summer-early Fall is likely due to the flushing of DOC after OM has built up in the soils during the dry summer months. We can infer from the uniform seasonal distribution of DC events (clockwise, dilution) that it is common for DOC sources to be near streams in our study catchments, and that even proximal DOC sources can become diluted from the high antecedent moisture conditions and rainfall characteristic of this coastal, perhumid ecoregion. There are occurrences of DC events during the dry summer months however, indicating perhaps that storm events during the summer fully mobilize and dilute proximal DOC stores.

2.4.5 Environmental and Landscape Drivers: RDA and CART analyses

The findings of our RDA and CART models both reinforce the findings that – particularly for FI – seasonally-driven variations in moisture conditions drive variations in the hysteretic response. Other, recent work has explicitly tied subsurface connectivity to both trends in stream DOC concentrations and climatic drivers. For example, one recent study has demonstrated that maximum subsurface hydrologic connectivity is positively correlated with antecedent rainfall in addition to rainfall during the storm event (Zuecco et al. 2019). Field-verified models have garnered evidence for the dependence of subsurface hydrologic connectivity (i.e. solute transport) on a) storm event precipitation; b) storm event soil moisture; and c) antecedent soil moisture (Dick et al. 2015). In this context, our findings that dilution responses dominated during wet periods, while flushing was more likely during dry periods is coincident with the findings of previous work, and provide further support for considering DOC transport models in terms of combined hydro-biogeochemical cycling at sub-annual and sub-seasonal temporal scales.

In our RDA analyses, variation in FI was primarily explained by temperature and antecedent precipitation. This provides further support for the influence of antecedent wetness, and thus seasonality, in driving solute export dynamics. Antecedent moisture was also found to be a significant explanatory variable for the FI of nitrate export (Aguilera and Melack 2018), while root zone available water capacity has also been found to be a significant predictor of the FI for nitrate export (Musolff et al. 2015). The seasonality of FI in our catchments is also implied in the importance of temperature as a significant explanatory variable for the FI in this RDA. RDA2, which was more strongly associated with HI, explained much less variation in the dataset overall. The influence of predominantly landscape variables on the HI could indicate that DOC sources are driven more by watershed-scale spatial rather than environmental factors in this region. The low explanatory power of RDA2 could also indicate that DOC sources are primarily driven by spatial characteristics on smaller, sub-catchment scales. Waterbody cover (ponds and wetlands) and mean watershed elevation were negatively correlated with the HI. This could be due to the dominant landscape characteristics across our study catchments and how they affect DOC source distribution, where low lying, wetter, boggy areas accumulate more soil C relative to areas with higher relief.

The percentage of total events accurately classified by our CART analysis was moderate, although slightly greater than another study that used CART analysis to predict hysteresis trends (Aguilera and Melack, 2018). This suggests that collapsing spatial and temporal predictors into models of both solute transport and source dynamics may result in complexity that is not easily reducible to sequential pathways of individual predictor variables. As such, we use the results of our CART analysis with caution, and describe broad similarities between our CART model results and those found via the analyses described above. Similar to our RDA analysis, pre-existing API (soil moisture) from 30 days before the storm event onset was a key parameter for determining the hysteretic response.

Flushing events were predominantly explained by low antecedent moisture conditions and dilution events by high antecedent moisture conditions. Precipitation was the critical driver of whether flushing events were clockwise or anticlockwise (dry antecedent conditions). It is interesting to note that the CART pathway that is predictive of FC events combines low antecedent moisture conditions and high precipitation. This suggests a requirement for prior dry conditions in order to build-up concentrated soil OM stores, yet also the need for a moderate amount of wetness to mobilize soil DOC. In addition to supporting our RDA findings, these results highlight the importance of storm events during dry periods for DOC mobilization, transport, and export.

2.4.6 Synthesizing a subsurface solute transport model for wet coastal temperate rainforests

A classic model of solute transport dynamics that directly pairs hydrological and biogeochemical cycles is the attribution of a three-component system of hydrologic flowpath inputs to different combinations of hysteresis types (anticlockwise, clockwise, and no hysteresis) and solute concentration behaviours (flushing or dilution) (Evans and Davies, 1998; Long et al. 2017). The three hydrologic flowpaths included in this model are surface runoff event water (SE), soil groundwater (SO) or interflow, and groundwater (G) comprised of bank or baseflow and deep baseflow. The underlying assumption is that solute transport pathways can be identified based on the relative concentration of the solute in each contributing flowpath. The relative dominance of each hydrologic pathway thus provides a mechanism to explain both solute source and transport dynamics (HI and FI) during storm events.

This three-component model (Evans and Davies 1998) has been used as a reference in other studies of solute transport dynamics (Carroll et al. 2007; Long et al. 2017). Although the assumptions of this model may not be transferrable between systems (such as groundwater (G) having lower solute concentrations than surface runoff event water (SE) or soil groundwater (SO), or SE coming from more proximal sources than SO), its underlying principles can be used to frame our understanding of solute transport dynamics in the PCTR. By integrating this model of seasonal flowpath dominance with our understanding of seasonal solute transport dynamics through the HI and FI, we can develop a first-order, hysteresis-based hydro-biogeochemical model of subsurface DOC transport in wet, coastal temperate rainforests.

For our model, we have divided our full Aug 2015-2016 data period into four distinct hydrologic periods based on watershed hydrograph characteristics. We can consider each period as composed of a different proportion of SE, SO, and G based on the understanding of PCTR solute transport dynamics gained in this study. The four periods include: 1) Re-wetting (late August to mid-September); 2) Wet (mid-September to mid-March); 3) Drying (mid-March to mid-April); and 4) Dry (mid-April to late August) (Figure 2.3). The Re-wetting and Drying periods are short transitions between the longer periods of Wet and Dry and are meant to allow for consideration of the rapid shifts in flowpaths that occur during these time periods.

Solute availability fluctuates seasonally due to differences in rainfall and temperature. Without wet conditions to transport soil DOM as DOC during the drier summer period, soil C accumulates and rapidly flushes into streams once the rainy fall season begins. During the re-wetting stage rapid hydrologic and biogeochemical change occurs. SO flowpaths increase, but this increase also encounters the majority of the dry period's accumulated carbon, which enables rapid export. Once the re-wetting phase is complete, the accumulated dry summer high carbon stores have been exported and DOC concentrations decrease. As the wet period continues DOC concentrations further decrease, indicating soil DOC stores are being diluted due to prolonged high SO flowpath connectivity and thus transport. During the re-wetting period, the primary DOC source transitions from accumulated dry period SOM, to active SOM from ecosystem NPP. During the drying period, the DOC source transitions from the active transport of highly connected, terrestrially-derived DOC sources, to isolated soil DOC stores which accumulate due to drier conditions and a lack of transport. Due to the presence of relatively shallow granodioritic bedrock across our coastal watersheds, the influence of deeper groundwater flowpaths (>1m depth) in our site-specific model is assumed to be negligible. The SE flowpath is more likely to contribute terrestrial POC than DOC to streams, as surface runoff mobilizes larger, less decomposed organic material from the ground surface.

Based on these assumptions and our results, we propose that SO is the primary solute transport flowpath for DOC in wet coastal temperate rainforests with legacy soil organic carbon stores. Flowpath dominance can be understood in bedrock-underlain PCTR catchments as a seasonal alternation between SO flowpath networks of differing extent, connectivity, and density. During wet seasons there is an SO flowpath network of high extent, connectivity, and density (SO_H), and during dry seasons there is an SO flowpath network of low extent, connectivity, and density (SO_L). SO flowpaths change seasonally from highly connected, large, dense networks in wet periods to isolated, small, sparse networks in dry periods, and seasonal trends in solute export follow these hydrologic changes as well. The following relative flowpath dynamics for each period are as follows: 1) Re-wetting: $SO_L = SO_H$; 2) Wet: $SO_L < SO_H$; 3) Drying: $SO_L = SO_H$; 4) Dry: $SO_L > SO_H$. The following relative solute concentration dynamics for each period are as follows: 1) Re-wetting: $DOC_{SOH} = DOC_{SOL}$; 2) Wet: $DOC_{SOL} < DOC_{SOH}$; 3) Drying: $DOC_{SOL} = DOC_{SOH}$; 4) Dry: $DOC_{SOH} < DOC_{SOL}$. DOC concentrations will be highest in the re-wetting period as it immediately follows the dry period and the build-up of DOC; and will be lowest at the end of the wet period, as that is when dilution exerts the strongest influence on stream DOC response.

In summary, high stream DOC export is likely to occur in the PCTR during hydrologic periods after the accumulation of isolated soil carbon stores during the dry period, and when the SO flowpath network is highly connected, large and dense and hasn't fully diluted soil DOC (Re-wetting and late Wet periods, respectively). Soil DOC flux to streams is thus related to longer-term, seasonal soil moisture trends, where the influence of preceding conditions is key in determining subsurface solute sources and transport dynamics. It is necessary to consider DOC transport dynamics as being coupled with the seasonal hydrologic cycle, especially in the high-rainfall, perhumid region of the PCTR. Future work in this ecoregion should focus on validating or further developing the first-order subsurface solute transport model proposed in this study. This could be done by developing comprehensive carbon and water budgets for streams and their surrounding riparian areas, integrating techniques such isotope tracers and subsurface well networks in a mass-balance approach.

2.5 Conclusion

Anthropogenic climate change is already affecting global hydro-biogeochemical cycling, with many areas of the world either predicted to experience or already experiencing an increasing frequency and magnitude of storm events, warmer temperatures, and more frequent fluctuations between temperature extremes (IPCC 2015). The PCTR can serve as a global end-member when predicting stream metabolism and health in regions slated to experience a greater percentage of total annual precipitation as rainfall instead of snowfall, for example across much of western North America (Fosu et al. 2014; Szeto et al. 2015; Diffenbaugh et al. 2015), and in regions predicted to experience an increasing frequency and magnitude of storm events. However, the PCTR ecoregion is also expected to experience warmer temperatures and higher rainfall under climate change (Shanley et al. 2015). Locally, this could increase the already-high DOC yield of these small catchments, which can cause streams to become more heterotrophic, affecting in-stream ecology and metabolism. It could also increase the primary productivity and acidification rates of coastal marine ecosystems, and increase the atmospheric efflux of stream DOC mineralized as CO_2. Drier periods in these regions will likely begin to yield higher stream DOC exports, especially if summer storms increase in magnitude. More DOC will be flushed to streams in winter months with increasing temperatures. Our models suggest that temperature plays a secondary role to hydrologic connectivity in stream DOC export, so changes in rainfall will affect these wet, temperate ecoregions most heavily with temperature as a moderating effect. As such, it is likely that the relative significance of coastal temperate rainforest ecoregions in the global carbon cycle will increase as anthropogenic climate change progresses. Due to the coupling between hydrologic and biogeochemical cycles in solute transport dynamics, climatic changes will undoubtedly affect the timing and amounts of solute transport and mobilization, stream biogeochemistry, and terrestrial-marine-atmospheric biogeochemical cycling. It is critical we develop quantitative hydro-biogeochemical models of terrestrial-aquatic connections to manage, predict and prevent negative ecological and climatic effects from changes in aquatic carbon biogeochemistry, especially in organic-rich regions where terrestrial solute export is dominated by DOC.

2.6 Tables

Table 2.1: Landscape characteristics per study watershed on Calvert Island, British Columbia, including watershed area (km^2), total discharge yield (mm), flow-weighted mean stream DOC concentration (mg L^{-1}), mean organic topsoil depth (cm), and the proportion of surface area covered by lakes measured by Oliver et al. (2017); the dominant ecosystem class defined by Thompson et al. (2016); and the mean percent slope calculated in GIS mapping software from geospatial layers provided by the Hakai Institute.

Parameter	703	708	819	1015
Q-weighted mean [DOC] (mg L^{-1})[a]	9.00	10.90	19.30	12.90
Total Water yield (mm yr^{-1})[a]	3628	2158	1689	1791
Mean organic topsoil depth (cm)[a]	37.30 +/- 16.50	36.20 +/- 19.70	37.90 +/- 19.10	39.50 +/- 17.20
Dominant ecosystem class	fresh to very moist forest	wetter to wetland forest	wetter to wetland forest	wetter to wetland forest
Land Area (ha)	1255	721	480	303
Waterbody Cover (%)	1.9	7.5	0.3	9.1
Mean elevation (m)	325	93	247	132
Maximum elevation (m)	1012	384	465	432
Mean slope (%)	40.3	28.5	30.1	34.2
Mean Vector Ruggedness Metric (ha^{-1})	0.03	0.03	0.03	0.04
Main Channel Length (km)	7.3	2.5	1.6	1.6
Total Stream Network Length (km)	113.6	61.4	42.3	31.5
Drainage Density (km km^{-2}) (DD)	8.88	7.88	8.79	9.48
Max Flowpath (km)	10.45	6.96	4.87	4.03
Mean NDVI	0.70	0.66	0.68	0.69
Mean Gap Fraction (Canopy Cover)	0.52	0.63	0.58	0.53
Wetland Cover (%)	45.8	68.0	84.4	88.8

[a] Oliver et al., 2017
[b] Thompson et al., 2016

Table 2.2: Summary statistics of continuous predictor and response variables per storm event. Predictor variables include maximum discharge (max Q), maximum dissolved organic carbon (max DOC), stream temperature, precipitation, and the antecedent precipitation index (API) for 3 days, 7 days, and 30 days prior to the beginning of each storm event as a indicator of antecedent soil moisture. Response variables include the flushing index (FI) and the hysteresis index (HI).

	Max Q ($m^3 s^{-1}$)	Max DOC ($mg L^{-1}$)	Stream Temperature (°C)	Precipitation ($mm 5min^{-1}$)	API 3 days (mm)	API 7 days (mm)	API 30 days (mm)	FI	HI
Minimum	0.236	3.005	0	0	0	0	0	-1.000	-0.683
Maximum	29.74	25.54	20.5	183.2	143.5	221.6	360.6	0.965	0.672
Median	2.551	10.74	8.9	23.70	12.60	42.17	97.43	-0.310	-0.205
Mean	3.723	11.43	8.9	32.64	20.66	50.32	111.2	-0.235	-0.182
Mean SE	0.209	0.241	0.203	1.657	1.262	2.367	3.794	2.494	0.014
Mean CI (0.95)	0.411	0.474	0.399	3.259	2.481	4.655	7.462	4.906	0.029
Std Dev	3.916	4.528	3.80	30.64	23.67	44.41	71.19	46.80	0.274

Table 2.3: Matrix of storm event counts per event type. Events are classified based on threshold values of the flushing index (FI) and the hysteresis index (HI) and their associated combinations.

	Flushing (F)	Dilution (D)	Chemostasis (ch)	Total (HI)
Anticlockwise (A)	67	142	33	242
Clockwise (C)	12	52	2	66
No hysteresis (N)	4	39	2	45
Total (FI)	83	233	37	353

2.7 Figures

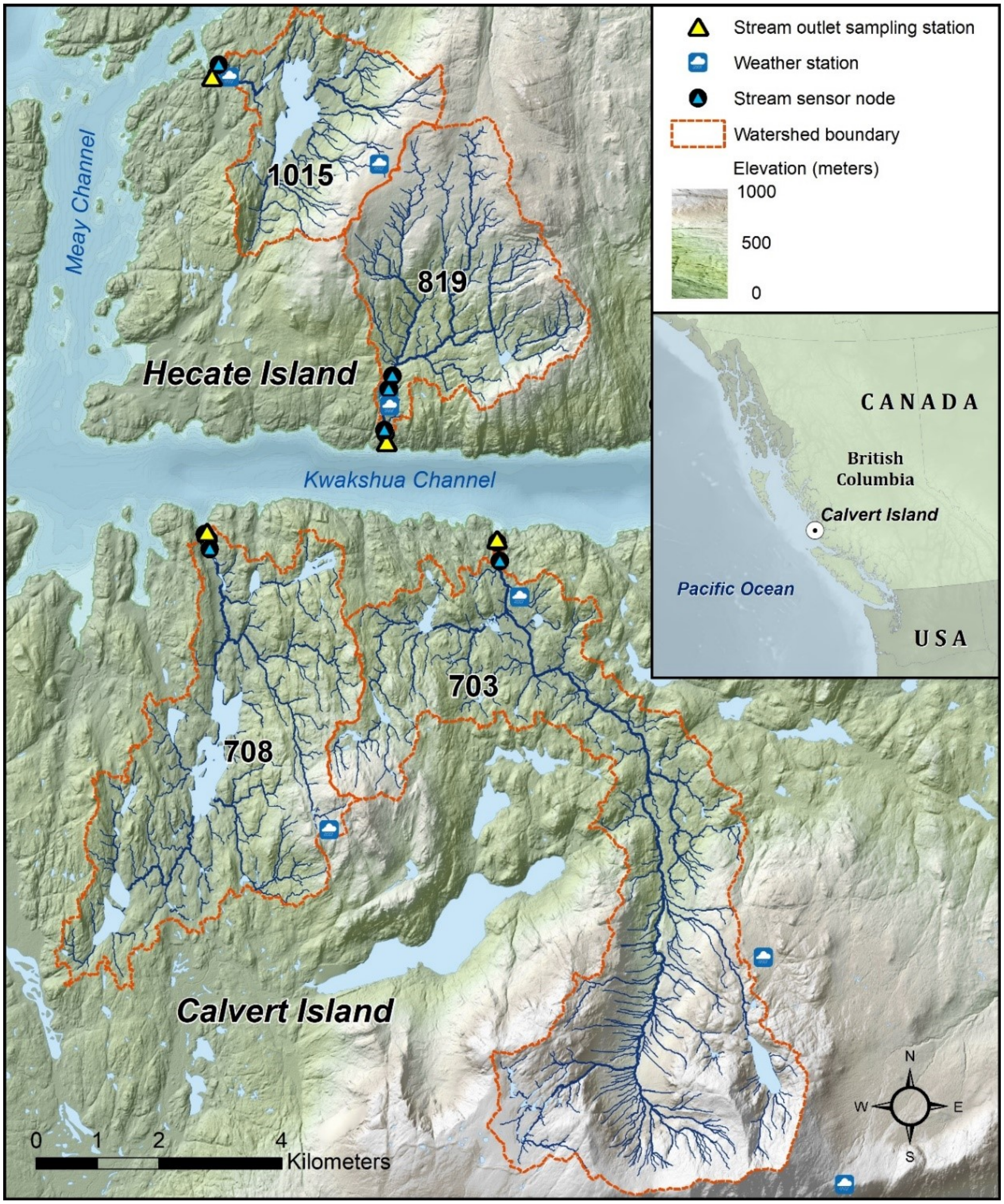

Figure 2.1: Map of the study watersheds, their stream networks, and installed sensors on Calvert and Hecate Islands, British Columbia, Canada. The inset indicates the location on the Pacific coast. The fDOM, turbidity, temperature, and water level sensors used in this study are located at the stream sensor nodes at the mainstem outlet of each study watershed. Precipitation gauges are located adjacent to each stream sensor node and at each weather station.

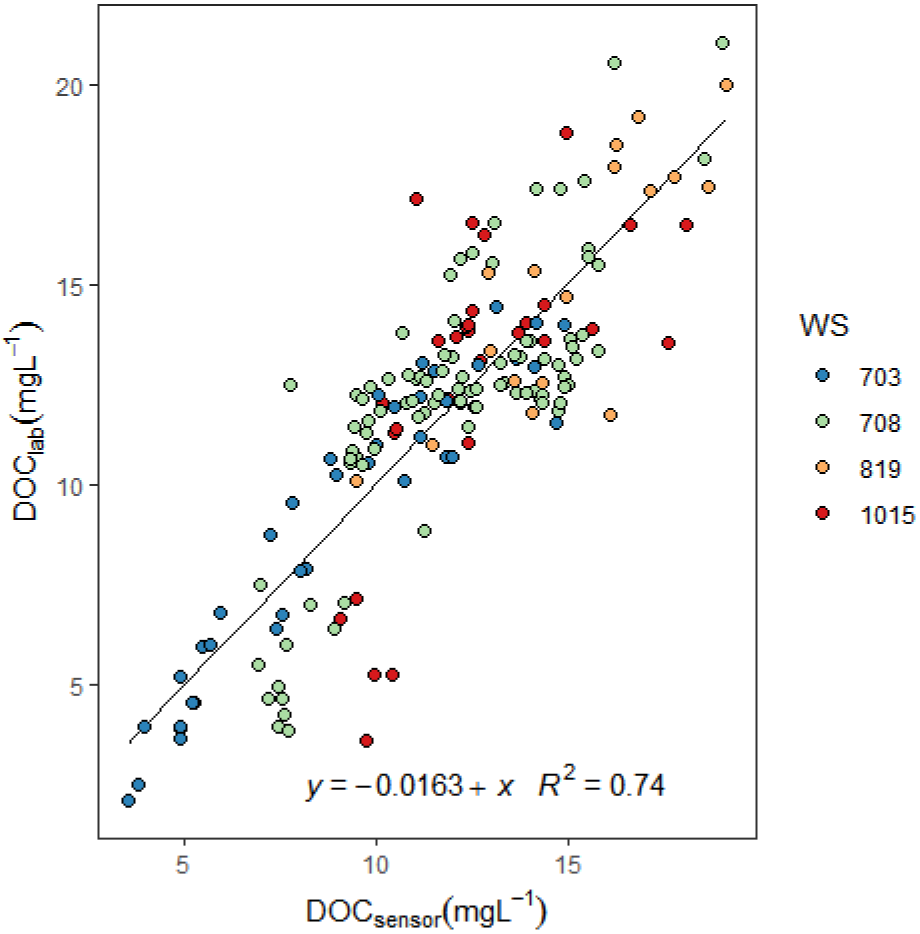

Figure 2.2: Final sensor DOC (DOC_{sensor}) corrected for the influence of temperature, turbidity, and inner-filter effects plotted against lab-processed stream DOC grab samples (DOC) for each of the four study watersheds during the 2015-2016 period.

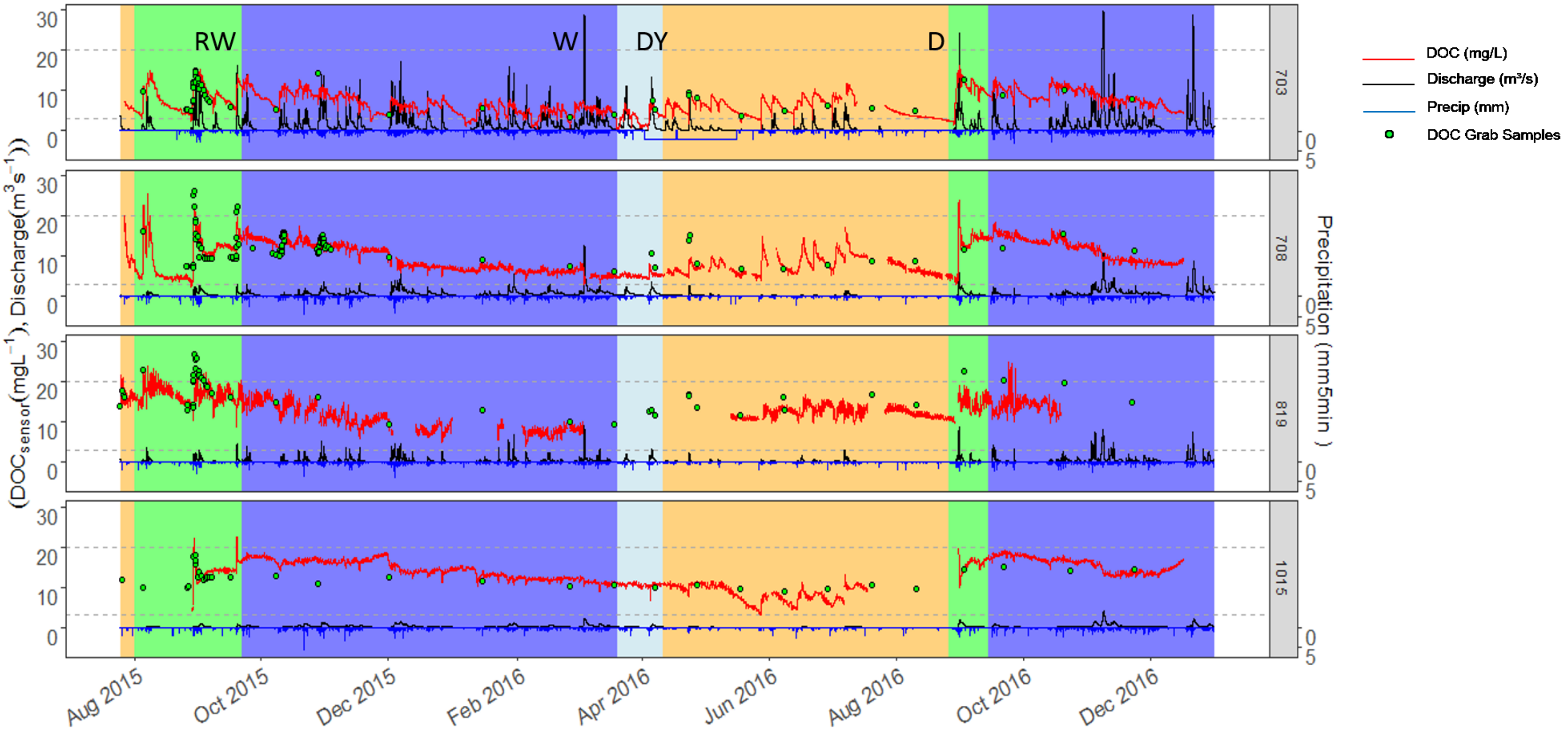

Figure 2.3: Time series of sensor DOC (DOC$_{sensor}$), stream discharge, precipitation, and lab-processed DOC grab samples for each study watershed during the 2015-2016 study period. Precipitation data was collected from rain gauges at proximal meteorological stations on Calvert Island, discharge was developed from a Lowess rating curve produced by the salt-dump dilution method and stream water level data (Korver et al., 2019) and sensor DOC was produced by fDOM sensors corrected for temperature, turbidity, and inner filter effects. The blue horizontal line in WS 703 indicates an absence of precipitation data. The labels for each coloured, shaded region of the timeseries indicate hydrological periods that coincide with our proposed conceptual model: 1) RW=Re-wetting; 2) W=Wet; 3) DY=Drying; and 4) D=Dry.

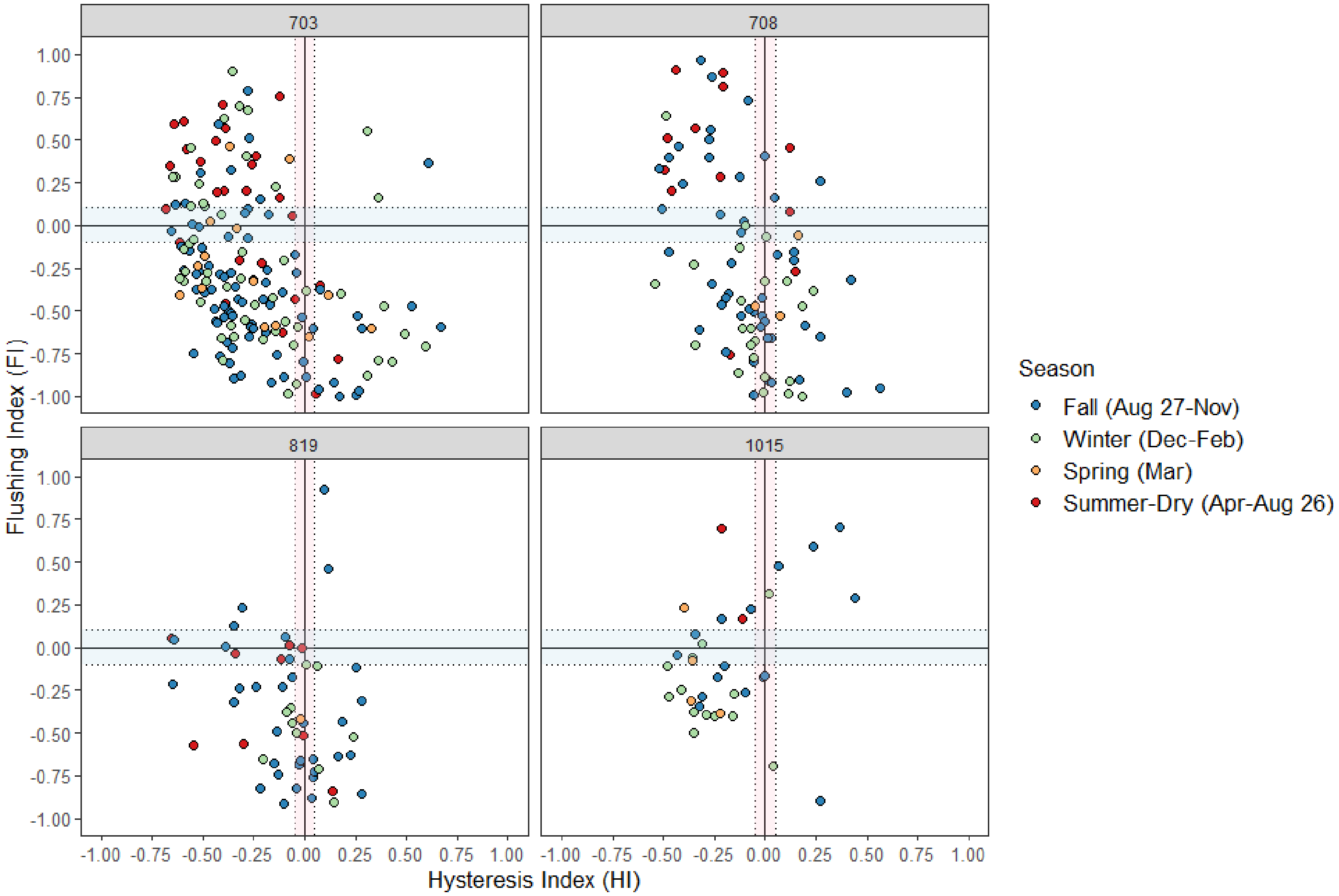

Figure 2.4: Event-scale distribution of FI and HI for each study watershed coloured by season. The four quadrats indicate the combination of FI and HI across various threshold values (see Figure 1 for details). The top-right quadrat (+FI, +HI) for each watershed is classified as FC (flushing, clockwise), the top-left quadrat (+FI, -HI) is FA (flushing, anticlockwise), the bottom-left quadrat (-FI, -HI) is DA (dilution, anticlockwise), and the bottom-right quadrat (-FI, +HI) is DC (dilution, clockwise). The red shaded regions indicate FN (flushing, no hysteresis), DN (dilution, no hysteresis); and the blue shaded regions indicate chA (chemostasis, anticlockwise); chC (chemostasis, clockwise), and the shaded square in the centre indicates chN (chemostasis, no hysteresis), where $-0.05 < HI < 0.05$ and/or $-0.1 < FI < 0.1$, respectively.

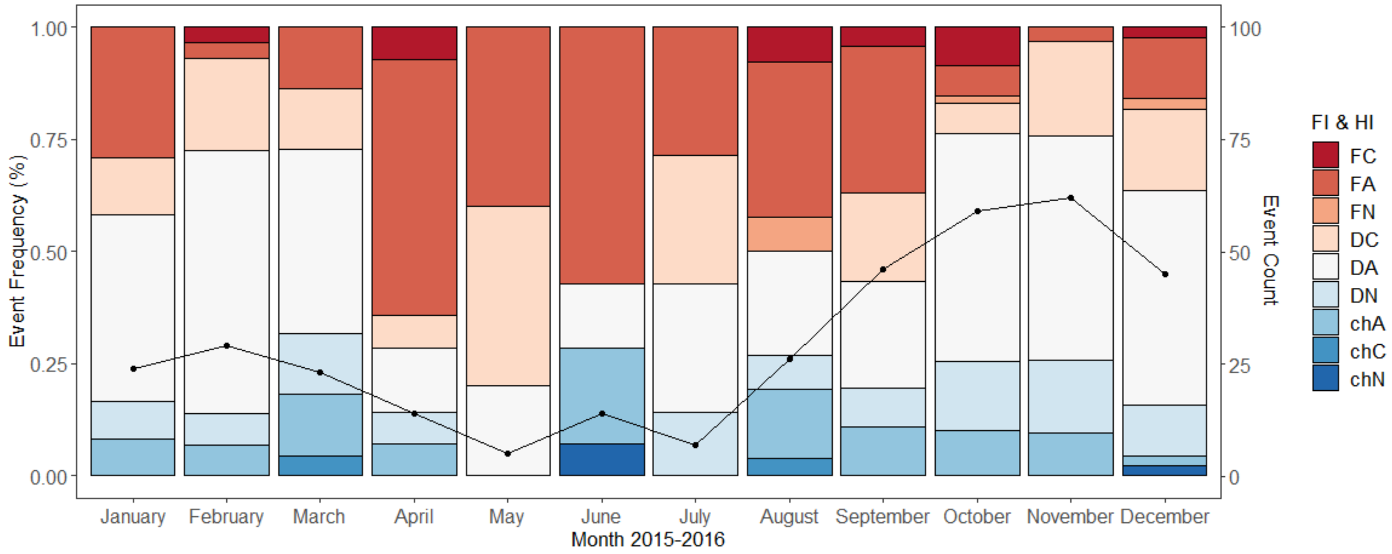

Figure 2.5: Monthly proportion of events that are classified as each quadrat-based event type (see Figure 2.4). The black points in each month indicate the monthly total event count. The categorical FI/HI combination types are as follows: FC=flushing, clockwise; FA=flushing, anticlockwise; FN=flushing, no hysteresis; DA=dilution, anticlockwise; DC=dilution, clockwise; DN=dilution, no hysteresis; chA=chemostasis, anticlockwise; chC=chemostasis, clockwise; and chN=chemostasis, no hysteresis.

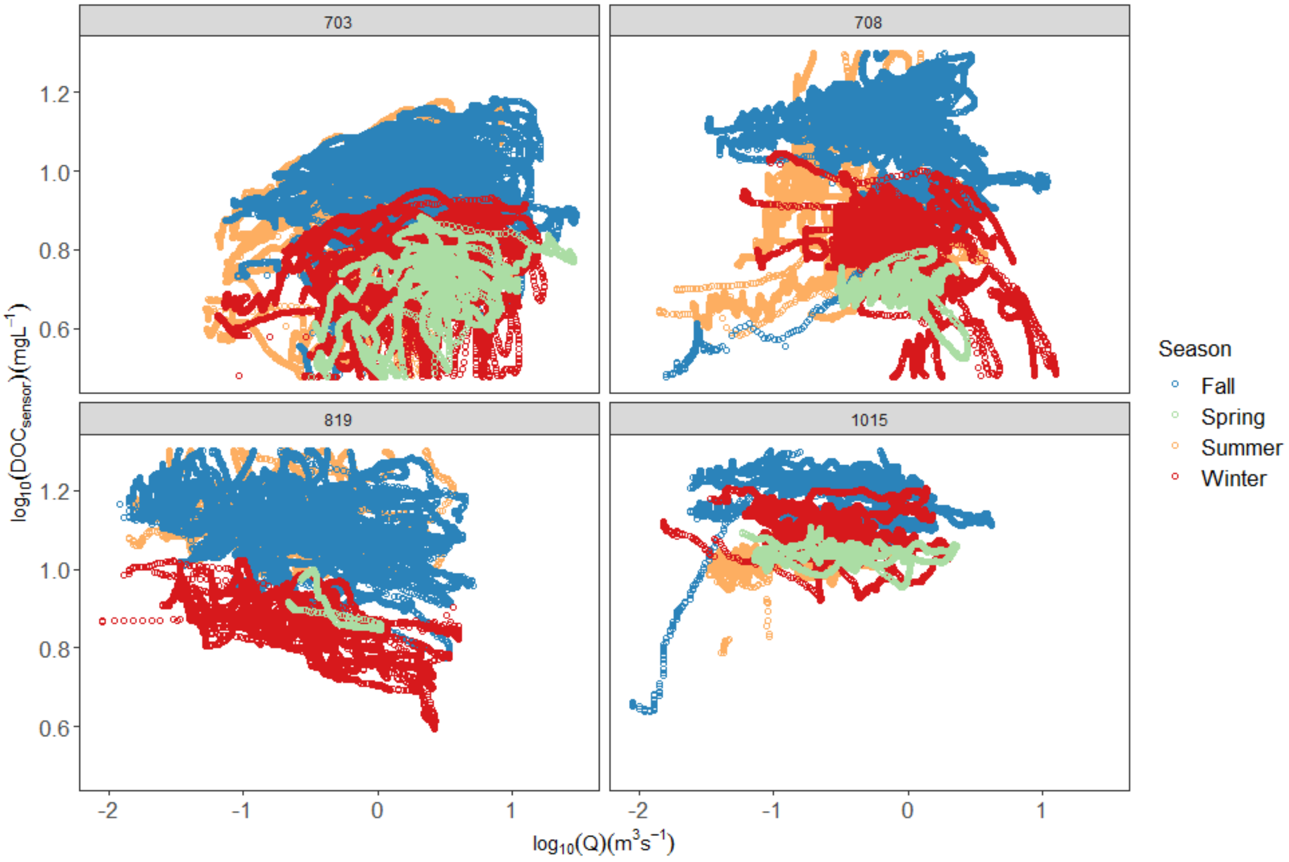

Figure 2.6: Solute concentration-discharge (C-Q) plots for each study watershed during the period 2015-2016, coloured by season between sensor DOC and discharge, with a threshold cut-off below 3 mgL^{-1} DOC.

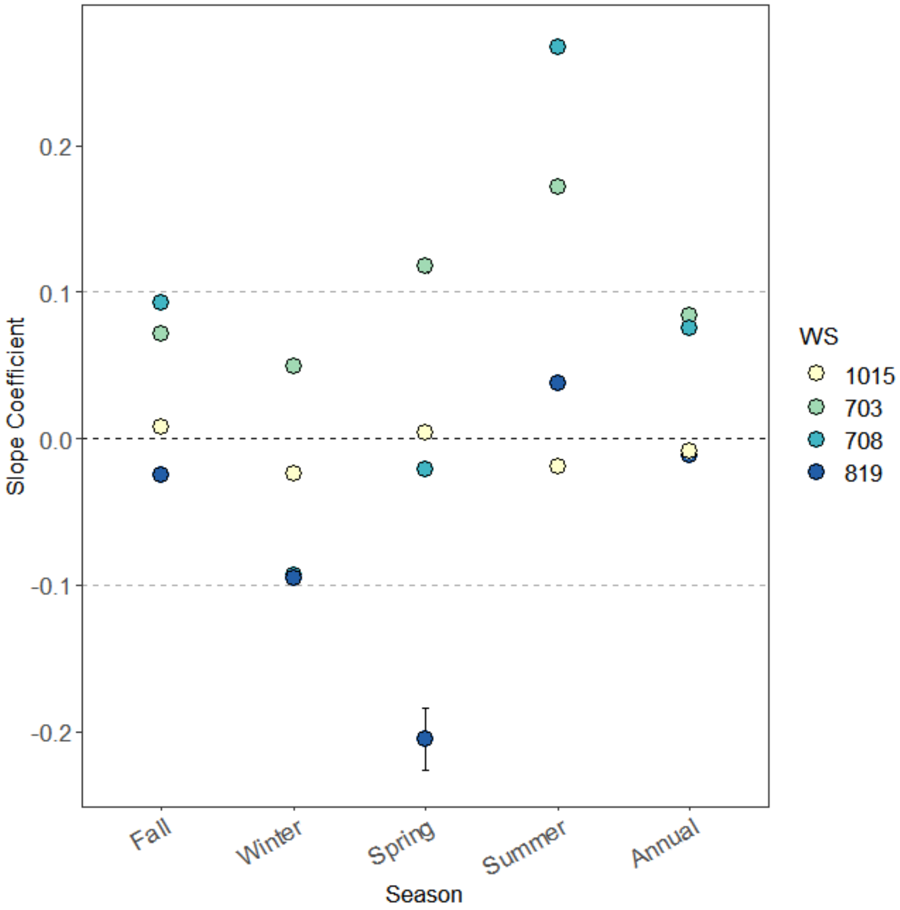

Figure 2.7: Annual and seasonal slope coefficients with 95% confidence intervals of the C-Q linear regression model between $\log_{10}$(DOC) and $\log_{10}$(discharge). Points above 0.1 indicate a positive C-Q slope and stream DOC flushing during storm events, and points below -0.1 indicate a negative C-Q slope and stream DOC dilution during storm events. Points within -0.1 to 0.1 represent a chemostatic stream response.

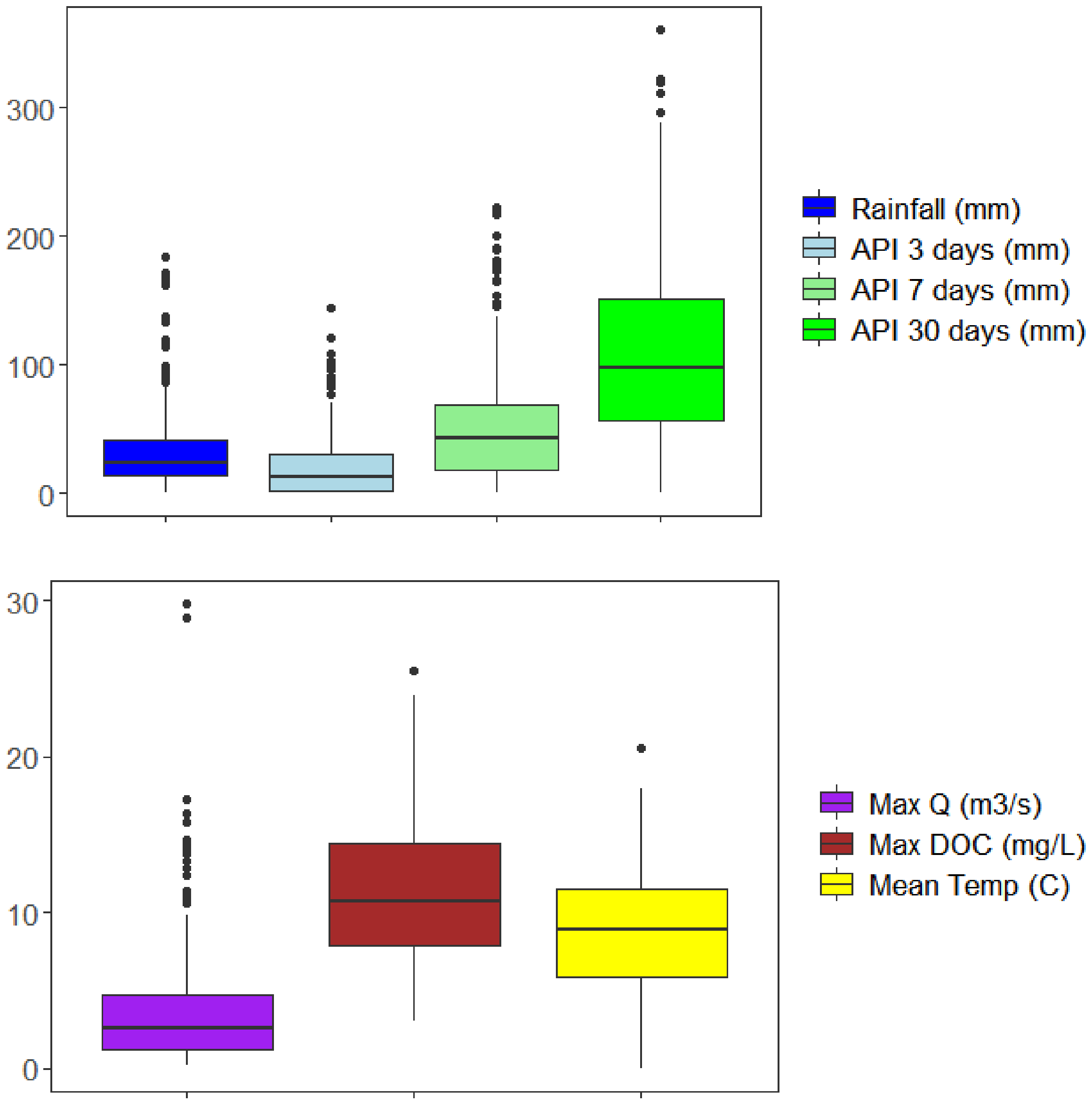

Figure 2.8: Boxplots indicating the median (horizontal line), range, and outliers of continuous predictor variables that were calculated for each storm event. Predictor variables include rainfall API 3d, API 7d, API 30d, maximum discharge, maximum sensor DOC, and mean temperature.

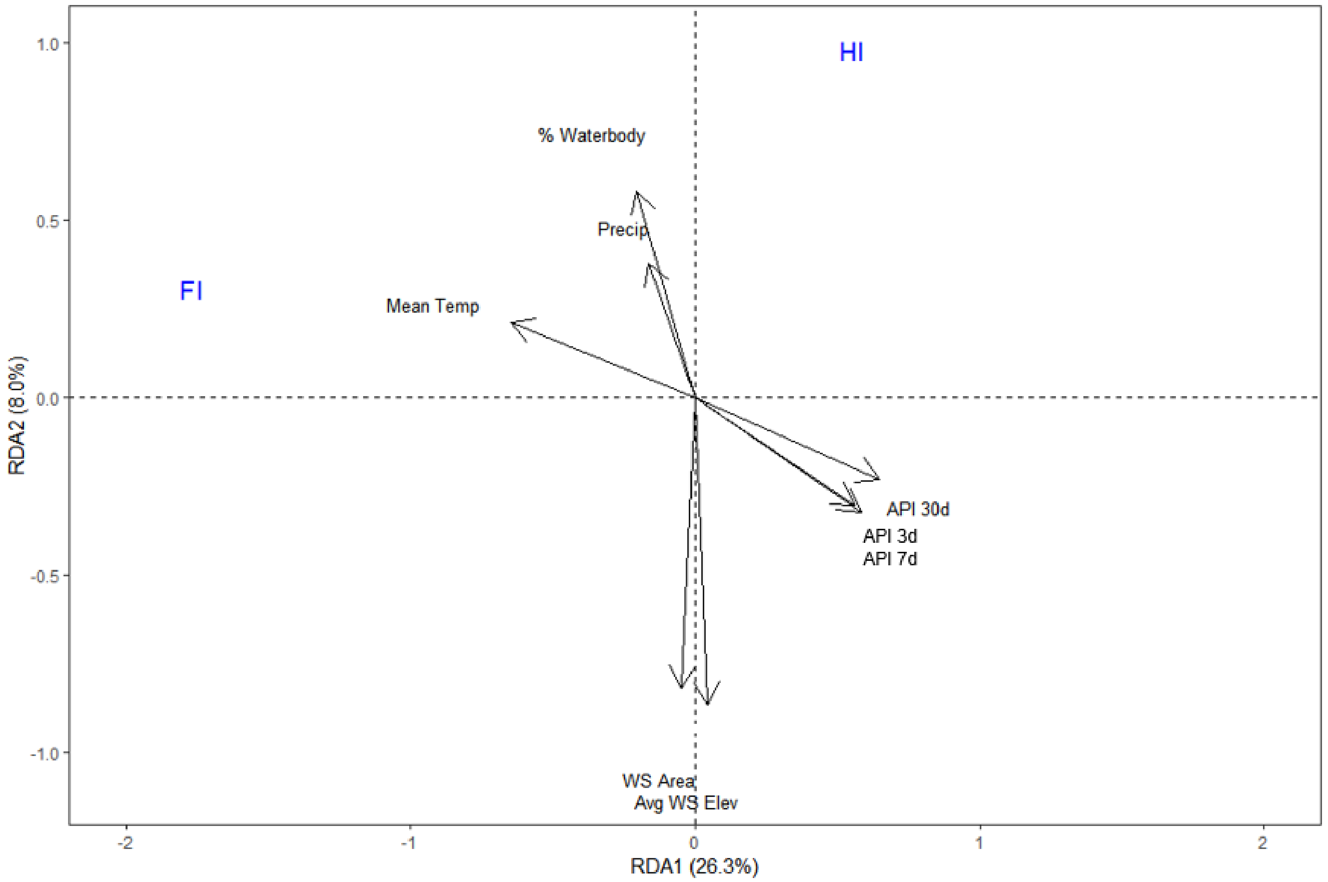

Figure 2.9: RDA of the constrained variance of response variables (FI and HI, in blue) explained by non-redundant predictor variables, including both climatic and watershed-scale spatial factors.

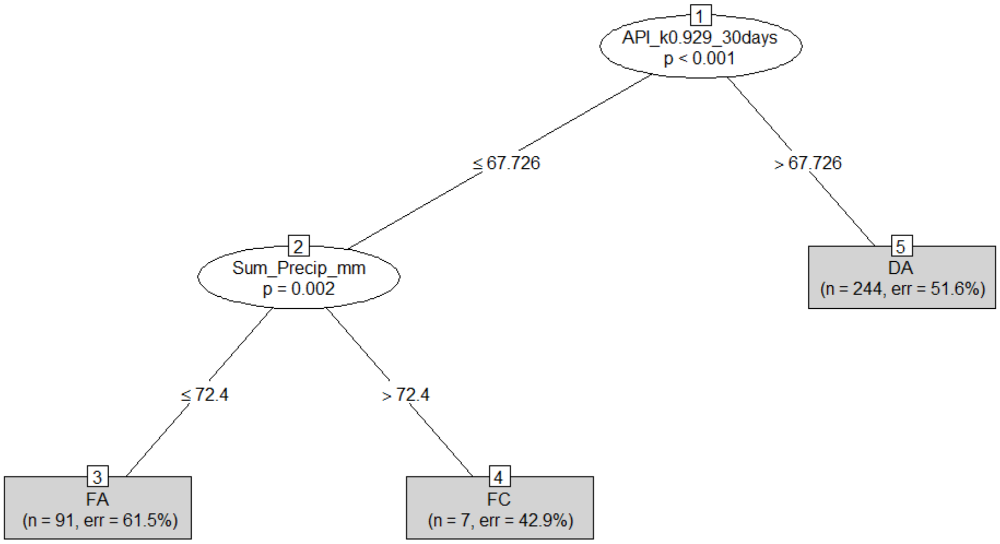

Figure 2.10: CART model output of significant predictors for the different categorical classes of quadrat-based event types from combinations of FI and HI. Inner nodes are indicated by circles, while final outer nodes are indicated by squares. Numbers in the lines between nodes indicate significant threshold values of predictor variables, which bin response variables into an event type category.

3.0 Sub-basin scale attributes drive dissolved stream CO_2 and CH_4 flux in northern pacific coastal temperate rainforest watersheds

3.1 Introduction

An important component of the global carbon cycle is the flux of carbon from inland freshwaters to the atmosphere, estimated at an annual rate of 3.9 Pg C yr^{-1} (Drake et al. 2017). These atmospheric freshwater emissions are a function of the lateral carbon fluxes from terrestrial to freshwater environments (Tank et al. 2017), and it has been estimated that the scale of these lateral fluxes are comparable to the residual terrestrial soil carbon sink (3.1 Pg C yr^{-1}; Le Quére et al. 2016). Sinks of stream C include autochthonous uptake by photosynthetic organisms (Jones and Mulholland, 1998), which has been estimated to decrease total freshwater C emissions by 0.3 Pg C yr^{-1} (Regnier et al. 2013). Freshwater C emission sources include root respiration and in-stream DOC mineralization via bacterial respiration, as well as in the adjacent riparian soil pore water, which both contribute to freshwater CO_2 (Mayorga et al., 2005; Waterloo et al., 2006; Berggren and del Giorgio, 2015).

In this project, our objective was to identify potential environmental controls on variability in two key greenhouse gases that are emitted from streams stream in the Pacific Coastal Temperate Rainforest (PCTR) ecoregion. We measured and assessed environmental drivers on CO_2 and CH_4 partial pressure and efflux to provide insight on watershed and sub-watershed carbon cycling, and to support future carbon budget calculations. Efflux here is defined as the outward flow of gases from the freshwater stream to the atmospheric environment. Partial pressure is a term that refers to the amount of pressure each gas in a gas mixture exerts against its container, which in this case is the stream's atmospheric boundary.

The PCTR ecoregion has been identified as a potential global "hotspot" for inland freshwater CO_2 evasion due to its wet climate and high amounts of organic material contained in catchment soils (Mayorga et al., 2010; Raymond et al. 2013). This classification as a potentially globally significant component of the carbon cycle highlights the need for further quantification of the controls on temporal variability in dissolved CO_2 flux. We conducted a spatial field survey across three hypermaritime watersheds on Hecate and Calvert Islands along central Pacific coast of British Columbia, Canada (Figure 3.1), to identify the primary sources of spatial and temporal variation in stream CO_2 and CH_4. We hypothesized that discharge (a proxy for turbulence) and flow type (a visual assessment of turbulence) would explain most variation in dissolved stream greenhouse gas (CO_2 and CH_4) partial pressure and efflux in our study watersheds. High turbulence increases the exposure of dissolved stream gases with the atmosphere, facilitating a more rapid efflux rate (Kling et al., 1998). As such, we hypothesized that sites with higher discharge and riffle flow types would positively related with CO_2 and CH_4 efflux, and negatively related with pCO_2 and pCH_4. Streams in this hypermaritime coastal environment also have very high concentrations of dissolved organic carbon (DOC) (Oliver et al., 2017). Although we expect stream DOC and CO_2 to be generally uncoupled in our study watersheds due to the influence of turbulence on gas evasion (Aufdenkampfe et al., 2011; Smits et al. 2017), the predominance of thick folisol soils and a carbon-rich landscape indicates that stream CO_2 partial pressure and efflux rates may be influenced by landscape characteristics to a certain extent (Section 2). Across watersheds, we expect stream CO_2 to have similar seasonal and hydrologic controls, such as stream temperature and rainfall.

It is increasingly critical to identify controls on atmospheric evasion of dissolved CO_2 and CH_4 as climatic and hydrologic patterns transform due to global climate change. Quantifying stream CO_2 and CH_4 efflux in this carbon-rich temperate rainforest ecoregion can support future climate modelling efforts and provide upscaled estimates of the cumulative impact of these ecoregions on global climate feedback systems.

3.2 Methods

3.2.1 Study Site

The North Pacific Coastal Temperate Rainforest (NPCTR) ecoregion (50°N - 58°N) spans from California to Alaska and is the largest contiguous stretch of coastal temperate rainforest in the world (Kellogg et al., 1995). This study took place in the NPCTR on the central coast of British Columbia, Canada, across three small watersheds on Calvert and Hecate Islands. Coastal temperate rainforest ecosystems are characterized by ocean proximity, coastal mountains, cool summer temperatures, and high precipitation across all seasons with either perhumid, or humid and seasonally dry climates (Weigand, 1990; Thornthwaite, 1948; Alaback, 1996). The NPCTR specifically has some of the highest biomass accumulations and rates of productivity of forest ecosystems in the world (Barbour and Billings, 2000), as well as extremely large stocks of soil organic carbon (SOC; McNicol et al. 2019). The study watersheds (WS) used for this research include WS 703, WS 708, and WS 819, as described in Chapter 2. Watershed 1015 was omitted from this sampling effort. Further details on the study region, as well as the distinct ecology, hydrology, and geology of our watersheds are presented in Table 2.2.

3.2.2 Data Collection

Field surveys were conducted in June 2017 and May 2018 to collect dissolved gas samples of CO_2 and CH_4 across our three study watersheds (Figure 3.1). Our gas collection method followed the headspace equilibration method outlined in Tank et al. (2009), whereby 60 mL of headspace was created in a sealed, 1L polyethylene bottle containing stream water, and the headspace was sampled following 3 minutes of equilibration between headspace and water sample via vigorous shaking. Duplicate samples were collected at each sampling location. In 2017, gas samples were collected in adjacent pool and riffle stream reaches along the stream mainstem to assess the effect of turbulence on dissolved gas concentration. We integrated a broader catchment approach into the sampling method in 2018 with the goal of capturing a wide selection of discharge and other model input parameters. Another objective was to sample at sub-basin outflows to pair sub-basin scale landscape data with gas concentrations, and where possible, to sample in the adjacent watershed mainstem for a direct comparison of gas levels and potential off-gassing. At the reach scale, sites were selected to maximize a range of streambed slopes, because of the importance of slope for regulating gas flux gradients (Raymond et al. 2012). Gas samples were processed for CO_2 and CH_4 concentrations with a Varian CP3800 gas chromatograph in the Biogeochemical Analytical Services Laboratory (BASL) at the University of Alberta, Edmonton.

At each site, measurements were taken for stream width, depth, velocity, bed substrate, flow type, discharge, slope, DOC concentration, and absorbance at $254cm^{-1}$ (A254). All water chemistry samples (DOC and A254) were filtered in the field (Millipore Millex-HP Hydrophilic PES 0.45 µm) and kept on ice, isolated from light sources, until their analysis at the BC Ministry of the Environment Technical Services Laboratory (Victoria, BC, Canada; DOC), or onsite (absorbance). DOC samples were preserved with 7.5M H_3PO_4 after being filtered into 60mL amber glass bottles. Stream width was measured with measuring tape, stream depth was calculated as the average of 10 measurements taken at equal intervals across the stream, stream velocity was taken from a single FlowTracker measurement at the site of gas sample collection, and stream substrate was visually assessed from within the stream. Substrates were defined on a scale from 0 to 6 based on grain size and texture, where 0=bedrock, 1=boulders, 2=cobbles, 3=pebbles, 4=gravel, 5=sand, 6=muck. A substrate was considered a "mix" if it was equal parts of two distinct materials. Flow type was assessed visually in the location of each gas sample as being a pool, riffle, or steady flow area. Discharge was assessed at a subset of sample sites due to time constraints, and was measured with a Sontek FlowTracker using the velocity-area relationship and five measurements taken at equal distances across the channel. Slope was determined for each sample site using two clinometers positioned at the same height above the streambed, at a distance of approximately 5m apart along the reach length. These parameters were sampled to accurately calculate the gas exchange velocity (k) which is a component of the gas efflux calculation (Raymond et. al 2012), and to explore environmental controls on spatial variation in stream pCO_2, pCH_4, and CO_2 and CH_4 efflux. Stream water temperature was measured using a YSI multimeter probe.

Measurements were also collected from the Hakai Institute's pre-existing telemetry watershed and meteorological monitoring network to assist in partial pressure and efflux calculations and in statistical modelling. Air temperature and sea level air pressure data were used from meteorological stations near the outlet of each study watershed, and stream temperature was collected from watershed sensor network monitoring sites near each outlet. Spatial data from Hakai's LiDAR watershed metric dataset (Gonzalez et al., 2015) was extracted from every sampled sub-basin in each study watershed to assess the influence of broader, sub-basin scale attributes on our response variables, the partial pressure and efflux of dissolved stream CO_2 and CH_4. These parameters include sub-basin perimeter, sub-basin area, waterbody percent cover, mean elevation, maximum elevation, mean slope, mean vector ruggedness matrix

(VRM), mainstem length (Lm), total stream network length (Lt), maximum flowpath length (MxFlwpth), and drainage density (DD). Sampled sub-basins were delineated in ArcGIS 10.4 (ESRI, 2013) by a visual assessment of hydrologic and topographic vector layers provided by the Hakai Institute. As such, the spatial data associated with each sub-basin is an approximation, yet it is suitable for a first-order estimate and exploratory analysis.

3.2.3 CO_2 and CH_4 Efflux Calculations

To calculate the rate of gas efflux from the streams to the atmosphere, the difference in concentration between water and air is multiplied by the gas transfer velocity (k), a coefficient with a unit of length per unit of time that accounts for the transfer speed between the two environments (Raymond et al. 2012; Equation 1):

$$F(g) = k * (C_{water} - C_{air}) \qquad (1)$$

Where F(g) is the air-water flux of a gas, C indicates concentration, and k is the gas transfer velocity of that gas from a stream to the atmosphere. The gas transfer velocity (k) is primarily dependent on the turbulent dissipation rate at the air-water interface. As such, previous efforts to determine accurate stream gas efflux measurements have focused on the reaeration coefficient (K or k_2), which is similar to k but not corrected for depth. To determine the gas transfer velocity (k) normalized to a Schmidt number of 600 (k_{600}) for CH_4, we employed an empirical, logarithmic relationship developed from 493 k_2 values derived from tracer-gas studies in 166 streams by the US Geological Survey (USGS). This relationship was verified using 127 k_2 values on 24 streams (Melching and Flores, 1999). Firstly, we calculated the oxygen reaeration coefficient (k_2) using Equation 10 from Melching and Flores (1999). Due to the fact that we conducted field sampling primarily during low flow conditions, and because our streams are small and experience pools and riffles, we chose the relationship for pool and riffle streams experiencing low flows (Q <

0.556 m^3 s^{-1}) (Melching and Flores 1999, Equation 10). This k_2 equation incorporates an empirical relationship developed through logarithmic regression modelling between physically related stream hydraulic characteristics: water-surface slope, discharge, velocity, depth, and width. After calculating k_2, we converted it to the oxygen gas transfer velocity (kO_2) following Raymond et al. 2012 and determined the Schmidt number for kO_2 (ScO_2) (Wanninkohf et al. 1992). This was then used to determine the Schmidt number for CH_4 (Raymond et al. 2012, Table 2), and from this the reaeration coefficient for CH_4 (kCH_4; Raymond et al. 2012, Equation 3).

We relied on predetermined relationships between k_{600} and stream morphology characteristics to calculate dissolved stream CO_2 efflux (Raymond et al. 2012; Table 2; Equation 1). The k models in Raymond et al. (2012) were developed with the same dataset as Melching and Flores (1999).

3.2.4 Statistical Methods and Analysis

In this study our aim was to assess the influence of various continuous and categorical environmental parameters on both the partial pressure and efflux of two dissolved stream greenhouse gases, CO_2 and CH_4. We assessed continuous predictors through a multivariate ordination analysis (RDA) and a univariate linear regression on ordination outputs. The effect of categorical predictor variables were assessed visually through the use of bar plots. We conducted our RDA and univariate regression analyses using all sample sites at the reach scale, as well as on the subset of sample sites that corresponded to specific, independent sub-basins within the larger watershed (sub-basin scale) to investigate the influence of local and broader watershed characteristics on dissolved stream CO_2 and CH_4 dynamics. Reach-scale continuous predictors included DOC concentration, absorbance at 254 cm^{-1} (A254; which is correlated to DOC), absolute slope, stream wetted width, stream depth, stream temperature and air temperature. Reach-scale categorical predictors included flow type (pool, riffle, and steady) and substrate. In addition to our reach-scale parameters, our sub-basin scale continuous predictors include sub-basin perimeter, area, waterbody percent cover, mean elevation, maximum elevation, mean slope, mean vector ruggedness matrix (VRM), mainstem length (Lm), total stream network length (Lt), maximum flowpath length (MxFlwpth), and drainage density (DD).

We calculated summary statistics of our continuous predictor and response variables with the package *pastecs* and the function *stat.desc* in R (R Core Team, 2013) at the reach (Table 3.1) and sub-basin (Table 3.2) scales. We calculated descriptive statistics of our categorical predictor variables with the *summary* function from base R (R Core Team, 2013) (Table 3.3). Summary statistics included the minimum, maximum, and mean. Normality was assessed with the Pearson's coefficient of skewness and a Shapiro-Wilks test. The skewness coefficient is an assessment of the symmetry of a data set's deviation around the mean. Significance of this statistic is assessed using the value of the skewness coefficient normalized to two standard errors following the z-distribution (Table 3.1; Table 3.2; Pskew 2SE), where an absolute value greater than 1 indicates significant non-normality. The Shapiro-Wilk's test is a more formal test for normality with the null hypothesis that the data is normally distributed. Any parameters that exhibit a p-value less than the alpha value (0.05) indicate a significant deviation from the normal distribution and thus skewness (Shapiro and Wilk, 1965; Table 3.1; Table 3.2; Shapiro-Wilks p value).

We input our continuous reach-scale and sub-basin scale predictor variables into distinct Redundancy Analyses (RDAs) using the function *rda* from the R package *vegan* (R Core Team, 2013). An RDA is a type of ordination for non-parametric multivariate regression models, which includes the response variables in the analysis and ordination plot output (unlike PCAs). We assessed the strength and direction of the univariate relationship between every RDA-selected predictor variable and our response variables using the function *lm* from base R (R Core Team, 2013). We visually assessed the influence of our categorical predictors on our response variables through the use of bar plots and the *ggplot* package in R (R Core Team, 2013).

3.3 Results

Field surveys resulted in a total of 74 dissolved stream CO_2 and CH_4 gas samples across our three study watersheds: WS 703 (n=23), WS 708 (n=21), and WS 819 (n=30). In addition to samples along the mainstem of each river, field samples were collected at the outlets of 21 sub-catchment basins of various sizes: eight basins in WS 703, six basins in WS 708, and seven basins in WS 819 (Figure 3.1). Summary statistics of these measurements are presented in Table 3.1. Across all sites, values for pCO_2 ranged from 325 – 4275 µatm, while values for pCH_4 ranged from 0.73 – 887 µatm (Figure 3.2, Table 3.1). The distributions of both pCO_2 and pCH_4 were positively skewed based on normalized skewness coefficients, indicating the presence of a small number of samples with relatively high values. The Shapiro-Wilks test output also demonstrates general data skewness across the majority of results, with p-values below 0.05 for all continuous predictor variables except DOC and A254.

3.3.1 RDA Output

Overall, our sub-basin scale RDA models performed better than our reach scale models, accounting for over half of the total variation in each dataset (Table 3.4, Figure 3.3, Figure 3.4). Our RDA model output for partial pressures of CO_2 and CH_4 at the reach scale (n=53) explained

16% of variance over the first two RDA axes (11% RDA1; 6% RDA2), indicating distinct environmental controls for each dissolved gas: pCO_2 was negatively related to A254 and DOC, and positively related to air temperature; whereas pCH_4 was negatively related to site slope and riffles, and positively related to stream temperature (Figure 3.3). This low explanatory power also indicates that some key variables may be missing from this initial model, such as turbulence or substrate, or some broader scale hydrologic and topographic parameters. RDA model performance at the sub-basin scale (n=10) (Figure 3.3) showed pCO_2 and pCH_4 to be driven by distinct landscape attributes, with pCO_2 negatively correlated with sub-basin area, and pCH_4 strongly positively related to maximum stream flowpath length, total stream network length, and stream mainstem length, and to a lesser extent positively correlated with mean slope and mean VRM. RDA1 explained 82% and RDA2 explained 14% of total variation in this second sub-basin scale RDA model, while total constrained variance explained was at 97% (Figure 3.3); which is substantially higher than the variation explained by our reach scale RDA output.

The total constrained variance explained by our RDA model for stream CO_2 and CH_4 efflux at the reach scale (n=22) (0.43) was far higher than the constrained variance explained in our reach scale pCO_2 and pCH_4 model (Table 3.4). RDA1 explained 39% and RDA2 explained 4% of the total variation (Figure 3.4). CO_2 efflux was negatively related to stream temperature and positively related to air temperature and riffles, while CH_4 efflux was negatively correlated with DOC, as well as moderately positively related to air temperature and steady flow (Figure 3.4). Although the sample sizes were reduced when including sub-basin scale data, the amount of constrained variance explained (i.e. related to our response variables) of our sub-basin scale RDA efflux model was the highest of any model (0.93; Table 3.4). RDA1 explained 78% of the variation in response variables and RDA2 explained 22% (Figure 3.4). CO_2 efflux at the sub-basin scale was primarily positively related to waterbody percent coverage, and negatively related to mean VRM and area. CH_4 efflux was dominated by the influence of hydrologic attributes at the sub-basin scale, such as maximum flowpath, total network length, and mainstem length, and sub-basin slope to a lesser extent (Figure 3.4).

3.3.2 Effect of Flow and Substrate (Categorical)

A visual assessment of our bar plot results suggest that pCO_2 does not vary consistently with flow type, while pCH_4 does (Figures 3.5, 3.6) (n=53). While pCO_2 did not visibly differ across flow types, pCH_4 was higher in pools than in steady or riffle flows. Relative to pCO_2 and pCH_4, flow type also appeared to have less influence on CO_2 and CH_4 efflux (Figure 3.7 and Figure 3.8, respectively) (n=23). Riffles accounted for the highest CO_2 efflux yet exhibited a high standard error. Steady flows accounted for slightly more CH_4 efflux than riffles.

Partial pressures of CO_2 were highest in sample sites with cobble and muck substrate, followed by gravel (Figure 3.7). A single sample site with a pebble-gravel substrate mix demonstrated relatively high levels of pCO_2. pCH_4 levels were highest at sites with muck substrate, followed by cobbles (Figure 3.8) (n=53). CO_2 efflux was also highest at sites with cobble substrate followed by sand, although the standard error for the cobble measurements was large (Figure 3.5) (n=23). CH_4 efflux was high in muck, sand, and cobbles (Figure 3.6) (n=23).

3.3.3 Univariate Linear Regression Models

We conducted univariate linear regression modelling on the output parameters of each RDA model to determine significant univariate relationships with partial pressures and efflux (Table 3.5). There were no significant predictors for pCO_2 or pCH_4 at the reach scale, while

pCO_2 at the sub-basin scale exhibited significant correlations with several attributes, including mainstem length, network length, and maximum flowpath (R^2 0.48-0.91; $p<0.05$) (Figure 3.9). pCH_4 was significantly correlated with the same variables at the sub-basin scale (R^2 0.77-0.91; $p<0.001$) (Figure 3.9).

Univariate regression results for CO_2 and CH_4 efflux were similar at the sub-basin scale, however at the reach scale they were more strongly explained by DOC than pCO_2 and pCH_4. CO_2 and CH_4 efflux were both significantly correlated with DOC at the reach scale (R^2=0.29, 0.19; $p<0.05$) (Figure 3.10). At the sub-basin scale, CO_2 efflux was significantly correlated with maximum flowpath length (R^2=0.37; $p<0.05$) (Figure 3.11). CH_4 efflux was significantly correlated with mainstem length, network length, and maximum flowpath length at the sub-basin scale (R^2 0.87-0.91; $p<0.0001$) (Figure 3.11). Across our study watersheds WS 703 had the highest partial pressure levels and efflux rates, whereas WS 708 and WS 819 were lower (Figures 3.9 - 3.11).

3.4 Discussion

The overall higher performance of our sub-basin scale models in comparison to the reach-scale model output suggests that broad-scale hydrologic and topographic attributes may have more of an influence on stream CO_2 and CH_4 than variables that are specific to the local reach. The influence of sub-basin and catchment-scale hydrologic and topographic attributes on stream CO_2 flux has been demonstrated elsewhere (Fellman et al. 2016; Bertuzzo et al. 2017). This could also indicate that a strong, reach-scale driver of pCO_2 and pCH_4, for example a quantitative measurement of turbulence, was missing from our RDA model parameters. Although substrate was excluded from our multivariate RDA ordinations, the visual correlation between both categorical predictors with pCO_2 and pCH_4 (Figures 3.5 - 3.8), as well as the inclusion of flow type in our RDA model output, implies that further work to capture these variables with continuous data may enhance the predictive power of stream C flux models in this ecoregion.

The negative relationship between pCO_2 and DOC at the reach scale is counter to the expectation that dissolved CO_2 levels have a generally positive relationship with DOC, where as DOC increases, in-stream mineralization also increases. This negative relationship could suggest that the influence of DOC on pCO_2 is negligible relative to other factors such as turbulence. It could also indicate that there may be a contraindicative dynamic between the type of carbon (highly aromatic; Oliver et al. 2017) being transported from soils to streams in this ecoregion and the metabolic ability of in-stream microbes that would otherwise mineralize the input carbon. Further work is needed to determine the influence of in-stream microbial DOC mineralization in these highly allochthonous streams, as well as the influence of terrestrially derived soil CO_2 from root respiration relative to in-stream DOC mineralization on total dissolved stream pCO_2.

Reach scale slope and stream temperature primarily explained stream pCH_4 levels, where reach slope was negatively and stream temperature positively related to pCH_4. Low slope can function as a proxy for the presence of wetland ecosystems in stream DOC models (D'Amore et al. 2015), as carbon accumulation in the form of peat is hindered on steep slopes (Smits et al. 2017). Stream temperatures can also be higher near wetlands due to the influx of shallow, warmed waters. These model outputs suggest that methane inputs to streams in our northern PCTR study catchments are driven by the proximity of wetland ecosystems. This is counter to the primary drivers of two of the world's largest tropical rivers, the Amazon and the Congo, where wetlands exerted strong control on pCO_2 yet not pCH_4 (Borges et al. 2015).

At the sub-basin scale, pCO_2 and pCH_4 were positively associated with several hydrologic attributes including the total stream network length, maximum flowpath length, waterbody % coverage, and mainstem length. This likely indicates stream CO_2 and CH_4 accumulation due to increasing subsurface soil inputs as one moves further downstream in the sub-basin. This is also in alignment with the River Continuum Concept, namely that stream reaches are dynamic in both space and time, and that they reflect the integrated processes of the upstream watershed (Vannote et al. 1980). Sub-basin area and the topographic Vector Ruggedness Metric (VRM) were also moderately positively related with pCH_4 in our RDA model output. The positive relation of sub-basin area with pCH_4 and the influence of the VRM could be indicative of the ubiquitous nature of wetlands in our ecoregion. Finally, after conducting linear regression between each individual RDA model response and predictor variable, we found that regression output reflected the RDAs and thus the evidence of the aforementioned potential drivers, as pCO_2 and pCH_4 were significantly correlated with sub-basin hydrologic attributes (mainstem length, R^2=0.48, 0.91; total network length, R^2=0.91, 0.82; maximum flowpath length, 0.54; 0.77, respectively) (Table 3.5).

Our reach scale RDA model output for CO_2 and CH_4 efflux was similar to the output for reach scale pCO_2 and pCH_4, however its overall performance doubled in terms of the cumulative constrained variance explained (Figure 3.3; Figure 3.4). DOC exhibited strong negative correlations with CH_4 efflux and CO_2 efflux, which reflects similar mechanisms with pCO_2 and pCH_4 described above. DOC was the only significant reach-scale predictor of CO_2 (R^2=0.29) and CH_4 efflux (R^2=0.19) determined by univariate linear regression between each individual model response variable and input parameter (Figure 3.10).

At the sub-basin scale, CH_4 efflux was more strongly correlated with the broader hydrologic attributes of maximum flowpath, maximum stream network length, and mainstem length than CO_2 efflux, indicating the possibility of divergent drivers between the emissions of both greenhouse gases. It also suggests a cumulative increase in CH_4 inflows throughout the watershed, again likely due to increasing wetland inputs. The positive relation of waterbody % cover with CO_2 efflux also supports the notion of cumulative C inflows due to wetlands as one moves further downstream in the watershed. The significant regression predictors of CO_2 efflux at the sub-basin scale was maximum flowpath (R^2=0.37), while for CH_4 efflux the significant predictors included mainstem length (R^2=0.91), network length (R^2=0.89), and maximum flowpath (R^2=0.87). These higher univariate coefficients of determination at the sub-basin scale relative to the reach scale suggest that broader hydrologic and topographic attributes may influence stream CO_2 and CH_4 flux more strongly than attributes at the site or stream reach level.

pCO_2 was highest in sites with pool conditions, and CO_2 efflux was highest at sites with riffle flow type. This supports our initial model of CO_2 efflux being driven by turbulence due to the more rapid exposure of in-stream dissolved gas to the atmosphere in turbulent, or riffle, areas. The high CO_2 emissions associated with cobble substrate could point to more groundwater influx through a coarse streambed medium, and the emissions associated with muck could be due to a proximity of wetlands and CO_2 produced via anaerobic methane oxidation. pCH_4 was also highest in pool stream sites, however CH_4 efflux was highest in sites with steady flows, rather than in riffles where CO_2 efflux was highest. This could point towards the influence of external methane sources in areas with slower flows, such as in bogs or other wetland ecosystems where stream water is forced through lower slopes, winding paths and shallower beds. Our substrate data also supports this, as pCH_4 is far higher in sites where the stream bed is partially decomposed muck, and thus where anaerobic methanogensis is more likely to take place (Figure 3.8).

3.5 Conclusion and Significance

This project provides evidence that supports the influence of broader, sub-basin scale hydrologic and topographic attributes on stream CO_2 and CH_4 fluxes. As stream networks are fundamentally connected both temporally and spatially, a dynamic approach that integrates both reach-scale and sub-basin scale data is necessary for moving forwards with research on the drivers of these dissolved stream greenhouse gases. Further investigation into the effect of flow and substrate type on stream CO_2 and CH_4 flux is warranted, as well as work on autochthonous CO_2 and CH_4 uptake/mineralization in perhumid, coastal PCTR watersheds. There is recent evidence that large stocks of SOC in the northern PCTR are driven primarily by precipitation and topographic characteristics, and that the high amounts of SOC are caused by and depend on high soil moisture (McNicol et al. 2019). Following this, northern coastal temperate rainforests should be considered as SOC storage hotspots on the scale of the global carbon cycle. However, shifting moisture regimes due to global anthropogenic climate change are predicted to affect the cycling of carbon in this ecoregion. Specifically, coastal perhumid regions of the PCTR are projected to experience increasing precipitation (DellaSalla et al. 2015). Based on the evidence presented by this research project, it is likely that increasing precipitation will increase the rate of transport of terrestrial SOC to streams in the form of DOC, CO_2 and CH_4, and as such will increase the emissions rate of greenhouse gases like CO_2 and CH_4 from streams to the atmosphere. Some evidence already indicates increasing soil DOC export with warming temperatures (D'Amore et al. 2015). Our results provide further support for evidence of a terrestrial-hydrologic carbon positive feedback loop in this ecoregion, which has implications for the global carbon cycle (Oliver et al. 2017). Left unaddressed and unincorporated into regional and global models, this feedback has the potential to increase greenhouse gas emissions to the atmosphere, exacerbating current anthropogenic climate warming and its effects.

Table 3.1: Summary statistics of continuous predictor, response, and site variables measured at each sample site or at proximal sensors. The skewness coefficient is an assessment of the symmetry of a data set's deviation around the mean. Significance of the skewness coefficient is assessed using the value of the skewness coefficient normalized to 2 standard errors following the z-distribution (Pskew 2SE), where an absolute value greater than 1 indicates significant non-normality. The Shapiro-Wilk's test also tests for skewness with a null hypothesis of normality. Any parameters that exhibit a p-value less than the alpha value (0.05) indicate a significant deviation from the normal distribution.

	Min	Max	Mean	Pskew 2SE	Shapiro-Wilks p value
DOC (mg L^{-1})	5.20	20.81	12.24	0.27	0.1717
A254 (cm^{-1})	0.00	0.87	0.53	-0.14	0.2859
Velocity (m s^{-1})	0.00	0.89	0.22	1.75	<0.001
Absolute slope (m/m)	0.00	0.25	0.04	3.80	<0.001
Stream width (m)	0.08	11.80	2.73	1.79	0.0002
Stream depth (m)	0.07	0.88	0.29	1.41	0.0040
Water T (˚C)	9.20	21.60	13.21	1.00	0.0020
Air T (˚C)	8.41	16.62	11.66	0.55	0.0088
Atm CO_2 (ppm)	438.63	481.60	463.48	-0.85	<0.001
Atm CH_4 (ppm)	1.46	2.79	1.73	2.91	<0.001
pCO_2 (µatm)	325.40	4275.30	950.35	4.99	<0.001
pCH_4 (µatm)	0.73	887.17	59.81	8.41	<0.001
CO_2 flux (mg m^{-2} s^{-1})	0.78	4540.03	0.59	3.01	<0.001
CH_4 flux (mg m^{-2} s^{-1})	-0.02	2.10	495.14	0.28	<0.001

Table 3.2 Summary statistics of sub-basin basin scale predictor variables. Sub-catchment basins and accompanying spatial datasets were delineated in ArcGIS 10.4 (ESRI, 2013) from the Hakai Institute's LiDAR Watershed dataset (Gonzalez et al. 2015).

	n	min	max	mean	Pskew 2SE	Shapiro-Wilks p value
Area (ha)	21	4878.38	2445288	508102.20	1.478	<0.001
Waterbody coverage (%)	21	0.17	7.51	2.18	1.069	0.016
Mean elevation (m)	21	69.00	325.39	211.96	-0.195	0.229
Max elevation (m)	21	196.92	1012.37	572.80	0.566	0.012
Mean slope (%)	21	28.05	40.85	34.32	0.111	0.040
Mean VRM (ha^{-1})	21	0.02	0.04	0.03	0.701	0.116
Mainstem length (km)	21	0.91	7.31	3.43	0.591	0.002
Total network length (km)	21	21.07	113.59	59.78	0.481	0.005
Maximum flowpath (km)	21	2.80	10.45	6.27	0.407	0.007

Table 3.3: Categorical predictor variables, their class IDs and definitions, and the total number of freshwater gas field survey sites per class.

Categorical Predictor Variable (2017-2018)	Class ID	Class	Total sites per class
Flow Type	P	pool	18
	S	steady	33
	R	riffle	43
Substrate	0	bedrock	4
	1	boulder	10
	2	cobble	12
	3	pebble	0
	4	gravel	11
	5	sand	4
	6	muck	3
	0-1 mix	bedrock-cobble	1
	1-2 mix	boulder-cobble	1
	1-4 mix	boulder-gravel	1
	2-4 mix	cobble-gravel	1
	3-4 mix	pebble-gravel	1
	4-5 mix	gravel-sand	2
	4-6 mix	gravel-muck	1

Table 3.4: RDA multivariate model parameters and outputs. Predictor variables are comprised of reach scale sample site and proximal sensor data, and sub-basin scale spatial data pulled from regional LiDAR layers in ArcGIS. Values are rounded to the second decimal place (0.01).

Response Variables	Predictor Scale	Predictor Variables	Prop. Constrained Variance Explained	Prop. Unconstrained Variance Explained	Prop. Total Variance Explained RDA1	Prop. Total Variance Explained RDA2	Significant Predictors (ANOVA) ($p < 0.05$)	n	Total Adj. R^2
pCO_2 and pCH_4	reach	slope, DOC, A254, stream temp, air temp	0.16	0.83	0.11	0.06	none	53	0.04
pCO_2 and pCH_4	sub-basin	area, waterbody % cover, mainstem length, network length, max flowpath, mean slope, mean VRM	0.97	0.03	0.82	0.14	mainstem length	10	0.86
CO_2 efflux and CH_4 efflux	reach	slope, DOC, A254, stream temp, air temp	0.43	0.57	0.39	0.04	DOC	22	0.20
CO_2 efflux and CH_4 efflux	sub-basin	area, waterbody % cover, mainstem length, network length, max flowpath, mean slope, mean VRM	0.99	0.00	0.78	0.22	mainstem length, waterbody cover (%)	10	0.99

Table 3.5: Univariate linear regression models parameters and significant outputs ($p<0.05$). Predictor variables are comprised of reach scale sample site and proximal sensor data, and sub-basin scale spatial data pulled from regional LiDAR layers in ArcGIS.

Response Variable	Predictor Scale	Significant Predictor(s)	R^2	p	n
pCO_2	reach	none	none	none	53
pCO_2	sub-basin	mainstem length network length max flowpath	0.48 0.91 0.54	0.0152 1.04×10^{-5} 0.0096	10
pCH_4	reach	none	none	none	53
pCH_4	sub-basin	mainstem length network length max flowpath	0.91 0.82 0.77	1.04×10^{-5} 0.0002 0.0005	10
CO_2 efflux	reach	DOC air temperature	0.29 0.29	0.006 0.006	23
CO_2 efflux	sub-basin	max flowpath	0.37	0.0362	10
CH_4 efflux	reach	DOC	0.19	0.022	23
CH_4 efflux	sub-basin	mainstem length, network length, max flowpath,	0.91 0.89 0.87	1.04×10^{-5} 2.91×10^{-5} 4.62×10^{-5}	10

3.7 Figures

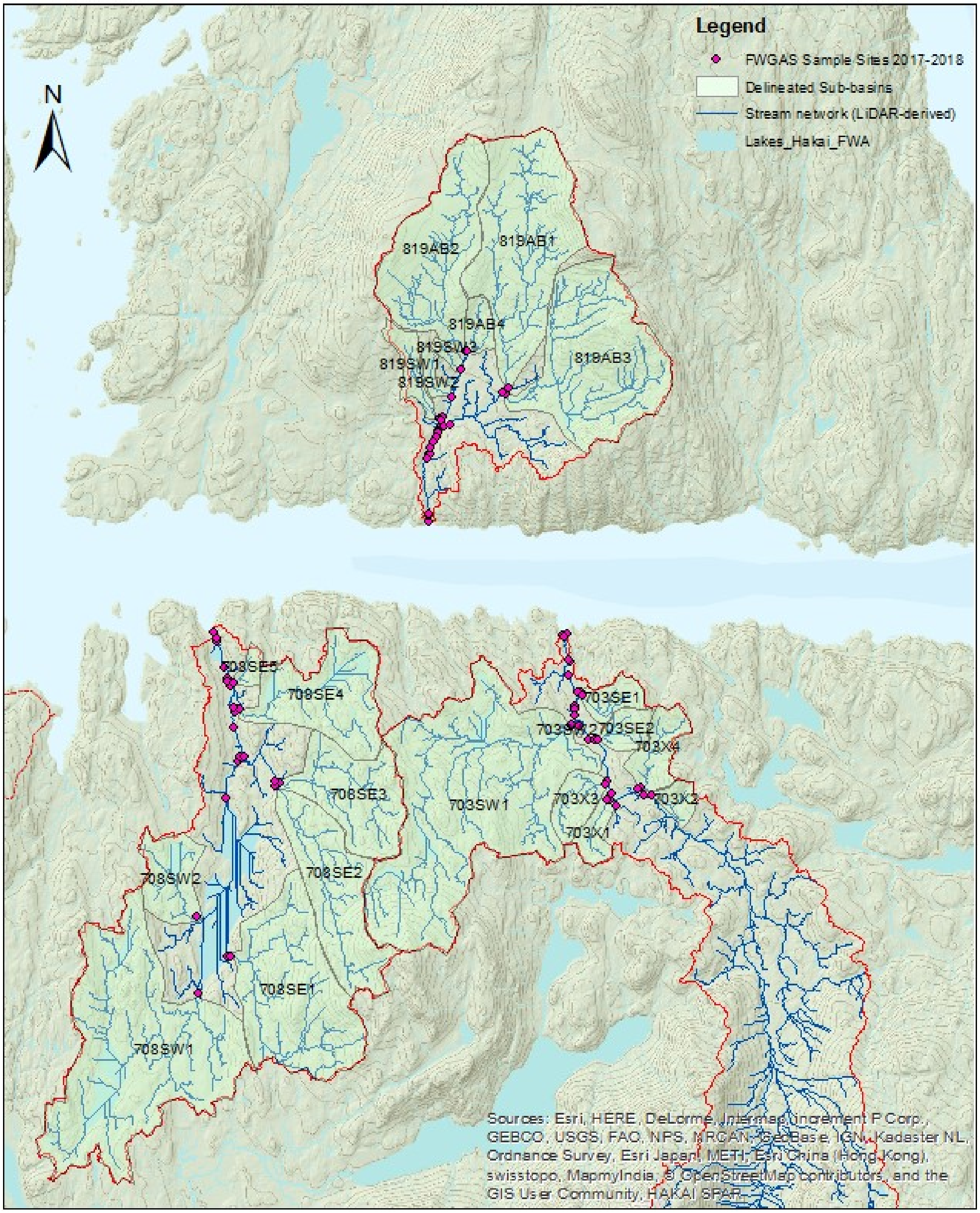

Figure 3.1: Map of our study watersheds (WS 819, WS 703, WS 708) and delineated sub-basins on Hecate and Calvert Islands, British Columbia, Canada.

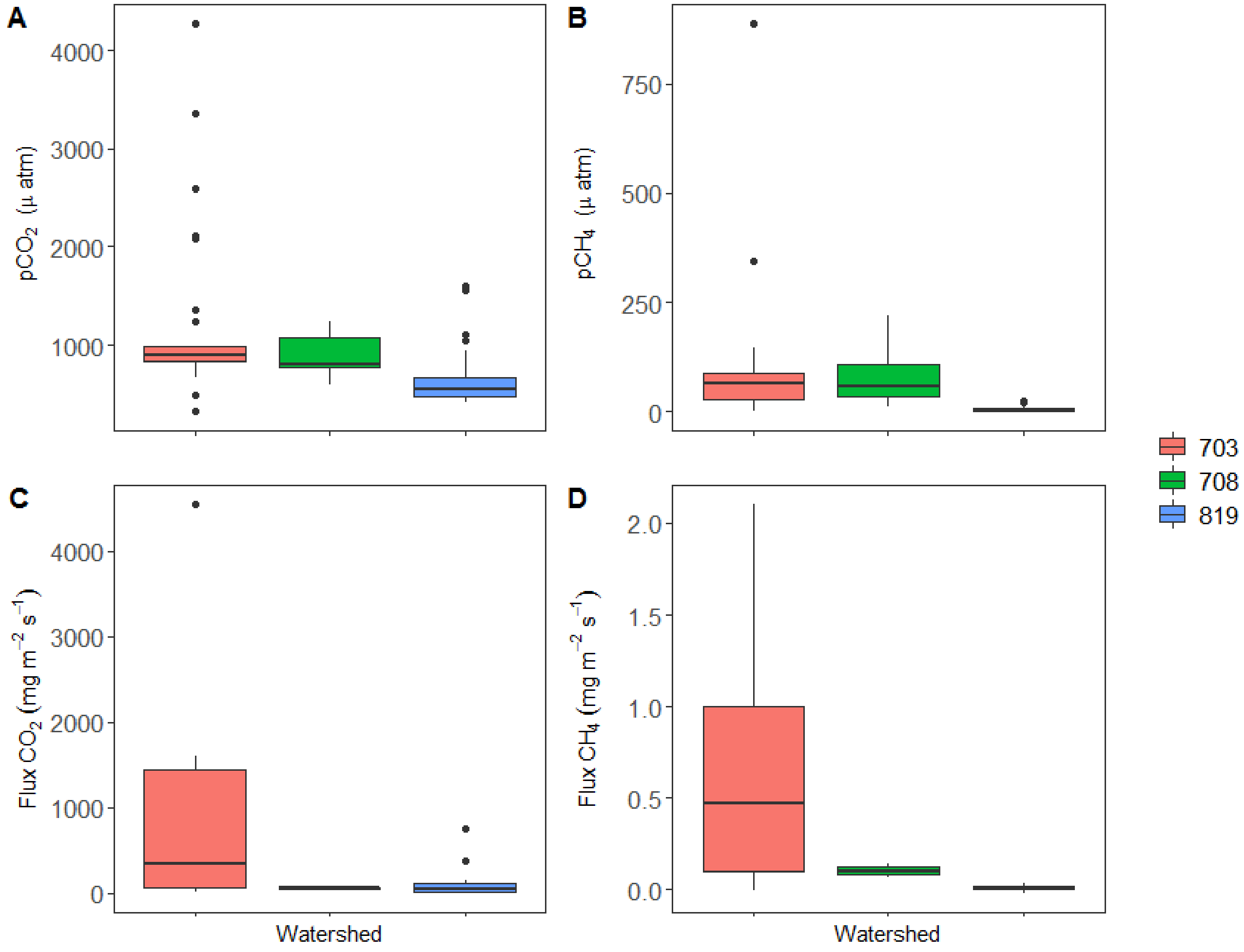

Figure 3.2: The range, median, and outliers of measured pCO_2, pCH_4, CO_2 efflux, and CH_4 efflux on Hecate and Calvert Islands in the coastal temperate rainforest of British Columbia, Canada.

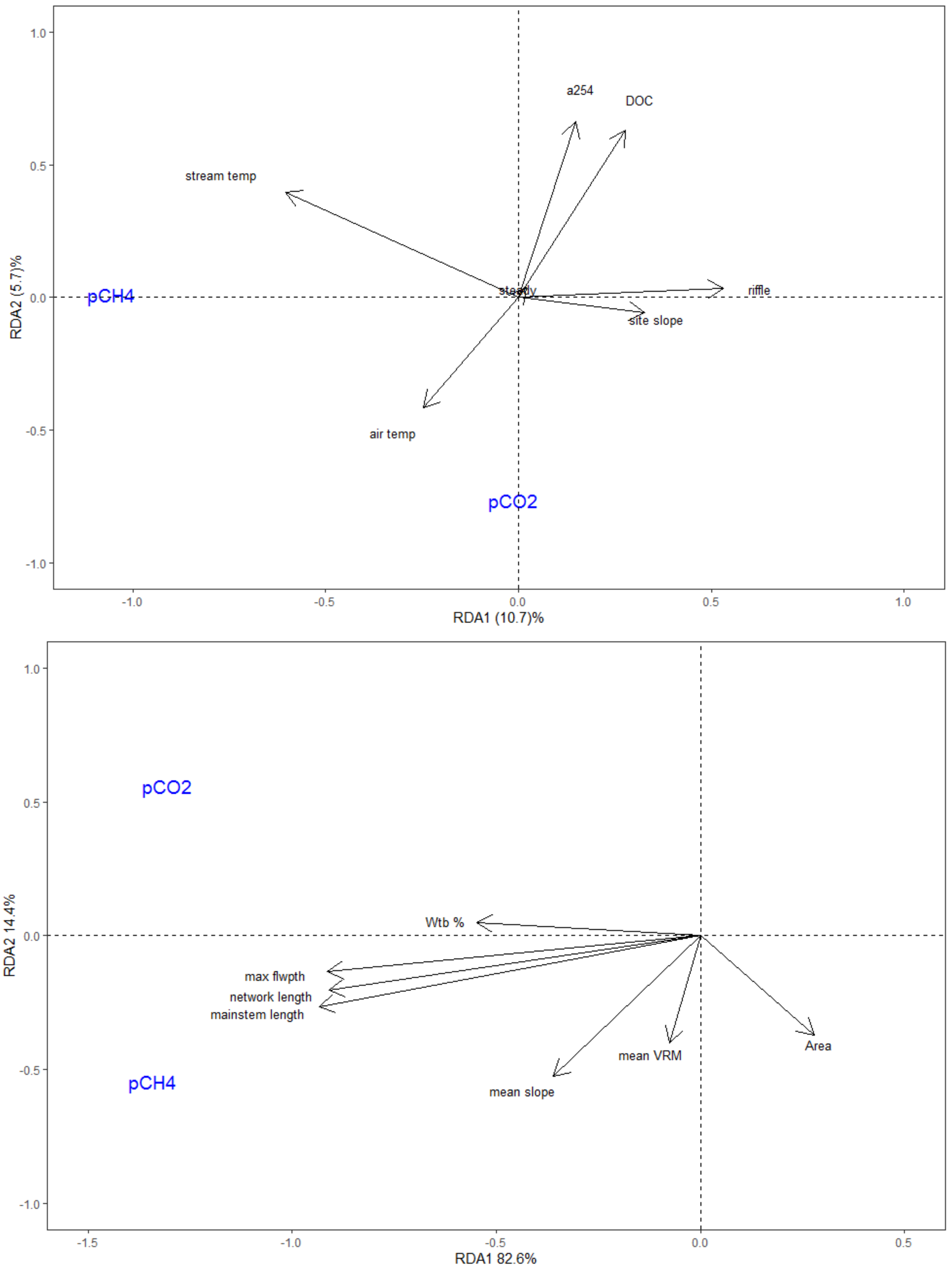

Figure 3.3: RDA model output for pCO_2 and pCH_4 at the reach (n=53) and sub-basin scale (n=10).

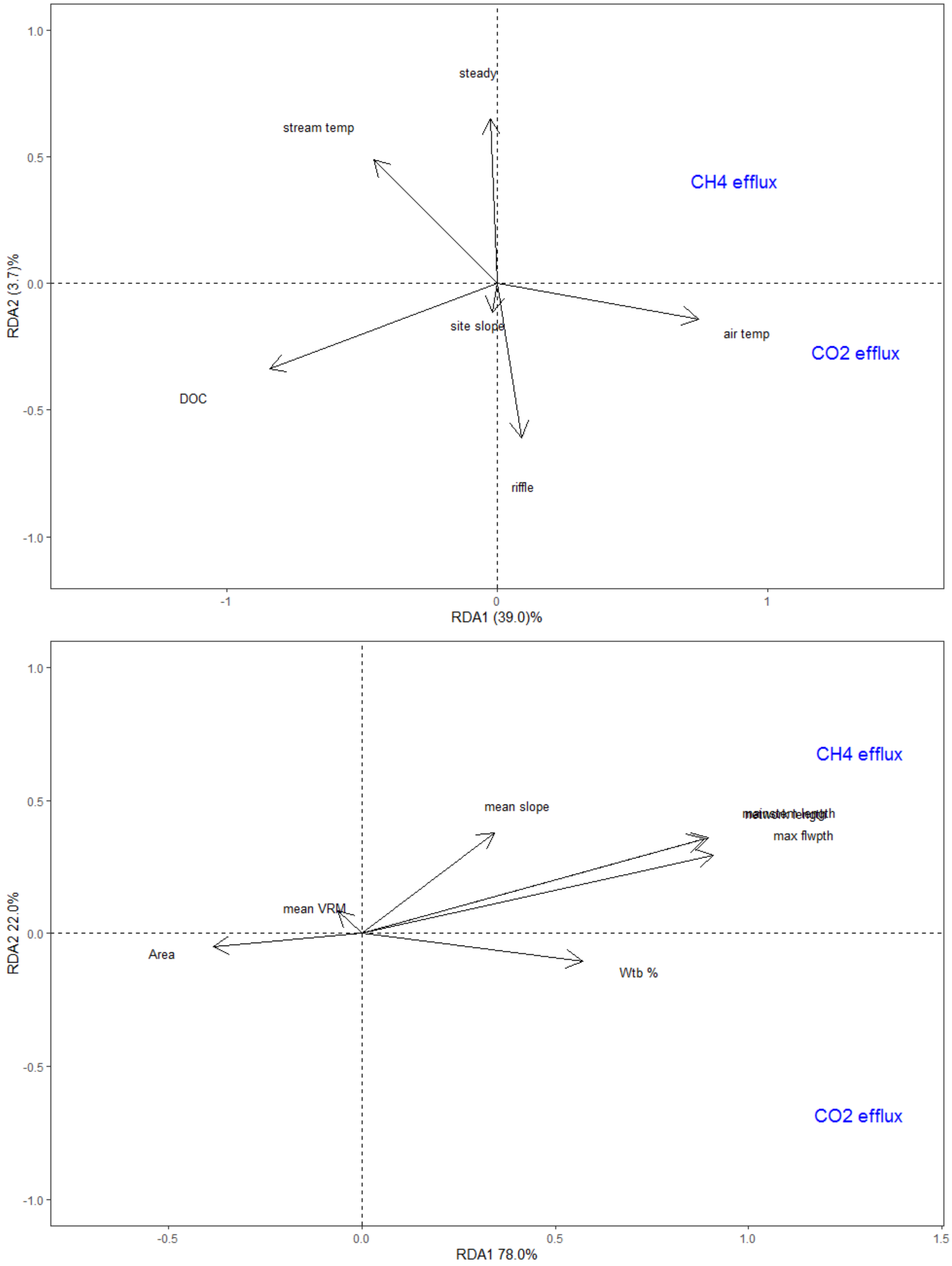

Figure 3.4: RDA model for CO_2 and CH_4 efflux at the reach (n=22) and sub-basin scale (n=10).

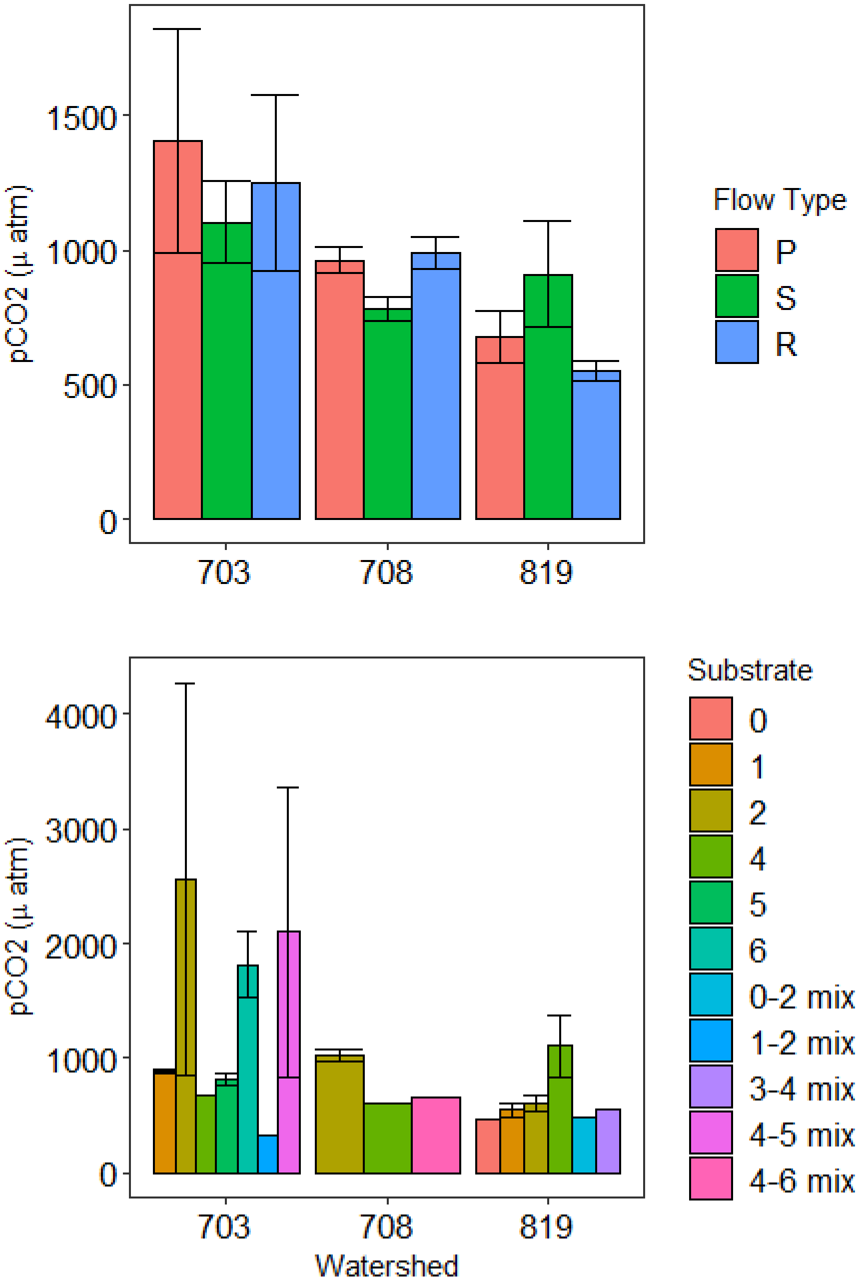

Figure 3.5: Stream pCO_2 per watershed according to flow type: pool (P), riffle (R), and steady (S); and substrate type: bedrock (0), boulders (1), cobbles (2), pebbles (3), gravel (4), sand (5), and muck (6) (n=94).

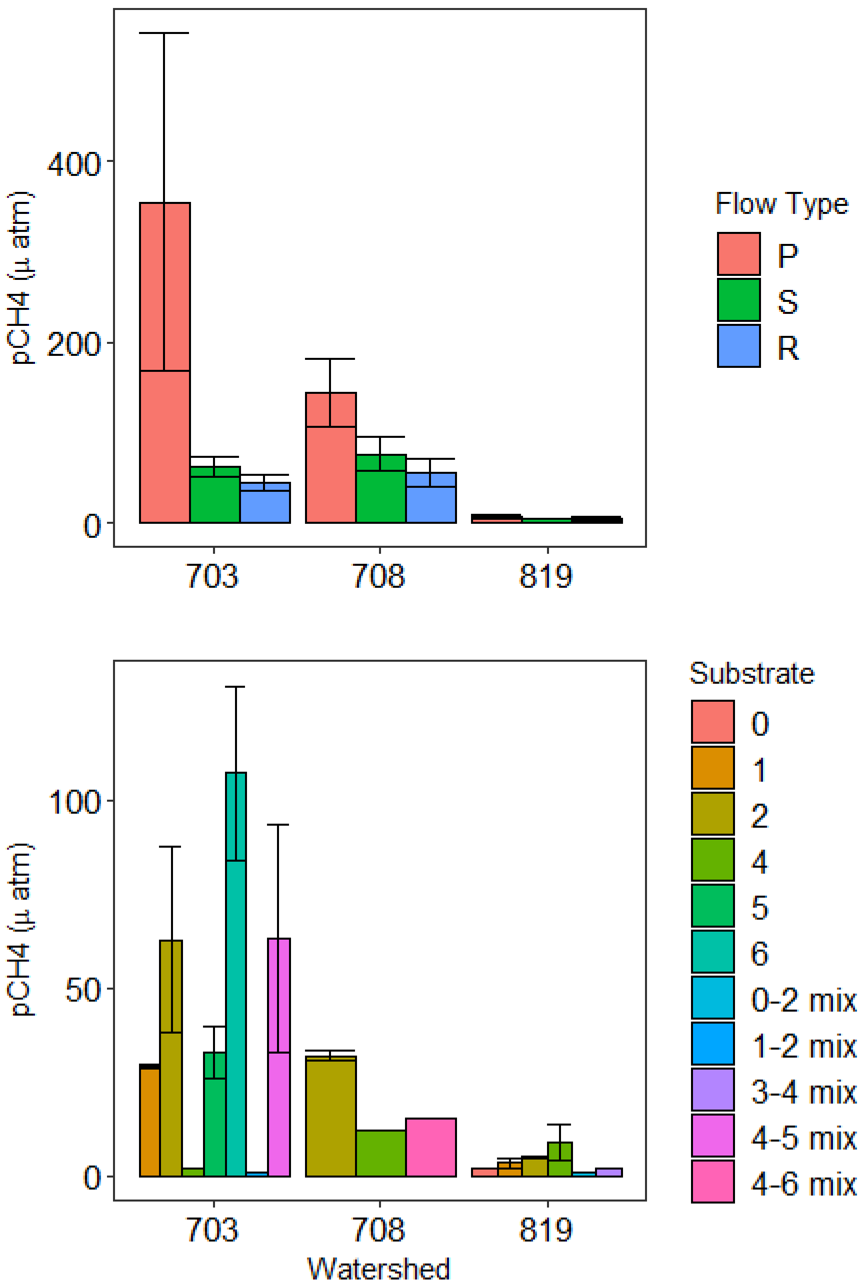

Figure 3.6: Stream pCH_4 per watershed according to flow type: pool (P), riffle (R), and steady (S) (n=94); and substrate type: and substrate type: bedrock (0), boulders (1), cobbles (2), pebbles (3), gravel (4), sand (5), and muck (6) (n=53).

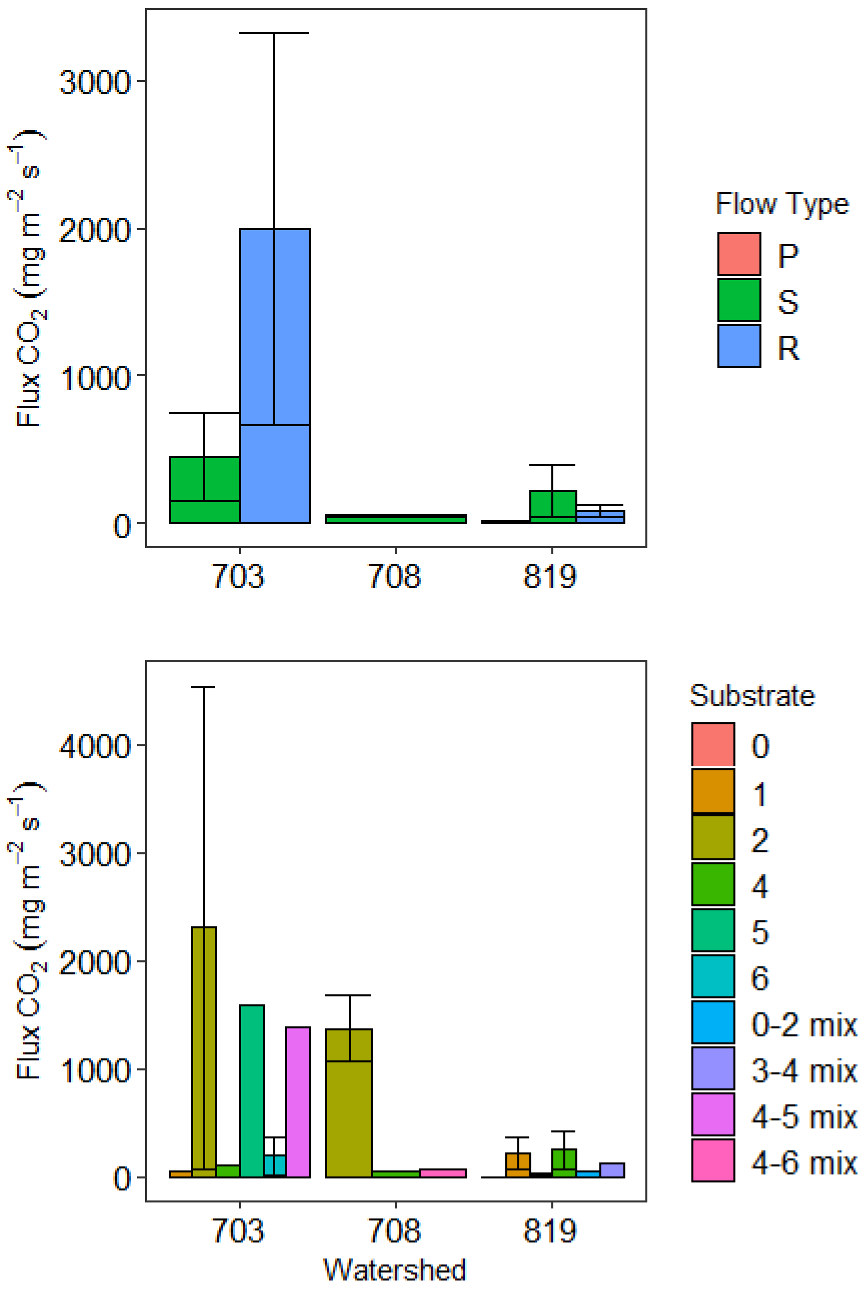

Figure 3.7: Stream CO_2 efflux per watershed according to flow type: pool (P), riffle (R), and steady (S) (n=53). and substrate type: bedrock (0), boulders (1), cobbles (2), pebbles (3), gravel (4), sand (5), and muck (6) (n=53).

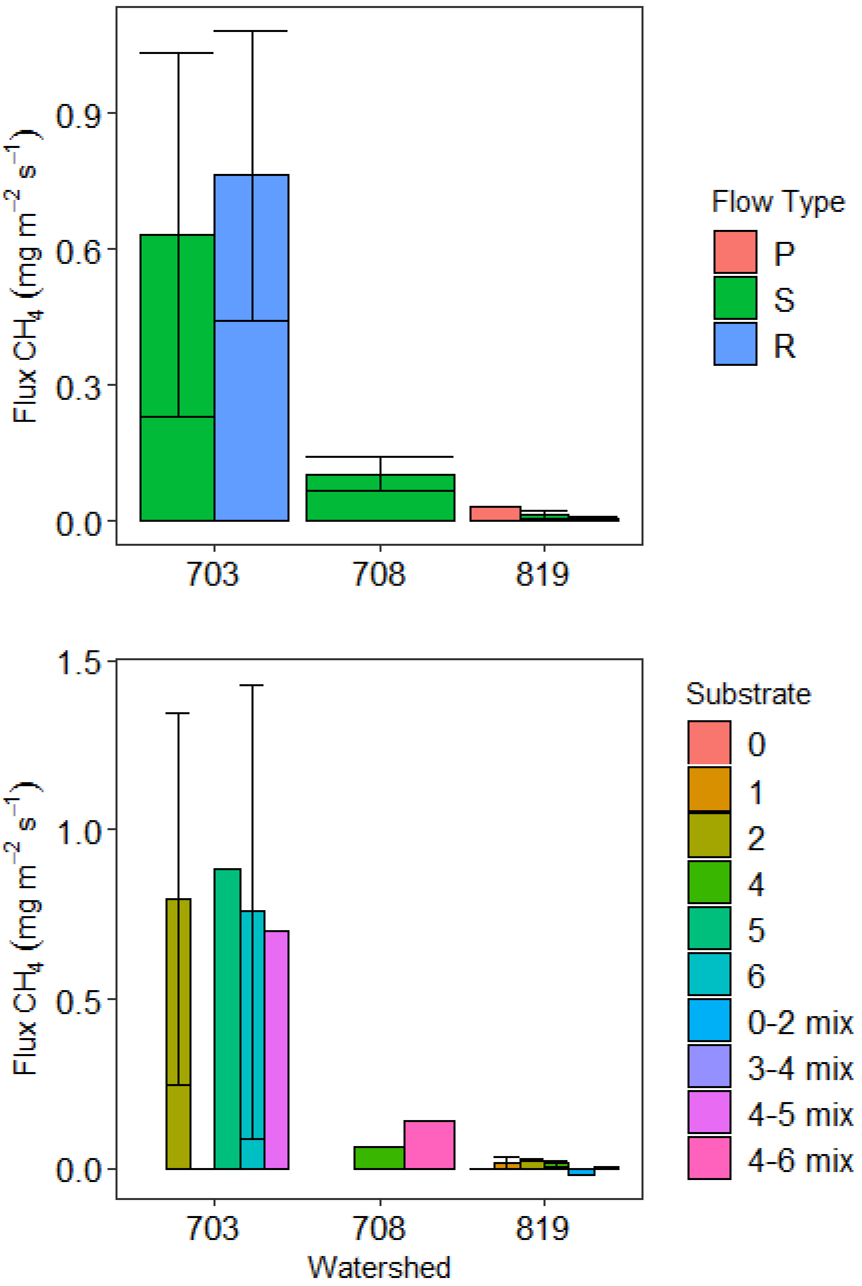

Figure 3.8: CH_4 efflux per watershed according to flow type: pool (P), riffle (R), and steady (S) (n=53); and substrate type: bedrock (0), boulders (1), cobbles (2), pebbles (3), gravel (4), sand (5), and muck (6) (n=53). A lack of data for a specific flow type indicates there were no sample site measurements taken for that type.

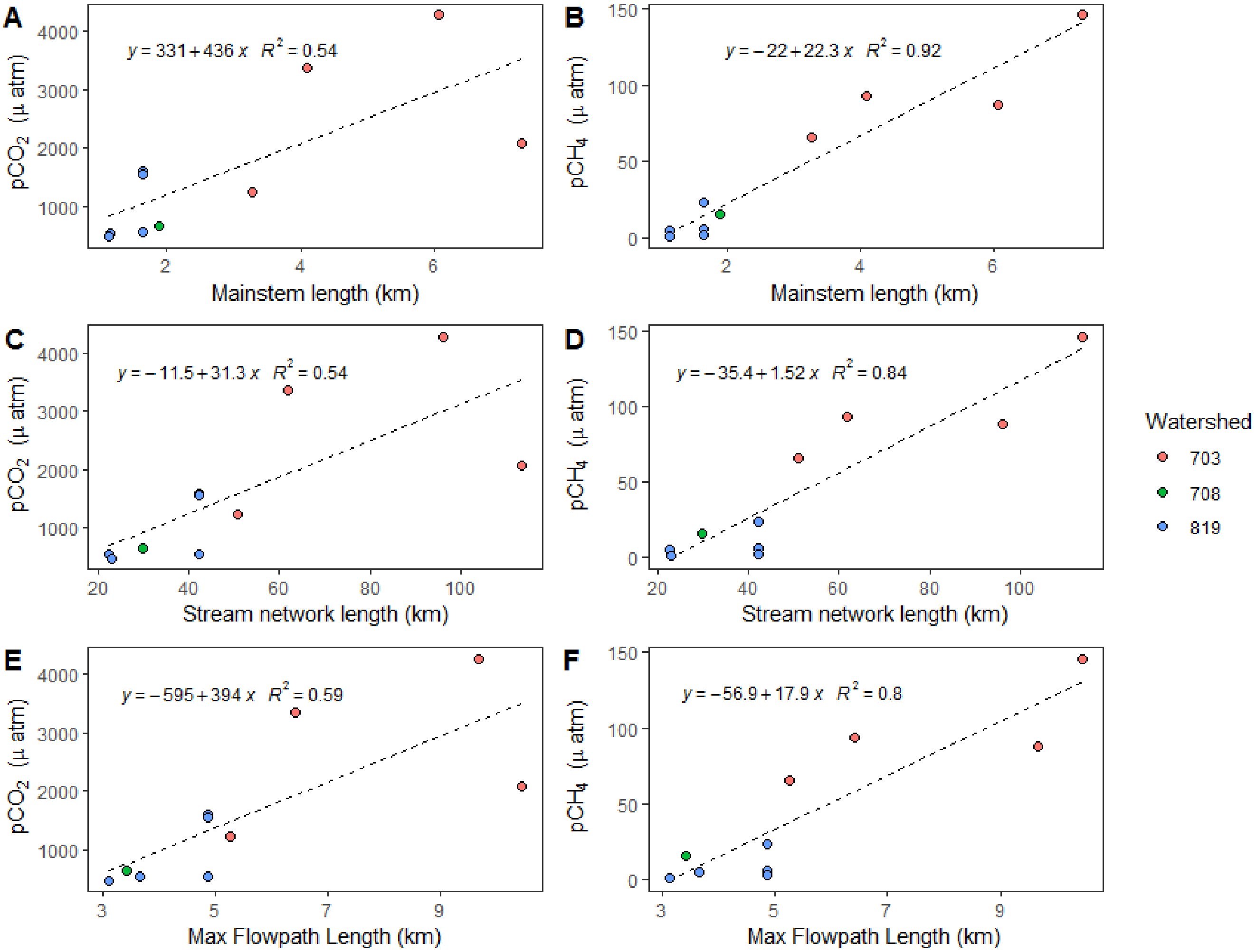

Figure 3.9: Linear regression model output for predictors ($p \leq 0.05$) of pCO_2 and pCH_4 (µatm) as response variables at the sub-basin scale.

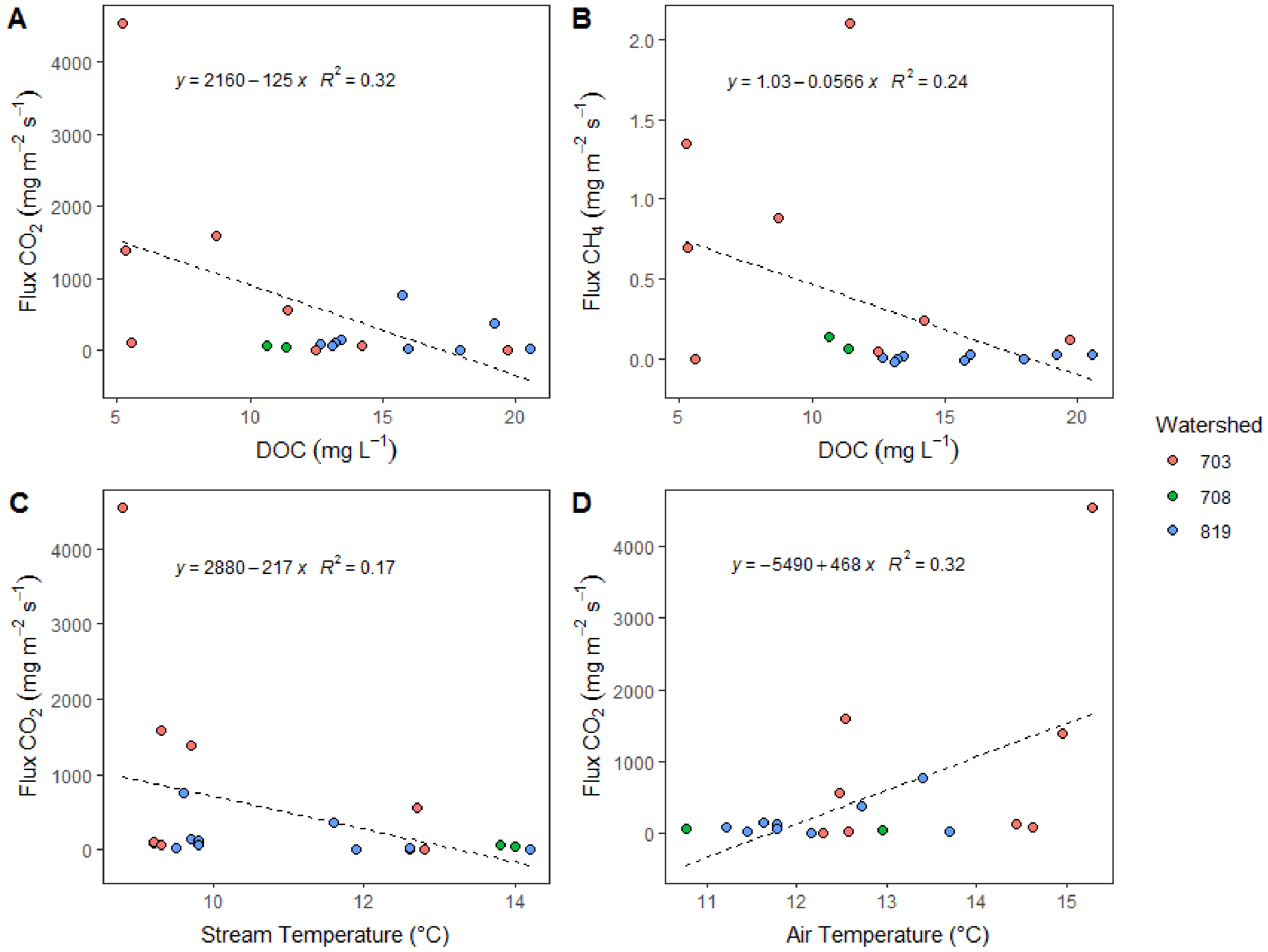

Figure 3.10: Linear regression model output for predictors ($p \leq 0.05$) CO_2 and CH_4 efflux at the reach scale.

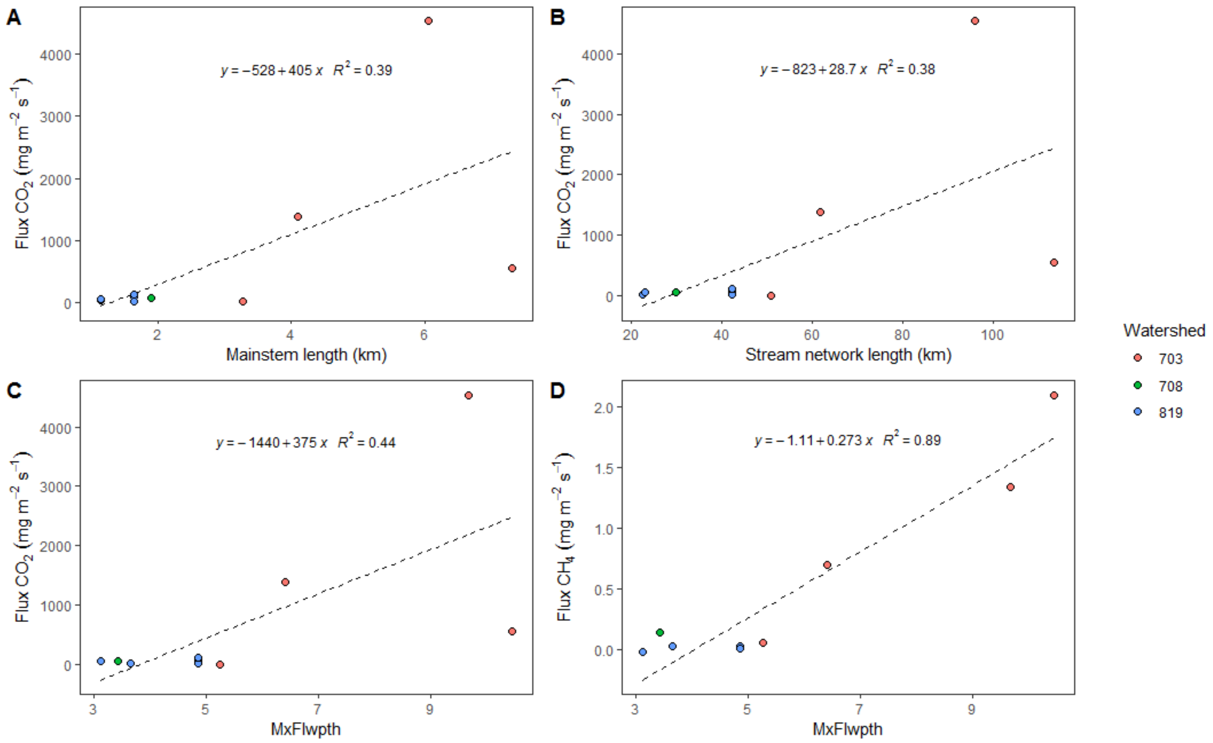

Figure 3.11: Linear regression model output for predictors ($p \leq 0.05$) CO_2 and CH_4 efflux (mg m^{-2} s^{-1}) as response variables at the sub-basin scale.

4.0 General Conclusions

On Calvert Island, the PCTR ecoregion exports a large annual carbon load of terrestrial DOC (Oliver et al., 2017), which coincides with the identification of the PCTR ecoregion as a global DOC export hotspot in Mayorga et al. (2010). Cumulatively, stream waters in PCTR watersheds had a mean annual DOC yield of 52.3 MgC km^{-2} (52.3 gC m^{-2}) (Oliver et al., 2017), which is higher than the annual DOC yields of the top 30 rivers ranked by discharge in the world (Raymond and Spencer, 2015). In addition, the PCTR ecoregion has been identified as an area with significantly high freshwater atmospheric CO_2 evasion (Raymond et al. 2013). These studies suggest that the PCTR ecoregion plays a significant role in the global carbon cycle. As such, understanding how the PCTR both affects and is affected by global carbon dynamics is imperative in the context of climate change. Specifically, stream DOC, CO_2, and CH_4 outflows add to carbon pools in the atmosphere and ocean (Ridgwell and Arndt, 2015), which can increase ocean acidification (Bernhardt and Schlesinger, 2013), affect microbial/plankton community structure and function (Loginova et al., 2016; Traving et al., 2017), and the addition of the greenhouse gas CH_4 can accelerate predicted climate scenarios, which involve an increasing frequency and intensity of extreme weather events (Pachauri et al., 2014). It is evident from this research that growing carbon pools in the atmosphere and oceans will have social and ecological ramifications, thus it is critical to determine controls on temporal variability in stream DOC export and CO_2 emissions to predict how future global changes in climate might affect, and in turn be affected by, regional PCTR carbon export and emissions. Although the study by Oliver et al. (2017) was the first to quantify, characterize, and propose controls for DOC export from this data-poor region of British Columbia's central coast, there have been no studies that quantitatively assess the drivers of stream DOC or dissolved CO_2 and CH_4 partial pressures and efflux. At a broader scale, this study will add to the small but growing body of literature employing high-frequency, *in situ* sensors and spatial sampling to analyze freshwater DOC, CO_2, and CH_4 flux.

This bulk of this research project contributes to a growing field of hysteresis analyses on DOC and discharge within temperate streams. In Chapter 2 we present the first hysteresis analysis to be conducted within the NPCTR, which provides new insight into temporal variation in lateral, subsurface DOC transport, and soluble C flow in general, in this perhumid ecoregion. In addition, our analysis provides a mechanistic foundation that allows for general predictions to be made about the quantity and timing of DOC transport and stream DOC pulses in this ecoregion under the effects of global climate change. Chapter 2 also integrated multiple diagnostic tools that are often used separately, i.e. the HI/FI and C-Q plots, to allow for a comprehensive study of the hydro-biogeochemical processes occurring in this ecoregion. In Chapter 3, we deliver stream CO_2 and CH_4 partial pressure and efflux measurements for this understudied high-carbon region. In addition, the comparison of environmental influences on CO_2 and CH_4 partial pressure and efflux at different spatial scales is a relatively novel approach, and our results provide unique contributions to developing knowledge on the integrated effects of the larger spatiotemporal watershed network on stream reach carbon dynamics. This provides a first step towards using watershed network properties as predictors of reach carbon dynamics, for example, in work done by Bertuzzo et al. (2017). Both Chapters contain important contributions to furthering our understanding of C cycling in the NPCTR, and the role of temperate rainforest streams in the global carbon cycle and their potential feedback with global climate change.

This project has provided a thorough, mechanistic investigation into lateral, subsurface DOC transport dynamics and their temporal variation in a region where this type of hysteresis analysis has not been done before, and where the temporal variation in stream DOC at various timescales has not been well understood. It has also provided measurements of stream CO_2 and CH_4 partial pressure and efflux, allowing for a greater understanding of the role of coastal temperate rainforest streams in the global carbon cycle. In summary, this project presents valuable contributions to furthering knowledge of temporal variation in stream DOC and drivers of lateral DOC transport; as well as CO_2 and CH_4 partial pressure and efflux and their drivers at multiple spatial scales in the NPCTR. Future work to advance the research conducted in this project should focus on verifying the lateral DOC transport model presented by our hysteresis analysis, employing methods such as isotope tracers to define subsurface flowpath inputs, soil pore water sampling and analysis, and direct assessments of soil moisture. A full carbon budget should also be developed for the region, as it would integrate the current disparate C measurements of DOC concentration (export and yield), CO_2 and CH_4 partial pressure, and CO_2 and CH_4 efflux into a comprehensive biogeochemical model, to make quantitative predictions of regional C cycling under different future climate change emissions scenarios in the NPCTR.

Bibliography

Aguilera, R., & Melack, J. M. (2018). Concentration-Discharge Responses to Storm Events in Coastal California Watersheds. *Water Resources Research*, *54*(1), 407-424.

Alaback, P. B. (1996). Biodiversity patterns in relation to climate: the coastal temperate rainforests of North America. In *High-latitude rainforests and associated ecosystems of the West Coast of the Americas* (pp. 105-133). Springer, New York, NY.

Arnold, J. G., & Allen, P. M. (1999). Automated methods for estimating baseflow and ground water recharge from streamflow records 1. *JAWRA Journal of the American Water Resources Association*, *35*(2), 411-424.

Aufdenkampe, A. K., Mayorga, E., Raymond, P. A., Melack, J. M., Doney, S. C., Alin, S. R., ... & Yoo, K. (2011). Riverine coupling of biogeochemical cycles between land, oceans, and atmosphere. *Frontiers in Ecology and the Environment*, *9*(1), 53-60.

Baker, E. B., & Showers, W. J. (2019). Hysteresis analysis of nitrate dynamics in the Neuse River, NC. *Science of The Total Environment*, *652*, 889-899.

Banner, A., LePage, P., Moran, J., & de Groot, A. (2005). The HyP 3 Project: pattern, process, and productivity in hypermaritime forests of coastal British Columbia–a synthesis of 7-year results. *BC Min. For. Res. Br. Vic. BC Spec. Rep*, *10*, 142.

Barbour, M. G., & Billings, W. D. (Eds.). (2000). *North American terrestrial vegetation*. Cambridge University Press.

Basu, N. B., Destouni, G., Jawitz, J. W., Thompson, S. E., Loukinova, N. V., Darracq, A., ... & Rao, P. S. C. (2010). Nutrient loads exported from managed catchments reveal emergent biogeochemical stationarity. *Geophysical Research Letters*, *37*(23).

Bastviken, D., Tranvik, L. J., Downing, J. A., Crill, P. M., & Enrich-Prast, A. (2011). Freshwater methane emissions offset the continental carbon sink. *Science*, *331*(6013), 50-50.

Berggren, M., & del Giorgio, P. A. (2015). Distinct patterns of microbial metabolism associated to riverine dissolved organic carbon of different source and quality. *Journal of Geophysical Research: Biogeosciences*, *120*(6), 989-999.

Bernal, S., Lupon, A., Catalán, N., Castelar, S., & Martí, E. (2018). Decoupling of dissolved organic matter patterns between stream and riparian groundwater in a headwater forested catchment. *Hydrology and Earth System Sciences*, *22*(3), 1897-1910.

Bertilsson, S., & Tranvik, L. J. (2000). Photochemical transformation of dissolved organic matter in lakes. *Limnology and Oceanography*, *45*(4), 753-762.

Bertuzzo, E., Helton, A. M., Hall Jr, R. O., & Battin, T. J. (2017). Scaling of dissolved organic carbon removal in river networks. *Advances in water resources*, *110*, 136-146.

Bieroza, M. Z., & Heathwaite, A. L. (2015). Seasonal variation in phosphorus concentration–discharge hysteresis inferred from high-frequency in situ monitoring. *Journal of Hydrology*, *524*, 333-347.

Birkel, C., Broder, T., & Biester, H. (2017). Nonlinear and threshold-dominated runoff generation controls DOC export in a small peat catchment. *Journal of Geophysical Research: Biogeosciences*, 498–513.

Birkel, C., Broder, T., & Biester, H. (2017, April). Non-linear, connectivity and threshold-dominated runoff-generation controls DOC and heavy metal export in a small peat catchment. In *EGU General Assembly Conference Abstracts* (Vol. 19, p. 11297).

Birkel, C., Soulsby, C., & Tetzlaff, D. (2014). Integrating parsimonious models of hydrological connectivity and soil biogeochemistry to simulate stream DOC dynamics. *Journal of Geophysical Research: Biogeosciences*, *119*(5), 1030-1047.

Borges, A. V., Abril, G., Darchambeau, F., Teodoru, C. R., Deborde, J., Vidal, L. O., ... & Bouillon, S. (2015). Divergent biophysical controls of aquatic CO 2 and CH 4 in the World's two largest rivers. *Scientific Reports*, *5*, 15614.

Butman, D., & Raymond, P. A. (2011). Significant efflux of carbon dioxide from streams and rivers in the United States. *Nature Geoscience*, *4*(12), 839–842. https://doi.org/10.1038/ngeo1294

Butturini, A., Alvarez, M., Bernal, S., Vazquez, E., & Sabater, F. (2008). Diversity and temporal sequences of forms of DOC and NO3-discharge responses in an intermittent stream: Predictable or random succession?. *Journal of Geophysical Research: Biogeosciences*, *113*(G3).

Butturini, A., Francesc, G., Jérôme, L., Eusebi, V., & Francesc, S. (2006). Cross-site comparison of variability of DOC and nitrate c–q hysteresis during the autumn–winter period in three Mediterranean headwater streams: a synthetic approach. *Biogeochemistry*, *77*(3), 327-349.

Cerro, I., Sanchez-Perez, J. M., Ruiz-Romera, E., & Antigüedad, I. (2014). Variability of particulate (SS, POC) and dissolved (DOC, NO3) matter during storm events in the Alegria agricultural watershed. *Hydrological processes*, *28*(5), 2855-2867.

Coch, C., Lamoureux, S. F., Knoblauch, C., Eischeid, I., Fritz, M., Obu, J., & Lantuit, H. (2018). Summer rainfall DOC, solute and sediment fluxes in a small Arctic coastal catchment on Herschel Island (Yukon Territory, Canada). *Arctic Science*, (ja).

Cole, J. J., & Caraco, N. F. (2001). Carbon in catchments: connecting terrestrial carbon losses with aquatic metabolism. *Marine and Freshwater Research*, *52*(1), 101-110.

Couturier, M., Nozais, C., & Chaillou, G. (2016). Microtidal subterranean estuaries as a source of fresh terrestrial dissolved organic matter to the coastal ocean. *Marine Chemistry*, *186*, 46–57. https://doi.org/10.1016/j.marchem.2016.08.001

Creed, I. F., McKnight, D. M., Pellerin, B. A., Green, M. B., Bergamaschi, B. A., Aiken, G. R., ... & Aulenbach, B. T. (2015). The river as a chemostat: fresh perspectives on dissolved organic matter flowing down the river continuum. *Canadian Journal of Fisheries and Aquatic Sciences*, *72*(8), 1272-1285.

D'Amore, D. V., Edwards, R. T., Herendeen, P. A., Hood, E., & Fellman, J. B. (2015). Dissolved organic carbon fluxes from hydropedologic units in Alaskan coastal temperate rainforest watersheds. *Soil Science Society of America Journal*, *79*(2), 378-388.

Danielescu, S., MacQuarrie, K. T., & Popa, A. (2018). SEPHYDRO: A Customizable Online Tool for Hydrograph Separation. *Groundwater*.

DellaSala, D. A., Brandt, P., Koopman, M., Leonard, J., Meisch, C., Herzog, P., ... & von Wehrden, H. (2015). Climate change may trigger broad shifts in North America's Pacific Coastal rainforests. *Reference Module in Earth Systems and Environmental Sciences.*

Dick, J. J., Tetzlaff, D., Birkel, C., & Soulsby, C. (2015). Modelling landscape controls on dissolved organic carbon sources and fluxes to streams. *Biogeochemistry*, *122*(2-3), 361-374.

Diffenbaugh, N. S., Swain, D. L., & Touma, D. (2015). Anthropogenic warming has increased drought risk in California. *Proceedings of the National Academy of Sciences*, *112*(13), 3931-3936.

Downing, B. D., Pellerin, B. A., Bergamaschi, B. A., Saraceno, J. F., & Kraus, T. E. (2012). Seeing the light: The effects of particles, dissolved materials, and temperature on in situ measurements of DOM fluorescence in rivers and streams. *Limnology and Oceanography: Methods*, *10*(10), 767-775.

Drake, T. W., Raymond, P. A., & Spencer, R. G. (2018). Terrestrial carbon inputs to inland waters: A current synthesis of estimates and uncertainty. *Limnology and Oceanography Letters*, *3*(3), 132-142.

Eckard, R. S., Pellerin, B. A., Bergamaschi, B. A., Bachand, P. A., Bachand, S. M., Spencer, R. G., & Hernes, P. J. (2017). Dissolved organic matter compositional change and biolability during two storm runoff events in a small agricultural watershed. *Journal of Geophysical Research: Biogeosciences*, *122*(10), 2634-2650.

Eckhardt, K. (2005). How to construct recursive digital filters for baseflow separation. *Hydrological Processes: An International Journal*, *19*(2), 507-515.

Emili, L. A., & Price, J. S. (2013). Biogeochemical processes in the soil-groundwater system of a forest-peatland complex, north coast British Columbia, Canada. *Northwest Science*, *87*(4), 326-348.

Evans, C., & Davies, T. D. (1998). Causes of concentration/discharge hysteresis and its potential as a tool for analysis of episode hydrochemistry. *Water Resources Research*, *34*(1), 129-137.

Fedora, M. A., & Beschta, R. L. (1989). Storm runoff simulation using an antecedent precipitation index (API) model. *Journal of hydrology*, *112*(1-2), 121-133.

Fellman, J. B., Buma, B., Hood, E., Edwards, R. T., & D'Amore, D. V. (2016). Linking LiDAR with streamwater biogeochemistry in coastal temperate rainforest watersheds. *Canadian journal of fisheries and aquatic sciences*, *74*(6), 801-811.

Findlay, S., & Sinsabaugh, R. L. (1999). Unravelling the sources and bioavailability of dissolved organic matter in lotic aquatic ecosystems. *Marine and Freshwater Research*, *50*(8), 781-790.

Findlay, S., & Sinsabaugh, R. L. (Eds.). (2003). *Aquatic ecosystems: interactivity of dissolved organic matter*. Academic Press.

Fosu, B. O., Simon Wang, S. Y., & Yoon, J. H. (2016). The 2014/15 snowpack drought in Washington State and its climate forcing. *Bulletin of the American Meteorological Society*, *97*(12), S19-S24.

Fovet, O., Humbert, G., Dupas, R., Gascuel-Odoux, C., Gruau, G., Jaffrézic, A., ... & Grimaldi, C. (2018). Seasonal variability of stream water quality response to storm events captured using high-frequency and multi-parameter data. *Journal of Hydrology*, *559*, 282-293.

Fraser, C. J. D., Roulet, N. T., & Moore, T. R. (2001). Hydrology and dissolved organic carbon biogeochemistry in an ombrotrophic bog. *Hydrological Processes*, *15*(16), 3151-3166.

Futter, A. M. N., Löfgren, S., Köhler, S. J., Lundin, L., Moldan, F., Bringmark, L., & Ko, S. J. (n.d.). Simulating Dissolved Organic Carbon Dynamics at the Swedish Integrated Monitoring Sites with the Integrated Catchments Model for Carbon , INCA-C Simulating Dissolved Organic Carbon Dynamics at the Swedish Integrated Monitoring Sites with the Integrated Ca, *40*(8), 906–919. https://doi.org/10.1007/s13280-011-0203-z

Godsey, S. E., Kirchner, J. W., & Clow, D. W. (2009). Concentration–discharge relationships reflect chemostatic characteristics of US catchments. *Hydrological Processes: An International Journal*, *23*(13), 1844-1864.

Gonzalez, S. A. (2015). LiDAR derived watersheds with metrics – Calvert Island. *Hakai Institute.* http://services1.arcgis.com/TLdVcW1aE8FOKj1g/arcgis/rest/services/final_F_watersheds/FeatureServer

Green, R. N. (2014). Reconnaissance Level Terrestrial Ecosystem Mapping of Priority Landscape Units of 309 the Coast EBM Planning Area: Phase 3. *Vancouver, Canada: Blackwell and Associates*.

Hamann, A., Wang, T., Spittlehouse, D. L., & Murdock, T. Q. (2013). A comprehensive, high-resolution database of historical and projected climate surfaces for western North America. *Bulletin of the American Meteorological Society*, *94*(9), 1307-1309.

Hendrickson, G. E., & Krieger, R. A. (1964). *Geochemistry of natural waters of the Blue Grass region, Kentucky* (No. 1700). US Govt. Print. Off.

Herendeen, P. (2014). Water table fluctuations and runoff generation in three catchment types in a coastal temperate rainforest.

Herndon, E. M., Dere, A. L., Sullivan, P. L., Norris, D., Reynolds, B., & Brantley, S. L. (2015). Landscape heterogeneity drives contrasting concentration–discharge relationships in shale headwater catchments. *Hydrology and Earth System Sciences*, *19*(8), 3333-3347.

Hutchins, R. H., Prairie, Y. T., & del Giorgio, P. A. (2019). Large-Scale Landscape Drivers of CO_2, CH_4 , DOC, and DIC in Boreal River Networks. *Global Biogeochemical Cycles*, *33*(2), 125-142.

Inamdar, S. P., Christopher, S. F., & Mitchell, M. J. (2004). Export mechanisms for dissolved organic carbon and nitrate during summer storm events in a glaciated forested catchment in New York, USA. *Hydrological Processes*, *18*(14), 2651-2661.

Johnston, S. E., Shorina, N., Bulygina, E., Vorobjeva, T., Chupakova, A., Klimov, S. I., ... & Spencer, R. G. (2018). Flux and seasonality of dissolved organic matter from the Northern Dvina (Severnaya Dvina) River, Russia. *Journal of Geophysical Research: Biogeosciences*, *123*(3), 1041-1056.

Jones Jr, J. B., & Mulholland, P. J. (1998). Carbon dioxide variation in a hardwood forest stream: an integrative measure of whole catchment soil respiration. *Ecosystems*, *1*(2), 183-196.

Kämäri, M., Tattari, S., Lotsari, E., Koskiaho, J., & Lloyd, C. E. M. (2018). High-frequency monitoring reveals seasonal and event-scale water quality variation in a temporally frozen river. *Journal of hydrology*, *564*, 619-639.

Keesstra, S. D., Davis, J., Masselink, R. H., Casalí, J., Peeters, E. T., & Dijksma, R. (2019). Coupling hysteresis analysis with sediment and hydrological connectivity in three agricultural catchments in Navarre, Spain. *Journal of Soils and Sediments*, 1-15.

Kellogg, E. L. (1995). The rainforests of home: an atlas of people and place. *Authored by EC Wolf, AP Mitchell, and PK Schoonmaker. Published by Ecotrust, Pacific GIS, and Conservation International. Portland, OR*.

Knorr, K. H. (2013). DOC-dynamics in a small headwater catchment as driven by redox fluctuations and hydrological flow paths–are DOC exports mediated by iron reduction/oxidation cycles?. *Biogeosciences*, *10*(2), 891-904.

Koenig, L. E., Shattuck, M. D., Snyder, L. E., Potter, J. D., & McDowell, W. H. (2017). Deconstructing the Effects of Flow on DOC, Nitrate, and Major Ion Interactions Using a High-Frequency Aquatic Sensor Network. *Water Resources Research*, *53*(12), 10655-10673.

Korver, M.C., Floyd, W.C., Brunsting, R. (2019). Observed stream flow from seven small coastal watersheds in British Columbia, Canada. Version 3.0. Hakai Institute. Dataset. https://doi.org/10.21966/sbyc-d030

Lauerwald, R., Laruelle, G. G., Hartmann, J., Ciais, P., & Regnier, P. A. (2015). Spatial patterns in CO_2 evasion from the global river network. *Global Biogeochemical Cycles*, *29*(5), 534-554.

Lawler, D. M., Petts, G. E., Foster, I. D., & Harper, S. (2006). Turbidity dynamics during spring storm events in an urban headwater river system: The Upper Tame, West Midlands, UK. *Science of the Total Environment*, *360*(1-3), 109-126.

Le Quéré, C., Andrew, R., Canadell, J. G., Sitch, S., Korsbakken, J. I., Peters, G. P., ... & Keeling, R. F. (2016). Global carbon budget 2016.

Levy-Booth, D. J., Giesbrecht, I. J., Kellogg, C. T., Heger, T. J., D'Amore, D. V., Keeling, P. J., ... & Mohn, W. W. (2019). Seasonal and ecohydrological regulation of active microbial populations involved in DOC, CO 2, and CH 4 fluxes in temperate rainforest soil. *The ISME journal*, *13*(4), 950.

Lloyd, C. E. M., Freer, J. E., Johnes, P. J., & Collins, A. L. (2016a). Using hysteresis analysis of high-resolution water quality monitoring data, including uncertainty, to infer controls on nutrient and sediment transfer in catchments. *Science of the Total Environment*, *543*, 388-404.

Lloyd, C. E. M., Freer, J. E., Johnes, P. J., & Collins, A. L. (2016b). Testing an improved index for analysing storm discharge–concentration hysteresis. *Hydrology and Earth System Sciences*, *20*(2), 625-632.

Lloyd, C. E. M., Freer, J. E., Johnes, P. J., & Collins, A. L. (2016b). Testing an improved index for analysing storm discharge–concentration hysteresis. *Hydrology and Earth System Sciences*, *20*(2), 625-632.

Long, D. T., Voice, T. C., Xagaroraki, I., Chen, A., Wu, H., Lee, E., ... & Xing, F. (2017). Patterns of cq hysteresis loops and within an integrative pollutograph for selected inorganic and organic solutes and E. coli in an urban salted watershed during winter-early spring periods. *Applied Geochemistry*, *83*, 93-107.

Lyne, V., & Hollick, M. (1979, September). Stochastic time-variable rainfall-runoff modelling. In *Institute of Engineers Australia National Conference* (Vol. 1979, pp. 89-93). Barton, Australia: Institute of Engineers Australia.

Martin, J. M., & Meybeck, M. (1979). Elemental mass-balance of material carried by major world rivers. *Marine chemistry*, *7*(3), 173-206.

Mayorga, E., Aufdenkampe, A. K., Masiello, C. A., Krusche, A. V., Hedges, J. I., Quay, P. D., ... & Brown, T. A. (2005). Young organic matter as a source of carbon dioxide outgassing from Amazonian rivers. *Nature*, *436*(7050), 538.

Mayorga, E., Seitzinger, S. P., Harrison, J. A., Dumont, E., Beusen, A. H., Bouwman, A. F., ... & Van Drecht, G. (2010). Global nutrient export from WaterSheds 2 (NEWS 2): model development and implementation. *Environmental Modelling & Software*, *25*(7), 837-853.

McKnight, D. M., Boyer, E. W., Westerhoff, P. K., Doran, P. T., Kulbe, T., & Andersen, D. T. (2001). Spectrofluorometric characterization of dissolved organic matter for indication of precursor organic material and aromaticity. *Limnology and Oceanography*, *46*(1), 38-48.

McNicol, G., Bulmer, C., D'Amore, D., Sanborn, P., Saunders, S., Giesbrecht, I., Gonzalez-Arriola, S., Bidlack, A., Butman, D., and Buma, B. (2019). Large, climate-sensitive soil carbon stocks mapped with pedology-informed machine learning in the North Pacific coastal temperate rainforest. *Environmental Research Letters*, *14*(1), 014004.

Meinson, P., Idrizaj, A., & Laas, A. (2016). Continuous and high-frequency measurements in limnology : history , applications , and future challenges, *62*(October 2015), 52–62.

Melching, C. S., & Flores, H. E. (1999). Reaeration equations derived from US Geological Survey database. *Journal of Environmental Engineering*, *125*(5), 407-414.

Meybeck, M. (1979). Major elements contents of river waters and dissolved inputs to the oceans. *Revue de Géologie dynamique et de Géographie physique*, *21*(3), 215-246.

Meyer, J. L., Wallace, J. B., & Eggert, S. L. (1998). Leaf litter as a source of dissolved organic carbon in streams. *Ecosystems*, *1*(3), 240-249.

Mladenov, N., McKnight, D. M., Wolski, P., & Ramberg, L. (2005). Effects of annual flooding on dissolved organic carbon dynamics within a pristine wetland, the Okavango Delta, Botswana. *Wetlands*, *25*(3), 622-638.

Moody, C. S., Worrall, F., Evans, C. D., & Jones, T. G. (2013). The rate of loss of dissolved organic carbon (DOC) through a catchment. *Journal of Hydrology*, *492*, 139-150.

Musolff, A., Schmidt, C., Selle, B., & Fleckenstein, J. H. (2015). Catchment controls on solute export. *Advances in water resources*, *86*, 133-146.

Newbold, J. D., O'neill, R. V., Elwood, J. W., & Van Winkle, W. (1982). Nutrient spiralling in streams: implications for nutrient limitation and invertebrate activity. *The American Naturalist*, *120*(5), 628-652.

Oliver, A. A., Tank, S. E., Giesbrecht, I., Korver, M. C., Floyd, W. C., Sanborn, P., ... & Lertzman, K. P. (2017). Globally significant yields of dissolved organic carbon from small watersheds of the Pacific coastal temperate rainforest. *Biogeosciences Discuss*, 1-44.

Osburn, C. L., Oviedo-Vargas, D., Barnett, E., Dierick, D., Oberbauer, S. F., & Genereux, D. P. (2018). Regional groundwater and storms are hydrologic controls on the quality and export of dissolved organic matter in two tropical rainforest streams, Costa Rica. *Journal of Geophysical Research: Biogeosciences*, *123*(3), 850-866.

Outram, F. N., Cooper, R. J., Sünnenberg, G., Hiscock, K. M., & Lovett, A. A. (2016). Antecedent conditions, hydrological connectivity and anthropogenic inputs: Factors affecting nitrate and phosphorus transfers to agricultural headwater streams. *Science of the Total Environment*, *545*, 184-199.

Pellerin, B. A., Saraceno, J. F., Shanley, J. B., Sebestyen, S. D., Aiken, G. R., Wollheim, W. M., & Bergamaschi, B. A. (2012). Taking the pulse of snowmelt: in situ sensors reveal seasonal, event and diurnal patterns of nitrate and dissolved organic matter variability in an upland forest stream. *Biogeochemistry*, *108*(1-3), 183-198.

Pojar, J., Klinka, K., & Meidinger, D. V. (1987). Biogeoclimatic ecosystem classification in British Columbia. *Forest Ecology and Management*, *22*(1-2), 119-154.

Rasilo, T., Hutchins, R. H., Ruiz-González, C., & Del Giorgio, P. A. (2017). Transport and transformation of soil-derived CO_2, $CH_4$and DOC sustain CO_2 supersaturation in small boreal streams. *Science of The Total Environment*, *579*, 902-912.

Raymond, P. A., & Saiers, J. E. (2010). Event controlled DOC export from forested watersheds. *Biogeochemistry*, *100*(1-3), 197-209.

Raymond, P. A., & Spencer, R. G. (2015). Riverine DOM. *Biogeochemistry of marine dissolved organic matter, edited by: Hansell, DA and Carlson, CA, second Edn., Academic Press, San Diego, USA*, 509-533.

Raymond, P. A., Hartmann, J., Lauerwald, R., Sobek, S., McDonald, C., Hoover, M., ... & Kortelainen, P. (2013). Global carbon dioxide emissions from inland waters. *Nature*, *503*(7476), 355.

Raymond, P. A., Zappa, C. J., Butman, D., Bott, T. L., Potter, J., Mulholland, P., ... & Newbold, D. (2012). Scaling the gas transfer velocity and hydraulic geometry in streams and small rivers. *Limnology and Oceanography: Fluids and Environments*, *2*(1), 41-53.

Roddick, J. A. (1996). Queens Sound (102P) British Columbia: Geological Survey of Canada, Open File 3278, scale 1: 250,000. *Ottawa, Canada: Natural Resources Canada*.

Rode, M., Wade, A. J., Cohen, M. J., Hensley, R. T., Bowes, M. J., Kirchner, J. W., … Jomaa, S. (2016). Sensors in the Stream: The High-Frequency Wave of the Present. *Environmental*

Science and Technology, *50*(19). https://doi.org/10.1021/acs.est.6b02155

Rodríguez-Blanco, M. L., Soto-Varela, F., Taboada-Castro, M. M., & Taboada-Castro, M. T. (2018). Using hysteresis analysis to infer controls on sediment-associated and dissolved metals transport in a small humid temperate catchment. *Journal of Hydrology*, *565*, 49-60.

Rose, Lucy & Karwan, Diana & E. Godsey, Sarah. (2018). Concentration-discharge relationships describe solute and sediment mobilization, reaction, and transport at event and longer time scales. *Hydrological Processes.* 10.1002/hyp.13235.

Rutledge, J. M., & Chow-Fraser, P. (2019). Landscape characteristics driving spatial variation in total phosphorus and sediment loading from sub-watersheds of the Nottawasaga River, Ontario. *Journal of environmental management*, *234*, 357-366.

Saraceno, J. F., Pellerin, B. A., Downing, B. D., Boss, E., Bachand, P. A., & Bergamaschi, B. A. (2009). High-frequency in situ optical measurements during a storm event: Assessing relationships between dissolved organic matter, sediment concentrations, and hydrologic processes. *Journal of Geophysical Research: Biogeosciences*, *114*(G4).

Saxton, K. E., & Lenz, A. T. (1967). Antecedent retention indexes predict soil moisture. *Journal of the Hydraulics Division*.

Schultz, M., Pellerin, B., Aiken, G., Martin, J., & Raymond, P. (2018). High Frequency Data Exposes Nonlinear Seasonal Controls on Dissolved Organic Matter in a Large Watershed. *Environmental science & technology*, *52*(10), 5644-5652.

Seifert, A., Roth, V., Dittmar, T., Gleixner, G., Breuer, L., Houska, T., & Marxsen, J. (2016). Science of the Total Environment Comparing molecular composition of dissolved organic matter in soil and stream water : In fl uence of land use and chemical characteristics. *Science of the Total Environment, The*, *571*, 142–152. https://doi.org/10.1016/j.scitotenv.2016.07.033

Shanley, C. S., Pyare, S., Goldstein, M. I., Alaback, P. B., Albert, D. M., Beier, C. M., ... & McPhee, M. V. (2015). Climate change implications in the northern coastal temperate rainforest of North America. *Climatic Change*, *130*(2), 155-170.

Shapiro, S. S., & Wilk, M. B. (1965). An analysis of variance test for normality (complete samples). *Biometrika*, *52*(3/4), 591-611.

Smits, A. P., Schindler, D. E., Holtgrieve, G. W., Jankowski, K. J., & French, D. W. (2017). Watershed geomorphology interacts with precipitation to influence the magnitude and source of CO_2 emissions from Alaskan streams. *Journal of Geophysical Research: Biogeosciences*, *122*(8), 1903-1921.

Sprenger, M., Tetzlaff, D., Buttle, J., Carey, S. K., McNamara, J. P., Laudon, H., ... & Soulsby, C. (2018). Storage, mixing, and fluxes of water in the critical zone across northern environments inferred by stable isotopes of soil water. *Hydrological Processes*, *32*(12), 1720-1737.

Strohmeier, S., Knorr, K. H., Reichert, M., Frei, S., Fleckenstein, J. H., Peiffer, S., & Matzner, E. (2013). Concentrations and fluxes of dissolved organic carbon in runoff from a forested catchment: insights from high frequency measurements. *Biogeosciences*, *10*(2), 905-916.

Szeto, K., Zhang, X., White, R. E., & Brimelow, J. (2016). The 2015 extreme drought in Western Canada. *Bulletin of the American Meteorological Society*, *97*(12), S42-S46.

Tank, J. L., Rosi-Marshall, E. J., Griffiths, N. A., Entrekin, S. A., & Stephen, M. L. (2010). A review of allochthonous organic matter dynamics and metabolism in streams. *Journal of the North American Benthological Society*, *29*(1), 118-146.

Tank, S. E., Fellman, J. B., Hood, E., & Kritzberg, E. S. (2018). Beyond respiration: Controls on lateral carbon fluxes across the terrestrial-aquatic interface. *Limnology and Oceanography Letters*, *3*(3), 76-88.

Tank, S. E., Lesack, L. F., & Hesslein, R. H. (2009). Northern delta lakes as summertime CO 2 absorbers within the arctic landscape. *Ecosystems*, *12*(1), 144-157.

Tank, S. E., Striegl, R. G., McClelland, J. W., & Kokelj, S. V. (2016). Multi-decadal increases in dissolved organic carbon and alkalinity flux from the Mackenzie drainage basin to the Arctic Ocean. *Environmental Research Letters*, *11*(5), 054015.

Team, R. C. (2013). R: A language and environment for statistical computing.

Thompson, S. D., Nelson, T. A., Giesbrecht, I., Frazer, G., & Saunders, S. C. (2016). Data-driven regionalization of forested and non-forested ecosystems in coastal British Columbia with LiDAR and RapidEye imagery. *Applied Geography*, *69*, 35-50.

Thornthwaite, C. W. (1948). An approach toward a rational classification of climate. *Geographical review*, *38*(1), 55-94.

Toler, L. G. (1965). Relation between chemical quality and water discharge in Spring Creek, southwestern Georgia. *US Geological Survey Professional Paper*, *525*, C209-13.

Tunaley, C., Tetzlaff, D., Lessels, J., & Soulsby, C. (2016). Linking high-frequency DOC dynamics to the age of connected water sources. *Water Resources Research*, *52*(7), 5232-5247.

Vannote, R. L., Minshall, G. W., Cummins, K. W., Sedell, J. R., & Cushing, C. E. (1980). The river continuum concept. *Canadian journal of fisheries and aquatic sciences*, *37*(1), 130-137.

Vaughan, M. C., Bowden, W. B., Shanley, J. B., Vermilyea, A., Sleeper, R., Gold, A. J., ... & Birgand, F. (2017). High-frequency dissolved organic carbon and nitrate measurements reveal differences in storm hysteresis and loading in relation to land cover and seasonality. *Water Resources Research*, *53*(7), 5345-5363.

Wang, T., Hamann, A., Spittlehouse, D. L., & Murdock, T. Q. (2012). ClimateWNA—high-resolution spatial climate data for western North America. *Journal of Applied Meteorology and Climatology*, *51*(1), 16-29.

Wanninkhof, R. (1992). Relationship between wind speed and gas exchange over the ocean. *Journal of Geophysical Research: Oceans*, *97*(C5), 7373-7382.

Waterloo, M. J., Oliveira, S. M., Drucker, D. P., Nobre, A. D., Cuartas, L. A., Hodnett, M. G., ... & Pimentel, T. P. (2006). Export of organic carbon in run-off from an Amazonian rainforest blackwater catchment. *Hydrological Processes: An International Journal*, *20*(12), 2581-2597.

Watras, C. J., Hanson, P. C., Stacy, T. L., Morrison, K. M., Mather, J., Hu, Y. H., & Milewski, P. (2011). A temperature compensation method for CDOM fluorescence sensors in freshwater. *Limnology and Oceanography: Methods*, *9*(7), 296-301.

Weigand, J., Mitchell, A., & Morgan, D. (1990). Coastal temperate rain forests: definition and global distribution with particular emphasis on North America. *Unpublished report prepared for Ecotrust/Conservation International, Portland, OR*.

Weishaar, J., Aiken, G., Bergamaschi, B., Fram, M., Fujii, R., & Mopper, K. (2003). Evaluation of specific ultra-violet absorbance as an indicator of the chemical content of dissolved organic carbon. *Environmental Science and Technology*, *37*(20), 4702–4708. https://doi.org/10.1021/es030360x

Williams, G. P. (1989). Sediment concentration versus water discharge during single hydrologic events in rivers. *Journal of Hydrology*, *111*(1-4), 89-106.

Wilson, H. F., Saiers, J. E., Raymond, P. A., & Sobczak, W. V. (2013). Hydrologic drivers and seasonality of dissolved organic carbon concentration, nitrogen content, bioavailability, and export in a forested New England stream. *Ecosystems*, *16*(4), 604-616.

Yang, L., Chen, C. A., Lui, H., Zhuang, W., & Wang, B. (2016). Estuarine , Coastal and Shelf Science Effects of microbial transformation on dissolved organic matter in the east Taiwan Strait and implications for carbon and nutrient cycling. *Estuarine, Coastal and Shelf Science*, *180*, 59–68. https://doi.org/10.1016/j.ecss.2016.06.021

Ylöstalo, P., Seppälä, J., Kaitala, S., Maunula, P., & Simis, S. (2016). Loadings of dissolved organic matter and nutrients from the Neva River into the Gulf of Finland – Biogeochemical composition and spatial distribution within the salinity gradient. *Marine Chemistry*, *186*, 58–71. https://doi.org/10.1016/j.marchem.2016.07.004

Ziegler, A. D., Benner, S. G., Kunkel, M. L., Phang, V. X., Lupascu, M., & Tantasirin, C. (2016). Particulate carbon and nitrogen dynamics in a headwater catchment in Northern Thailand: hysteresis, high yields, and hot spots. *Hydrological Processes*, *30*(19), 3339-3360.

Zimmer, M. A., Pellerin, B., Burns, D., & Petrochenkov, G. (2019). Temporal variability in nitrate–discharge relationships in large rivers as revealed by high frequency data. *Water Resources Research*.

Zuecco, G., Penna, D., Borga, M., & van Meerveld, H. J. (2016). A versatile index to characterize hysteresis between hydrological variables at the runoff event timescale. *Hydrological Processes*, *30*(9), 1449-1466.

Zuecco, G., Rinderer, M., Penna, D., Borga, M., & van Meerveld, H. J. (2019). Quantification of subsurface hydrologic connectivity in four headwater catchments using graph theory. *Science of The Total Environment*, *646*, 1265-1280.

Appendix 1

Introduction

In situ fluorescence sensors (Turner Designs Cyclops 7) detect the fluorophoric component of stream DOM (fDOM) through optical measures and are thus sensitive to parameters that affect the measurement of fluoresced light within streamwater. These parameters include temperature, turbidity, and inner filter effects (absorbance). The chromophoric component of stream DOM dampens the fluoresced signal through absorbance in a non-linear relationship, which is termed the “inner filter effect” (Downing et al., 2012). If there are high turbidity levels in the stream, suspended particles scatter the sensor’s emission and dampen the return signal in a linear relationship (Downing et al., 2012). Finally, decreasing temperature dampens DOM fluorescence, and thus the fDOM sensor’s millivolt signal, in a linear process known as thermal quenching by radiationless decay (Watras et al., 2011). As part of the standard operating protocol for *in situ* fDOM sensors, adjustments must be made on the raw data output to correct for the influence of these parameters.

fDOM Sensor Calibrations

fDOM, temperature, and turbidity sensors were deployed in four study watersheds on Calvert and Hecate Islands (WS 703, WS 708, WS 819, and WS 1015). fDOM sensors (Turner Designs Cyclops 7, excitation/emission wavelengths = 370/425nm) were each paired with a turbidity sensor (Cyclops Submersible Sensor) and were installed in proximity to previously installed water temperature sensors (OTT Hydromet Pressure Level Sensor). Each fDOM sensor was equipped with a wiper to prevent biofilm accumulation. fDOM and turbidity sensors were installed in WS 708 in July 2014, and installed in WS 1015, 819, and 703 in July 2015. Measurements for fDOM sensor corrections were undertaken annually in July 2015 and 2016, using stream water from the deployment watersheds. Corrections were based on procedures developed by Watras et al. (2011) and Downing et al. (2012) and were applied in a stepwise fashion. Calibrations were conducted with support from the Hakai Institute and the Hakai Watersheds Research Program on Calvert Island, British Columbia, Canada.

Temperature Correction

De-ionized Milli-Q (DI) water was added to stream water from each study watershed (WS 703, 708, 819, 1015) to create a series of 3L dilution standards of 100%, 75%, 25%, and 0% stream water. Stream water samples were additionally processed and measured for DOC concentration and absorbance at 254nm. Dilution standards were chilled to ~4°C in pre-leached, non-reflective, black, high density 4L polyethylene (HDPE) polycarbonate pails and slowly warmed to 25-30°C in the dark while the fDOM sensor recorded measurements every five seconds, producing a 5minute average (mV). An OTT Hydromet Pressure Level Sensor was additionally used to record temperature concurrent with the fDOM measurements. The resulting relationship between temperature and raw fDOM sensor output was used to calculate the temperature coefficient, rho (ρ), for each dilution in the series, as defined in Watras et al. (2011):

$$\rho = m(c)/fDOM_r(c) \qquad \textit{(1)}$$

Where m(c) is the slope, and $fDOM_r(c)$ is the intercept of the linear equation between temperature (x) and raw fDOM sensor output (y). Within each watershed, values of ρ for each streamwater-containing member of the dilution series were averaged to arrive at the final value for ρ. The calculated ρ was then used to correct to a constant temperature of 20°C following Downing et al. (2012):

$$fDOM_{20} = fDOM_{raw} + \rho(T_{meas} - 20) \qquad \textit{(2)}$$

Where $fDOM_{20}$ is the fDOM sensor output corrected for temperature at 20°C, $fDOM_{raw}$ is the uncorrected fDOM sensor output, and T_{meas} is the measured temperature in degrees Celsius. Corrected outputs for 2015 are shown in Figure A1.1. The corrected $fDOM_{20}$ was then input to the turbidity corrections described below.

Turbidity Correction

Standard solutions containing streamwater, a manufactured AMCO Clear 100 NTU turbidity standard (E223-86861), and DI water were created to enable a dilution series that contained a constant (50%) concentration of streamwater, and turbidity concentrations ranging from 0 to 50 NTU. Measurements of fDOM across this turbidity gradient were used to correct for *in situ* turbidity effects following:

$$fDOM_{20tb} = fDOM_{20} * (m(Turb_{recip}) + Int_{recip}) \qquad (3)$$

Where $m(Turb_{recip})$ is the slope of the equation of the reciprocal of the percent loss in raw fDOM sensor output with increasing turbidity, Int_{recip} is the intercept of the same equation, $fDOM_{20}$ is the fDOM sensor output corrected for temperature, and $fDOM_{20tb}$ is the fDOM sensor output corrected for temperature and turbidity (Figure A1.3). The corrected $fDOM_{20tb}$ is the input for the subsequent absorbance correction.

Inner Filter Effects Correction (Absorbance)

To allow for a correction of inner filter effects beyond the concentrations measured at the time of sensor calibration, a standard dissolved organic matter (DOM) series was created to model equivalent DOC concentration. The series was created with DI water and stock Suwanee River DOM from the International Humic Substances Society (IHSS reference aquatic NOM #

2R101N; ihss.humicsubstances.org/) at 4, 10, 20, 30, 40, 50, 60, and 65 mg L^{-1} DOM, which corresponds to an approximate DOC concentration range of 2 – 32.5 mg L^{-1} ("Source Materials for IHSS Samples", n.d., para. 2). Weighed aliquots of Suwannee DOM were combined with DI water in volumetric flasks, and then transferred to 1L HDPE pails to control for further optical influence (Downing et al., 2012). All measurements were conducted in a dark room with solution and ambient temperatures of ~20°C.

Because the relationship between DOC concentration and absorbance varies across study systems, we calculated an equivalent DOC concentration for each of the NOM standards specific to our study streams. Equivalent DOC was calculated for each watershed using the per-watershed relationship between DOC concentration (mg L^{-1}) and absorbance at 254nm (A254) ($R^2 > 0.99$ in all cases) (Figure A1.5):

$$\text{WS 703: } DOC_{lab} = 22.1 * A254 \tag{4}$$

$$\text{WS 708: } DOC_{lab} = 22.6 * A254 \tag{5}$$

$$\text{WS 819: } DOC_{lab} = 21.4 * A254 \tag{6}$$

$$\text{WS 1015: } DOC_{lab} = 21.1 * A254 \tag{7}$$

Where both DOC concentration and A254 are taken from grab samples collected as part of the HWRP's long-term monitoring program 2015-2016, and the intercept is forced through zero (Figure A1.5).

This relationship was then input to the standard calibration rating curve between NOM and lab-measured sensor fDOM, with NOM converted to equivalent DOC based on the A254 NOM sample measurements and the previously established relationship between lab A254 and lab DOC, where:

$$fDOM_{sensor.l} = a^* DOC_{eq}{}^2 + b^* DOC_{eq} + c \tag{8}$$

Where a is the first coefficient of the negative quadratic model, b is the second, c is the third, and d is the intercept. DOC_{eq} is the equivalent concentration of the Suwannee reference NOM standard based on the relationship between grab sample A254 and grab sample DOC, and $fDOM_{sensor.l}$ is the lab-measured sensor output from the Suwannee standard series. The inverse of this relationship was modeled to a polynomial order 3 relationship rather than a quadratic, as the R2 was higher (R2 = 0.99) (Figure A1.6). The regression model was applied to $fDOM_{20tb}$ to apply an inner filter effect correction to each watershed:

$$fDOM_{20tbIFE} = a*fDOM_{20tb}{}^{3} + b*fDOM_{20tb}{}^{2} + c* fDOM_{20tb} + d \qquad (9)$$

Where $fDOM_{20tbIFE}$ is the sensor output corrected for temperature, turbidity, and inner filter effects (Figure A1.7). We then plotted the paired available *in situ* measurements of $fDOM_{20tbIFE}$ and grab sample DOC concentrations to result in a final linear regression model between fDOM sensor output and stream DOC, where each relationship was modeled as a 1:1 ratio (Figure A1.7):

$$DOC_{sensor} = (fDOM_{20tbIFE} - Int_{grb}) / m_{grb} \qquad (10)$$

Where m_{grb} is the slope of the regression between $fDOM_{20tbIFE}$ and grab sample DOC concentration, Int_{grb} is the intercept, and DOC_{sensor} is the fDOM sensor output fully corrected for temperature, turbidity, and inner filter effects at a 1:1 ratio (Figure A1.8). Sensor DOC was visually quality-controlled for technical errors.

Turbidity Sensor Calibrations

Manufactured AMCO Clear turbidity standards at 100 NTU (E223-86861) and 20 NTU (E223-86924) were used to calibrate turbidity sensors in each study watershed. Turbidity sensors were placed in 1L black HDPE buckets containing DI water (0 NTU), 20 NTU standard, and 100

NTU standard in a darkened room. Turbidity was recorded at 5 second intervals for 5 minutes, and a standard curve was generated to relate sensor mV output to turbidity. This process was conducted in 2015 and 2016 (Figure A1.2).

Hysteresis Analysis

Hysteresis Index (HI)

Calculating HI is a multi-step process that begins with determining the normalized discharge value (Q_i) at every 5% (0.05) interval (Lloyd et al. 2016b) on the rising and falling discharge limb of the hysteresis loop for each event. Q_i was calculated using the formula developed by Lawler et al. (2006):

$$Q_i = k(Q_{max} - Q_{min}) + Q_{min} \tag{11}$$

Where k is the interval length, Q_{max} is the normalized maximum discharge, and Q_{min} is the normalized minimum discharge. Q_i was calculated for each interval k on the rising and falling limb (before and after Q_{max}) of the hysteresis loop at 0.05, 0.1, 0.15, 0.2, 0.25 … up to 1. The corresponding normalized sensor DOC value (DOC_i) was calculated for every Q_i at each k interval level using the formula for linear interpolation (Lawler et al., 2006).

The calculation of HI is the difference between DOC_i on the rising limb of the loop (DOC_{i_RL}) and DOC_i on the falling limb (DOC_{i_FL}), which has been argued more accurately represents change in hysteresis amplitude over the HI ratio method introduced in Lawler et al. (2006), especially for complex loops (Lloyd et al. 2016b):

$$HI = DOC_{i\_RL} - DOC_{i\_FL} \tag{12}$$

The final HI for the entire hysteresis loop is the mean of each individual HI at each 5% interval. The resulting HI produces a value between -1 and 1, where the magnitude indicates the size of the loop, and the sign of the value indicates the type of hysteresis: clockwise (>0), anticlockwise (<0), or no hysteresis (0) (Lloyd et al. 2016b).

Flushing Index (FI)

The second quantitative index calculated for each storm event was the flushing index FI, weighted by maximum DOC concentration (from Butturini et al. 2008; similar to Vaughan et al. 2017). FI classifies intra-event DOC concentration dynamics and assesses their trends over the study period.

$$\mathrm{FI} = (C_{peak} - C_i) / C_{max} \tag{13}$$

Where C_{peak} is DOC concentration at peak discharge, C_i is the initial DOC concentration at the event start, and C_{max} is the maximum DOC concentration exhibited during the storm event. We have used the term C_i instead of C_b, which refers to solute concentration at baseflow prior to or just at the beginning of event start (Butturini et al. 2008; Vaughan et al. 2017). Inherent in the use of C_b is the assumption that discharge will always return to baseflow levels between storm events, which is an inaccurate assumption in this high-precipitation region with “flashy” watershed response patterns. Most storm events are composed of multiple consecutive hydrograph peaks and discharge does not immediately return to baseflow levels before the hydrograph begins to rise again. We have used C_i instead of C_b due to the predominance of multi-peak event series. If an event is composed of a series of consecutive peaks the C_i will be above the DOC concentration at baseflow, yet if an event is isolated, there is a higher probability that the initial DOC concentration is at baseflow level.

Figures

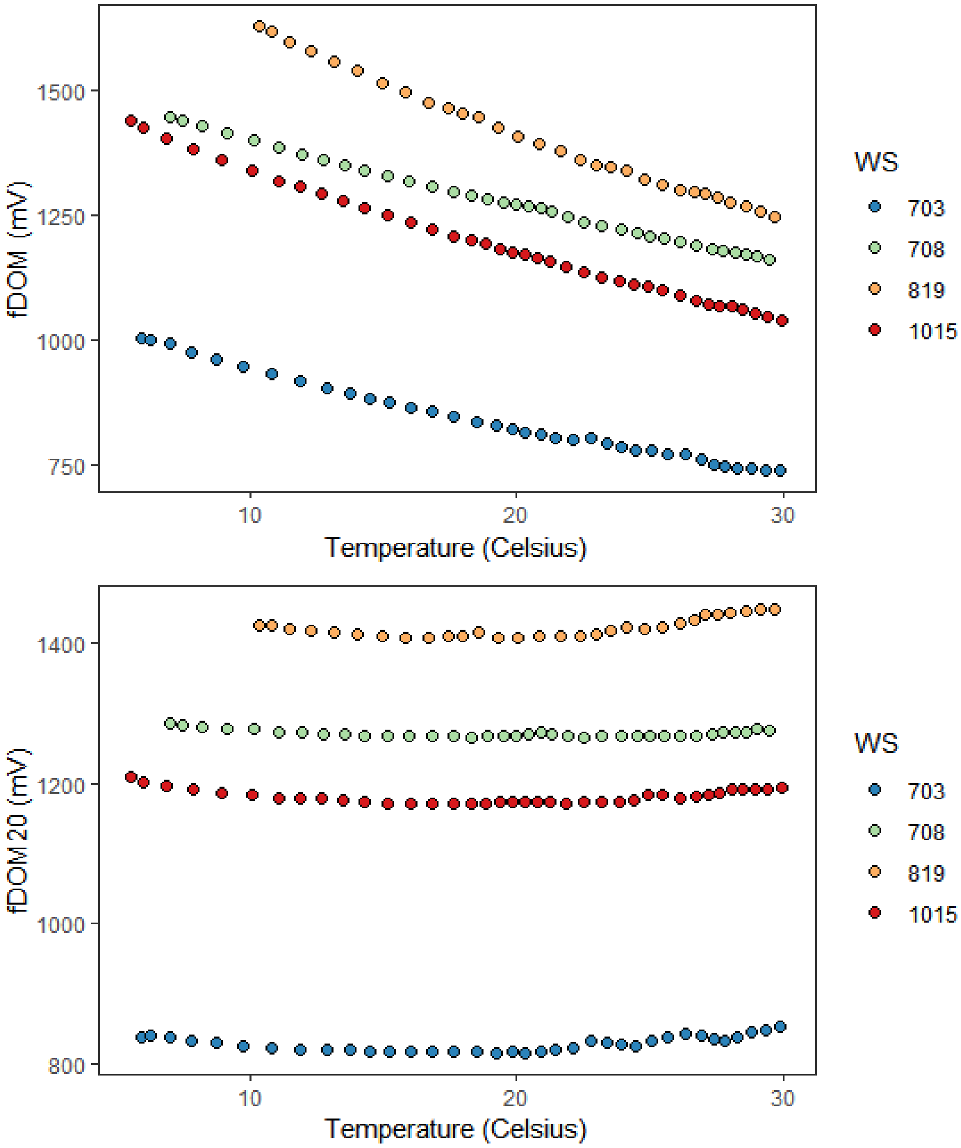

Figure A1.1: From the 2015 temperature calibration process for each study watershed, the relationship between temperature and raw fDOM sensor output (fDOM raw) and fDOM corrected for the influence of temperature set at a control of 20°C (fDOM20), using $\rho = m(c)/fDOM_r(c)$ (Watras et al. 2011) and $fDOM_{corrT} = fDOM_{raw} + \rho(T_{meas} - 20)$ (Downing et al. 2012).

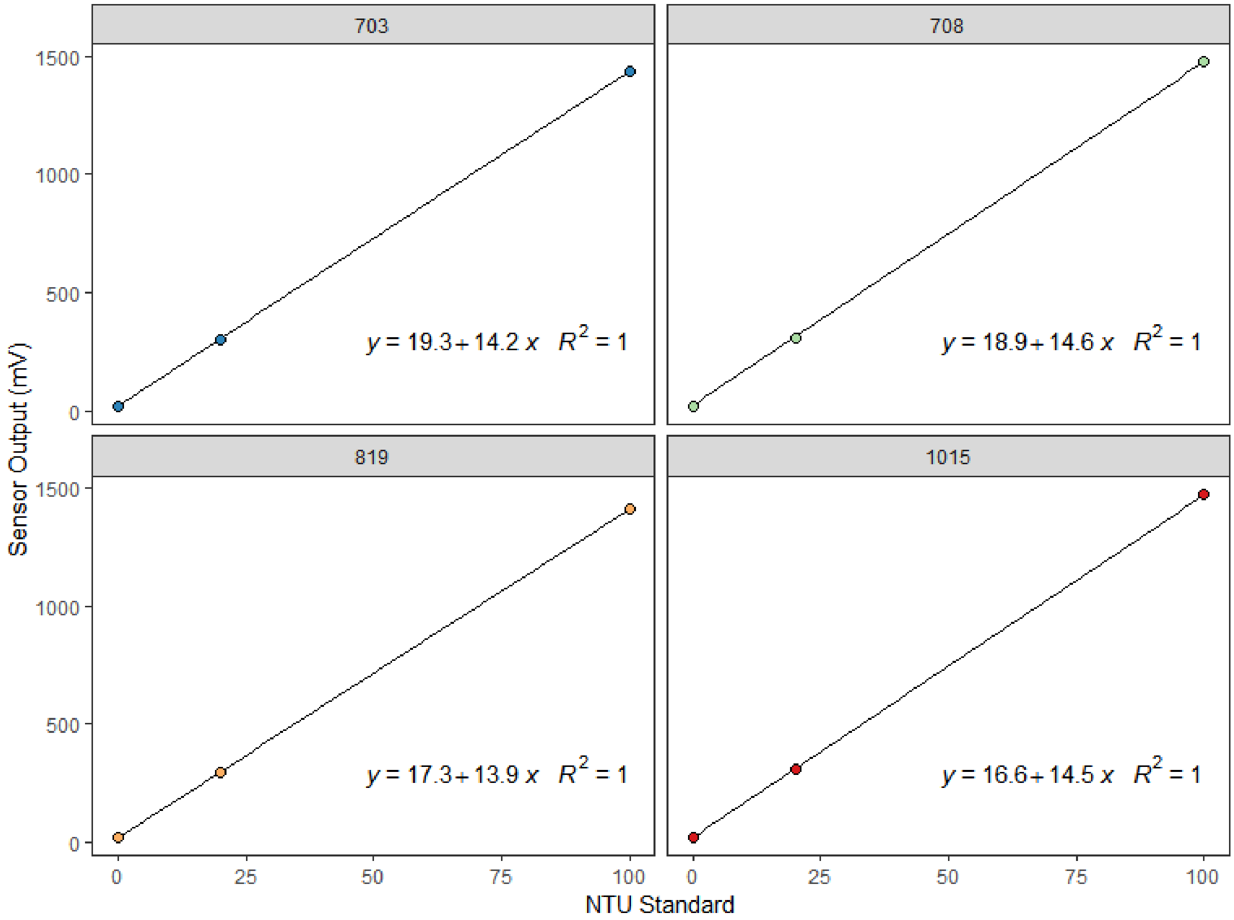

Figure A1.2: Turbidity sensor calibration process from 2015: linear regression between raw turbidity sensor output (mV) and standard turbidity series (NTU).

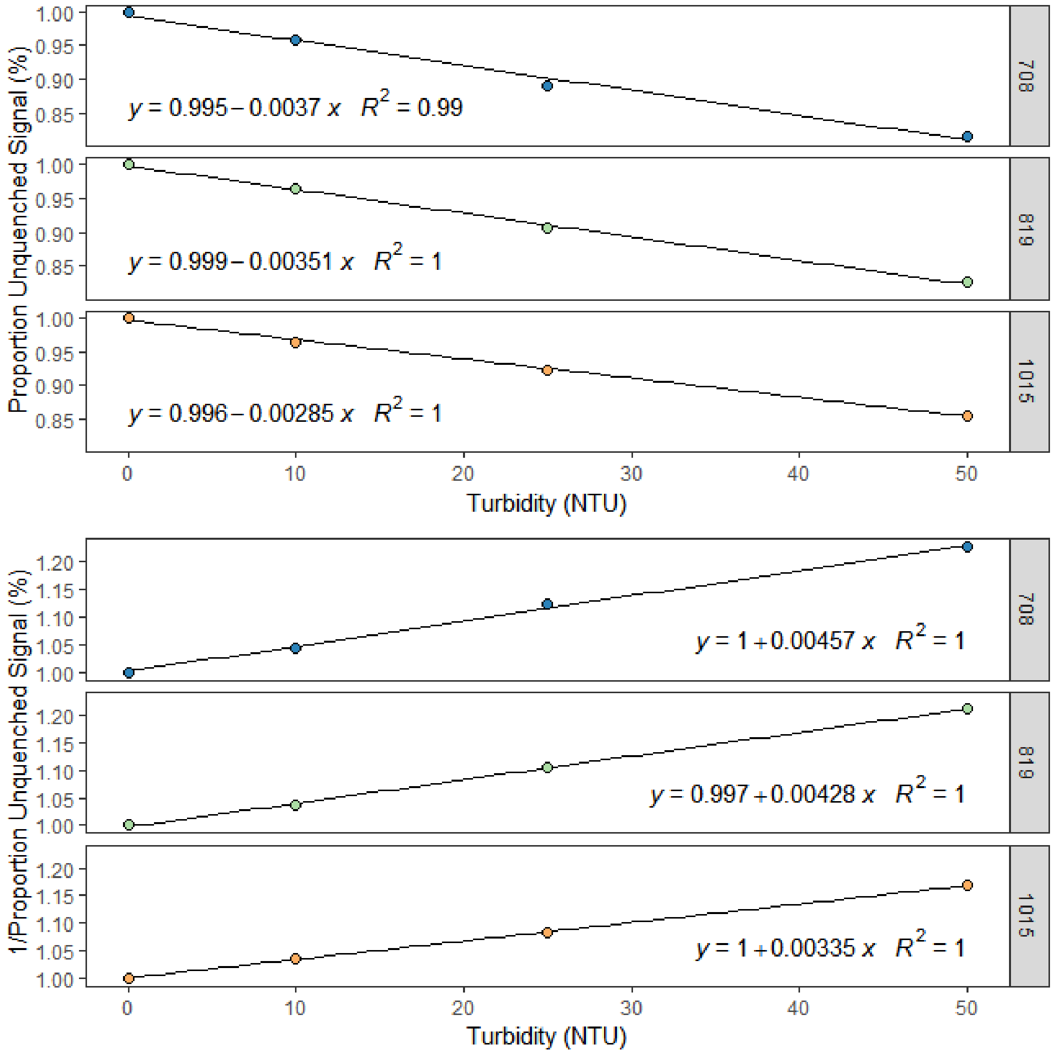

Figure A1.3: From the 2015 turbidity calibration process, the percent loss in fDOM sensor output with increasing turbidity and the reciprocal of the percent loss in fDOM sensor output with increasing turbidity (correction offset). The turbidity correction offset was calculated with fDOMcorrTtb = fDOMcorrT * (m(Turbrecip) + Intrecip), and the turbidity correction offset was calculated with fDOMcorrTtb = fDOMcorrT * (m(Turbrecip) + Intrecip).

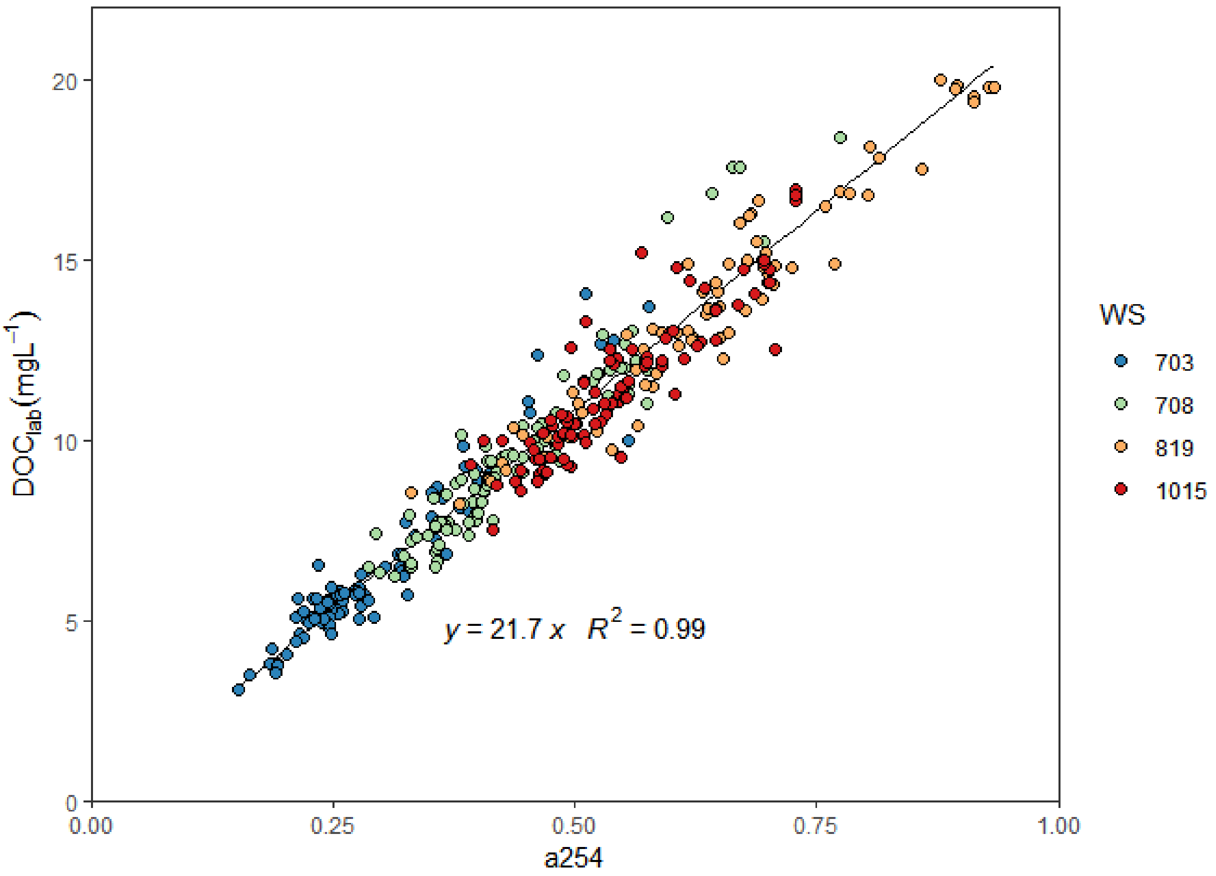

Figure A1.4: The relationship between absorbance at 254nm and DOC concentration from the Freshwater Grab Sampling program (FGS) taken at each study watershed outlet during 2015-2016 by Hakai Watersheds Program Staff.

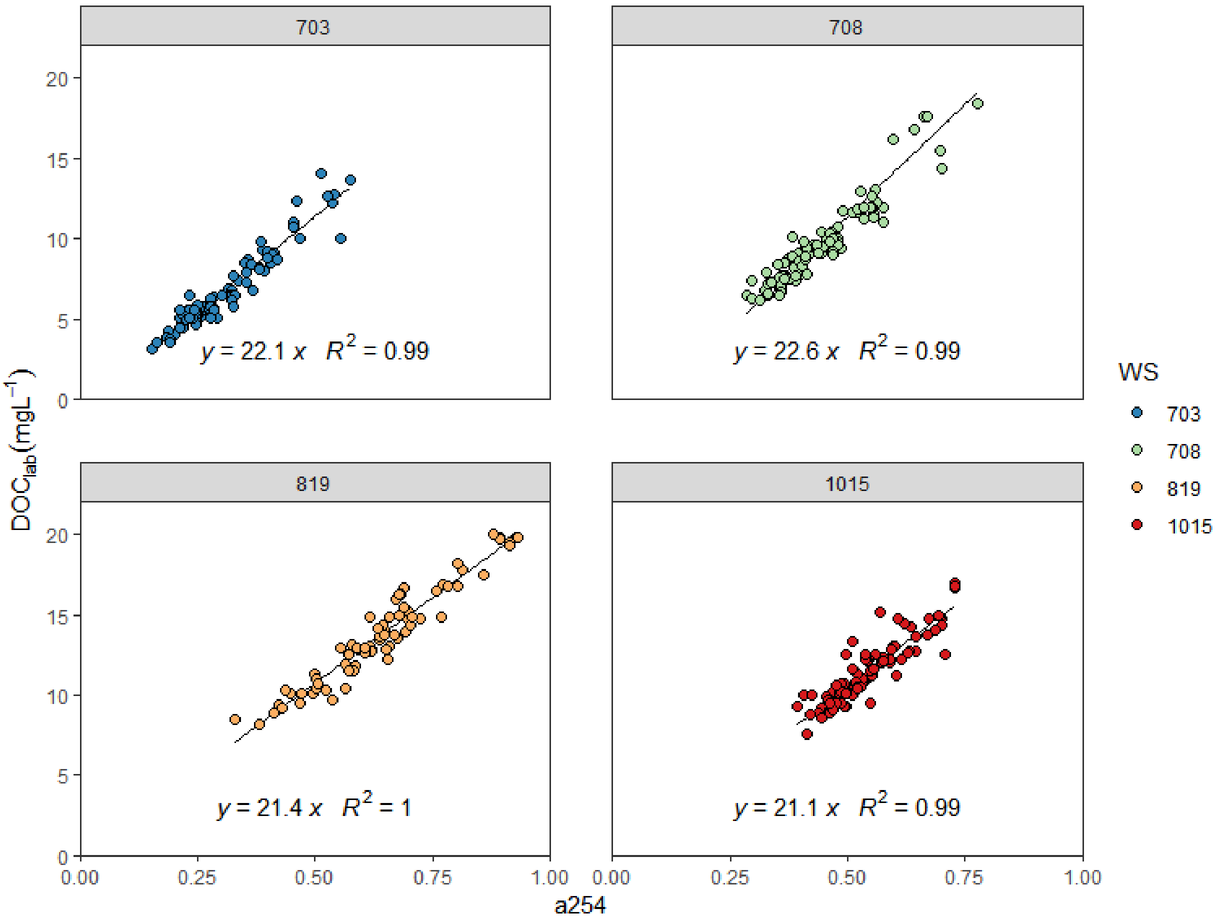

Figure A1.5: The relationship between absorbance at 254nm and DOC concentration per watershed from the Freshwater Grab Sampling program (FGS) taken at each study watershed outlet during 2015-2016 by Hakai Watersheds Program Staff.

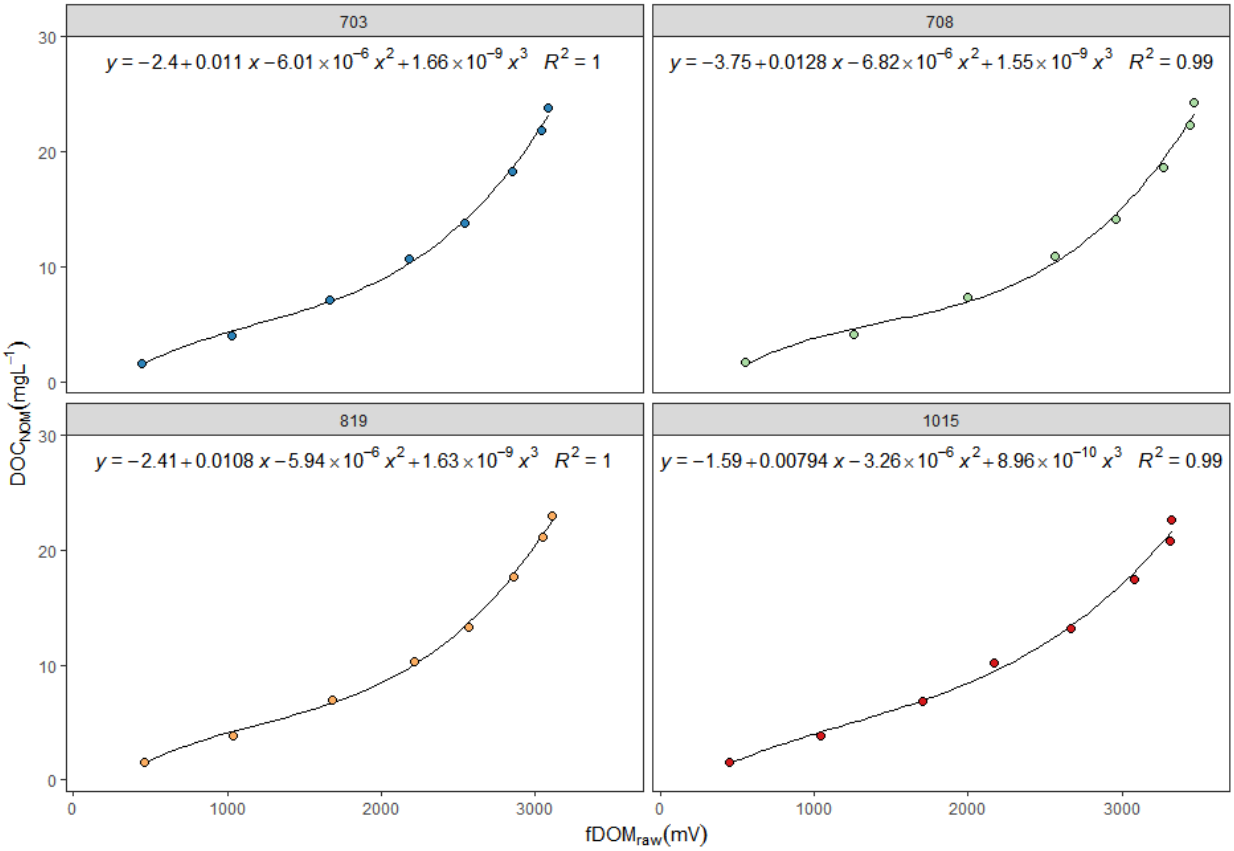

Figure A1.6: Non-linear, polynomial (order 3) regression between sensor fDOM corrected for temperature and turbidity, and the standard DOM series converted to DOC concentration through a linear regression with A254. Sensor fDOM was corrected for absorbance with the equation: $\mathrm{fDOM_{corrTtbIFE}} = (\mathrm{a_{abs}}*(\mathrm{fDOM_{corrTtb}})^2) + (\mathrm{b_{abs}}*\mathrm{fDOM_{corrTtb}}) + \mathrm{c_{abs}}$.

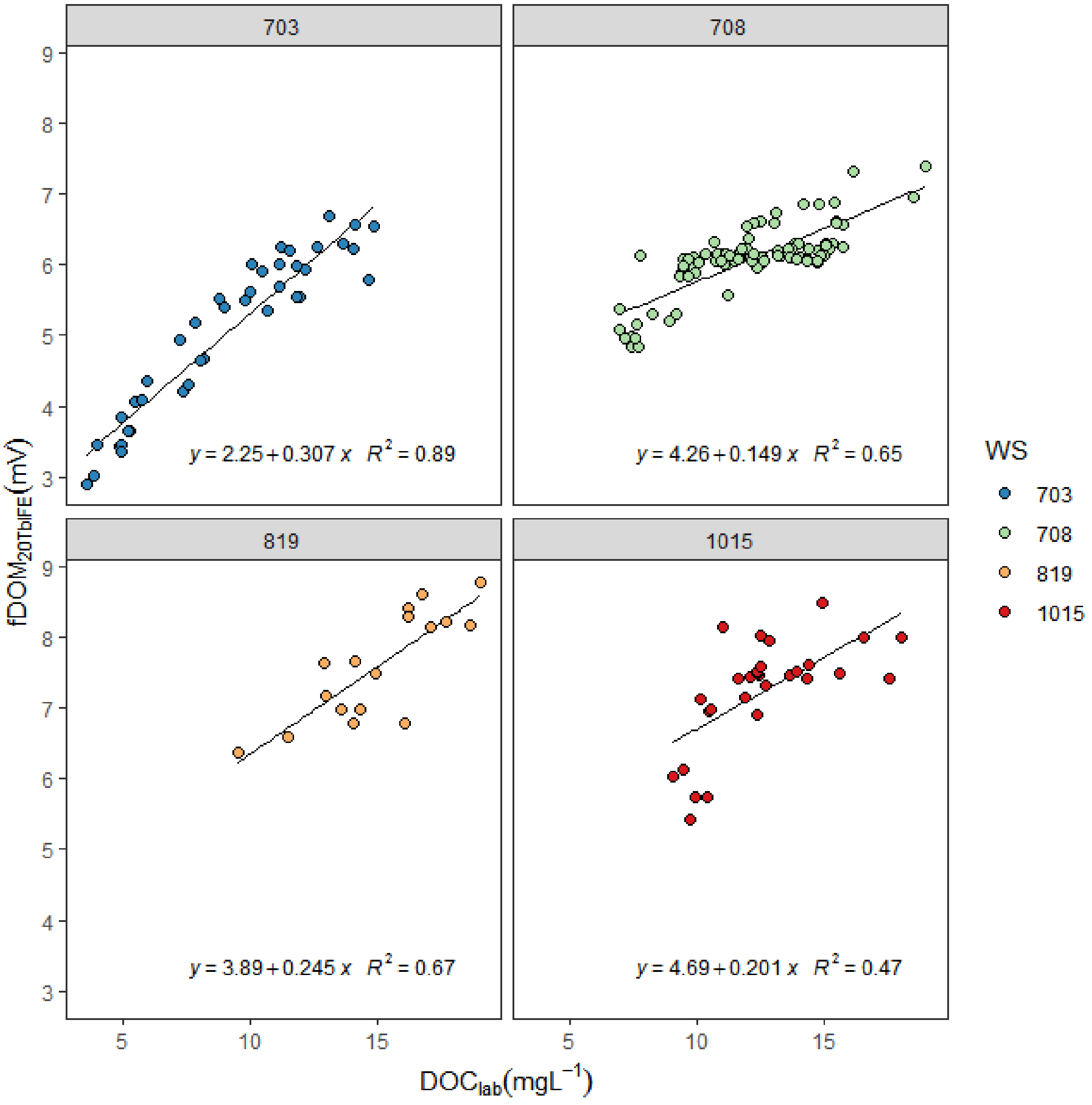

Figure A1.7: Linear regression between fDOM sensor output corrected for temperature, turbidity, and absorbance, and grab sample lab-processed DOC collected by Hakai Watersheds Program Staff. Sensor DOC was visually quality-controlled.

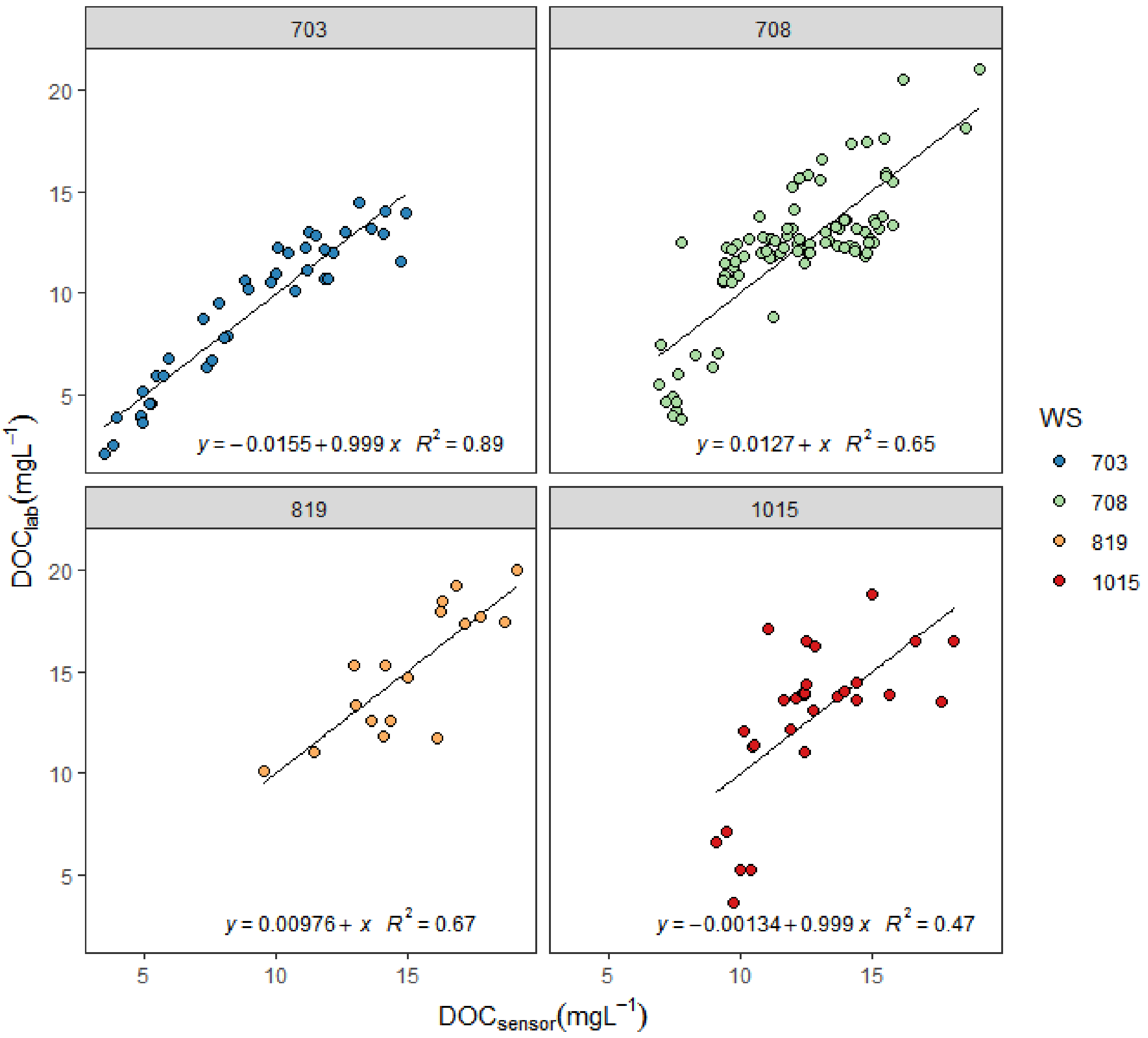

Figure A1.8: Final corrected sensor DOC fit to watershed-specific stream DOC from lab-processed grab samples, collected by Hakai Watersheds Program Staff. Sensor DOC was visually quality-controlled.

Appendix 2

Tables

Table A2.1: Significantly different pairs of response variables (FI & HI Combination, FI, HI) per different categorical groups (seasons, watersheds) assessed using the Kruskal-Wallis test.

Response Variable(s)	Groups with significant differences ($p < 0.05$) (seasons, watersheds)	χ^2	df	p value
FI & HI Combination	Winter, Summer	12.20	3	p=0.006
FI & HI Combination	WS 703, WS 708	13.65	3	p=0.003
FI	Winter, Summer	31.00	3	p<0.001
FI	Fall, Summer	31.00	3	p<0.001
FI	WS 819, WS 1015	11.04	3	p=0.011
HI	WS 703, WS 708	37.53	3	p<0.001
HI	WS 703, WS 819	37.53	3	p<0.001